November 2001 • NREL/SR-520-31290

Subcontractor Report

High-Efficiency Triple-Junction Amorphous Silicon Alloy Photovoltaic Technology

Final Technical Report
6 March 1998 – 15 October 2001

S. Guha
United Solar Systems Corp.
Troy, Michigan

National Renewable Energy Laboratory

1617 Cole Boulevard
Golden, Colorado 80401-3393

NREL is a U.S. Department of Energy Laboratory
Operated by Midwest Research Institute • Battelle • Bechtel

Contract No. DE-AC36-99-GO10337

November 2001 • NREL/SR-520-31290

High-Efficiency Triple-Junction Amorphous Silicon Alloy Photovoltaic Technology

Final Technical Report
6 March 1998 – 15 October 2001

S. Guha
United Solar Systems Corp.
Troy, Michigan

NREL Technical Monitor: K. Zweibel

Prepared under Subcontract No. ZAK-8-17619-09

National Renewable Energy Laboratory

1617 Cole Boulevard
Golden, Colorado 80401-3393

NREL is a U.S. Department of Energy Laboratory
Operated by Midwest Research Institute • Battelle • Bechtel

Contract No. DE-AC36-99-GO10337

NOTICE

Available electronically at http://www.doe.gov/bridge

Available for a processing fee to U.S. Department of Energy
and its contractors, in paper, from:

U.S. Department of Energy
Office of Scientific and Technical Information
P.O. Box 62
Oak Ridge, TN 37831-0062
phone: 865.576.8401
fax: 865.576.5728
email: reports@adonis.osti.gov

Available for sale to the public, in paper, from:

U.S. Department of Commerce
National Technical Information Service
5285 Port Royal Road
Springfield, VA 22161
phone: 800.553.6847
fax: 703.605.6900
email: orders@ntis.fedworld.gov
online ordering: http://www.ntis.gov/ordering.htm

Printed on paper containing at least 50% wastepaper, including 20% postconsumer waste

Preface

This Final Technical Report covers the work performed by United Solar Systems Corp. for the period March 6, 1998 to October 15, 2001 under DOE/NREL Subcontract No. ZAK-8-17619-09. The following personnel participated in the research program.

> A. Banerjee, E. Chen, G. Fischer, S. Guha (Principal Investigator), G. Pietka, M. Hopson, N. Jackett, K. Lord, A. Mohsin, J. Noch, T. Palmer, D. Wolf, B. Yan, J. Yang, and K. Younan.

Collaboration with members of the Thin-Film Partnership program is acknowledged.

Table of Contents

Section			Page
List of Figures			**4**
List of Tables			**6**
Summary			**8**
Section 1	**Introduction**		**14**
Section 2	**a-Si Alloy and a-SiGe Alloy Materials and Solar Cells Near the Threshold of Amorphous-to-Microcrystalline Transition**		**15**
	2.1.	Introduction	**15**
	2.2.	a-Si and a-SiGe Alloys Deposited on the Transition Edge using Hydrogen Dilution Profiling	**15**
	2.3.	Increase in V_{oc} with Light Soaking of Mixed Phase Solar Cells	**19**
	2.4.	Microdoping	**24**
	2.5.	Summary	**25**
Section 3	**Status of a-Si Alloy Solar Cells Deposited with RF at 3Å/s**		**27**
	3.1.	Introduction	**27**
	3.2.	Component Cells	**27**
	3.3.	Triple-Junction Cells	**28**
Section 4	**Modified Very-High-Frequency (MVHF) Plasma Enhanced Chemical Vapor Deposition of a-Si and a-SiGe Alloy Solar Cells at High Deposition Rates**		**31**
	4.1.	Introduction	**31**
	4.2.	Correlation of Process Parameters of MVHF Plasma and Device Performance of a-Si and a-SiGe Alloy Solar Cells	**32**
	4.2.1.	Ion Energy Distribution of RF and MVHF Plasma and the Effect of Ion Bombardment on a-Si and a-SiGe Alloy Solar Cells	**32**
	4.2.2.	Effect of Hydrogen Dilution on a-Si and a-SiGe Alloy Solar Cells made Near the Formation of Microcrystalline Silicon	**39**
	4.2.3.	Study of Amorphous Silicon Alloy Solar Cells Deposited using Fluorine Containing Gases	**41**
	4.2.4.	a-Si and a-SiGe Alloy Solar Cells made with Amplitude-Modulated MVHF Glow Discharge	**48**
	4.3.	Bandgap Engineering of a-Si and a-SiGe Alloy Solar Cells	**50**
	4.3.1.	n/i and i/p Interfaces in a-Si Alloy Solar Cells	**50**
	4.3.2.	n/i and i/p Interfaces in a-SiGe Alloy Middle Cells	**51**
	4.3.3.	Bandgap Profiling of a-SiGe Alloy Solar Cells	**53**
	4.4.	Optimized MVHF a-Si and a-SiGe Alloy Multijunction Cells	**54**

Section 5 Stability of a-Si and a-SiGe Alloy Solar Cells made at Various Deposition Rates 61

5.1. Introduction **61**
5.2. Initial Annealing of a-Si and a-SiGe Alloy Solar Cells **61**
5.2.1. a-Si Alloy Solar Cells **61**
5.2.2. a-SiGe Alloy Solar Cells **62**
5.2.3. Double-Junction a-Si/a-SiGe Alloy Solar Cells **62**
5.3. Comparison of the Stability of RF and MVHF a-Si Alloy Solar Cells **64**
5.4. Annealing Kinetics of a-Si Alloy Solar Cells made at Various Deposition Rates **65**
5.5. Stability Study **69**

Section 6 Status of Amorphous Silicon Alloy Component and Multijunction Cells and Modules Deposited in a Large-Area Reactor 70

6.1. Introduction **70**
6.2. Device Fabrication and Measurement **70**
6.2.1. Small-Area (0.268cm^2) Devices **70**
6.2.2. Module Fabrication **70**
6.3. Stability Studies **70**
6.4. Results of Component Cells **71**
6.4.1. Top Cell on Stainless Steel Substrate **71**
6.4.2. Middle Cell on Stainless Steel Substrate **71**
6.4.3. Bottom Cell on Ag/ZnO Back Reflector **71**
6.5. Results of Triple-Junction Cells **73**
6.6. Module Results **73**
6.6.1. Modules of Aperture Area ~460cm^2 **73**
6.6.2. Modules of Aperture Area ~920cm^2 **73**
6.7. NREL Measurement of Modules **76**
6.8. Stable Results **76**
6.9. Summary of Large Area Results **79**
6.10. Large-Area Prototype Modules **79**
6.11. IEEE Std 1262-1995 Qualification of Modules **80**

Section 7 Cells and Modules made Using Production Parameters in a Large-Area Reactor 81

7.1. Introduction **81**
7.2. Component Cells **81**
7.3. Triple-Junction Cells **82**
7.4. Stability Studies **82**
7.4.1. Top Cell on Stainless Steel Substrate **82**
7.4.2. Middle Cell on Stainless Steel Substrate **82**
7.4.3. Bottom Cell on Al/ZnO Back Reflector **83**
7.4.4. Triple-Junction Cell on Al/ZnO Back Reflector **84**
7.5. Module Results **84**
7.6. Summary **85**

Section 8 References 88

List of Figures

Figure # **Caption**

1. Thickness dependence of V_{oc} of a-Si alloy cells deposited with different hydrogen dilution.
2. Thickness dependence of V_{oc} of a-SiGe alloy cells deposited with different hydrogen dilution.
3. Dependence of initial V_{oc} on hydrogen dilution ratio.
4. One-sun light-induced changes in V_{oc} versus initial V_{oc} for cells with an *i* layer thickness of 2500Å (x), 5000Å (o), and 1μm (□). ◆ denotes changes produced by 30-sun light soaking on a 5000Å cell. The solid lines are polynomial fits to the data and serve as a guide to the eye.
5. Dark J-V characteristics of solar cells in the (a) annealed (□) and light-soaked (■) states in the amorphous phase, and (b) annealed (❍) and light-soaked (●) states in the mixed phase.
6. Initial and stabilized J-V characteristics of a triple-junction cell deposited at 3Å/s on an Ag/ZnO back reflector.
7. Stabilized quantum efficiency of a triple-junction cell deposited at 3Å/s.
8. The energy distribution of positive ions reached to the substrate in a H_2 plasma excited by 75 MHz VHF. The pressures were 0.1 and 1.0 Torr and VHF power was 10 W.
9. The positive ion energy distribution of a H_2 plasma excited by 13.56 MHz RF. Other conditions are the same as in Fig. 8.
10. Comparison of the positive ion energy distribution of pure H_2 plasma and plasma with H_2 and SiH_4 mixture. The measurements were made at 0.1Torr with 11W VHF power.
11. Ion energy distribution with two VHF powers for H_2 plasma at 0.1Torr.
12. Ion energy distribution with two RF powers for H_2 plasma at 0.1Torr.
13. Characteristic parameters for 2100Å thick a-Si alloy solar cells made at different SiH_4 flow rates on ss substrate.
14. V_{oc} as a function of thickness of intrinsic layer for a-Si alloy solar cells made using MVHF at deposition rate ~8-9Å/s. The four gas flow rates refer to SiH_4 gas.
15. Fill factor of a-SiGe alloy solar cells on ss as a function of H_2 flow rate. The cells were made at ~6Å/s.
16. Fill factors of a-SiGe alloy solar cells on BR as a function of H_2 flow rate. The deposition conditions were the same as in Fig. 15.
17. Characteristics of a-Si:F:H solar cells as a function of gas flow ratio $HF/(Si_2H_6+HF)$ or $SiF_4/(Si_2H_4+SiF_4)$. The cells were made with RF at low deposition rates.
18. Characteristics of a-Si:F:H solar cells as a function of gas flow ratio $HF/(SiH_4+HF)$ or $SiF_4/(SiH_4+SiF_4)$. The cells were made with MVHF at deposition rate ~8-9 Å/s. The cell thickness is ~2200Å.
19. Deposition rate vs. modulation frequency for a-Si alloy materials.
20. Self-bias vs. modulation frequency for a-Si alloy deposition.
21. Initial active-area J-V characteristics of the best a-Si alloy top cell made with MVHF at ~6Å/s.
22. Initial active-area quantum efficiency of the best a-Si alloy top cell made with MVHF at 6Å/s.
23. Initial active-area J-V characteristics of a-SiGe alloy middle cell made with MVHF at 6Å/s with an optimized bandgap profile.
24. Initial active-area quantum efficiency of MVHF a-SiGe alloy middle cell shown in Fig. 23.
25. Initial active-area J-V characteristics of the best a-Si/a-Si alloy same bandgap double-junction cell made with MVHF at high rate.
26. Initial active-area quantum efficiency of a-Si/a-Si alloy double-junction cell shown in Fig. 25.
27. Initial active-area J-V characteristics of the best MVHF a-Si/a-SiGe alloy double-junction solar cell.
28. Initial active-area quantum efficiency of the MVHF a-Si/a-SiGe alloy double-junction cell shown in Fig. 27.
29. Initial active-area J-V characteristics of the best triple-junction cell made with MVHF at high rate.

30. Initial active-area quantum efficiency of the best triple cell made with MVHF at high deposition rate shown in Fig. 29.
31. FF versus light soak time for the rf a-Si alloy solar cell made with high H_2 dilution. The diamond represents the cell with initial annealing, and the square represents the reference sample.
32. FF versus light soak time for the rf a-Si alloy solar cell made with no H_2 dilution. The diamond represents the cell with initial annealing, and the square represents the reference sample.
33. J-V characteristics and quantum efficiency of the best top cell made with MVHF at 8Å/sec. The solid and dashed curves indicate the initial and stabilized states, respectively.
34. Annealing kinetics at 100°C of normalized light-induced defect density.
35. The annealing activation energy distribution of a-Si alloy solar cells deposited at different deposition rates.
36. Initial I-V characteristics of module 6915 of area 463cm^2 and efficiency 12.7%.
37. Initial I-V characteristics of encapsulated module 691548L of area 922cm^2.
38. Initial I-V characteristics of unencapsulated module 2B8493 on Al/ZnO back reflector.
39. Initial I-V characteristics of encapsulated module 2B8493L on Al/ZnO back reflector.

List of Tables

Table # **Caption**

1. Current-Voltage Characteristics of Graded Bandgap a-SiGe Alloy Solar Cells With and Without Hydrogen Profiling.
2. Total-Area J-V Characteristics of Component Cells Deposited with Optimized Hydrogen Dilution.
3. Initial and Light Soaked J-V Characteristics of a-Si Alloy Cells Deposited with Various BF_3/Si_2H_6 Ratios.
4. Initial and Stable J-V Characteristics of an a-Si Alloy Top Cell Deposited at 3Å/s on Stainless Steel Substrate.
5. Initial and Stable J-V Characteristics of an a-SiGe Alloy Middle Cell Deposited at 3Å/s on Stainless Steel Substrate (λ>530nm).
6. Initial and Stable J-V Characteristics of an a-SiGe Alloy Bottom Cell Deposited at 3Å/s on Ag/ZnO Back Reflector (λ>630 nm).
7. Initial and Stable J-V Characteristics of a Triple-junction Cell Deposited at 3Å/s Measured at United Solar and NREL.
8. Characteristics of a-Si Alloy Solar Cells Made at Different Pressures.
9. Characteristics of a-Si Alloy Solar Cells Made at 0.1Torr with Different Biases.
10. Characteristics of a-SiGe Alloy Middle Cells Made at Low Pressure with External Bias.
11. Characteristics of a-SiGe Alloy Middle Cells Made at High Pressure with External Bias.
12. J-V Characteristics of a-Si Alloy Solar Cells made with Different SiF_4 Gas Flow Rates. The H_2 Flow Rate was Reduced by a Factor of Two from the Baseline. The Deposition Rate is ~8-9Å/s.
13. J-V Characteristics of a-Si Alloy Solar Cells made with Different SiF_4 Gas Flow Rates. The H_2 Flow Rate was Reduced by a Factor of Four from the Baseline. The Deposition Rate is ~8-9Å/s.
14. Comparison of Stability of a-Si Alloy Solar Cells made with 20% of SiF_4 and without SiF_4 in the Gas Phase. The Cells were made using MVHF at ~8-9Å/s.
15. Initial Active-Area J-V Characteristics of a-Si Alloy Top Cells made with Various Modulation Frequencies (f). Other Deposition Parameters are the same except Deposition Time that was Adjusted to get a Similar Intrinsic Layer Thickness.
16. Initial Active-Area J-V Characteristics of a-SiGe Alloy Middle Cells made with Various Modulation Frequencies (f). The Measurements were taken under AM1.5 Solar Simulator with a 530nm Cut-On Filter.
17. Initial Active-Area J-V Characteristics of a-Si Alloy Top Cells made at 8-9 Å/s Using MVHF with and without Buffer Layers.
18. New and Old Best Initial Active-Area Results of MVHF Top Cell made on Stainless Steel Substrate at ~6Å/s. The Results of the Best RF Low-Rate (~1Å/s) Top Cell is also shown.
19. J-V Characteristics of a-SiGe Alloy Middle Cells made using MVHF at 4-6Å/s with and without Buffer Layers. #8966 and #8973 have Different Buffer Layers.
20. Initial J-V characteristics of a-SiGe Alloy Middle Cells made with MVHF at 6Å/s with Standard and Profiled Buffer Layers.
21. Comparison of Profiled and Flat Bandgap a-SiGe Alloy Middle Cells and Bottom Cells made with RF at ~1 Å/s and MVHF at ~4-6 Å/s.
22. Initial Active-Area J-V Characteristics of a-SiGe Alloy Middle Cells made with MVHF at 6Å/s with Different Bandgap Profiling.
23. Initial Active-Area Characteristics of a-Si/a-SiGe Dual-Gap Solar Cells with Different Current Matching. The Top Cells were Made at ~8Å/s and the Bottom Cells at ~6 Å/s.
24. J-V Characteristics of a MVHF a-Si Alloy Solar Cell at Different states.
25. J-V Characteristics of RF a-Si Alloy Cells L12682 and L12678 made with High H_2 Dilution and No H_2 Dilution, respectively. The Annealed and Reference Values are Designated as “anneal” and “ref.”, respectively.

26. J-V Characteristics of MVHF a-SiGe Alloy Cell made with High H_2 Dilution at ~6Å/s. The Measurements were made under AM1.5 Solar Simulator with a 530nm Cut-on Filter. Annealed and Reference Halves are Designated as "anneal" and "ref.", respectively.
27. Summary of J-V Characteristics of the MVHF a-Si/a-SiGe Alloy Double-Junction Cell made with High H_2 Dilution. The 'with' and 'without' stand for with Initial Annealing and without Initial Annealing.
28. Initial and Stabilized Characteristics of Top Component Cells on Stainless Steel.
29. Stability of a-Si Alloy Top Cells made with MVHF at ~8Å/sec.
30. Initial and Stabilized Characteristics of Middle Component Cells on Stainless Steel.
31. Initial and Stabilized Characteristics of Bottom Component Cells on Back Reflector.
32. Initial and Light-Soaked J-V Characteristics of a-Si Alloy Solar Cells made at Different Rates.
33. Density of Defect States and Annealing Activation Energy Distribution Parameters for a-Si Alloy Solar Cells Deposited at Different Rates.
34. Initial and Stable J-V Characteristics of Component and Multijunction Solar Cells of Various Structures. The Solar Cells were Made with MVHF at High Deposition Rates.
35. Average Results of Small-Area a-Si Alloy Top Cells on 2"x2" Stainless Steel Substrate.
36. Average Results of Small-area a-SiGe Alloy Middle Cells on 2"x2" Stainless Steel Substrate.
37. Average Results of Small-area a-SiGe Alloy Bottom Cells on 2"x2" Ag/ZnO Substrate.
38. Average Results of Small-area Triple-junction Cells on 2"x2" Ag/ZnO Back Reflector.
39. Initial Spire I-V Characteristics of Unencapsulated Modules.
40. Initial Spire I-V Characteristics of Encapsulated Modules.
41. Comparison of NREL and United Solar Initial Measurements of 920cm^2 Area Encapsulated Modules of Aperture Area ~920cm^2.
42. NREL Measurement of Stable Encapsulated Module Performance.
43. Summary of all Stable Results and Corresponding Phase III Milestones.
44. Initial Total-Area Results of Component Cells of Area 0.268cm^2 made at ~3Å/s using Production Parameters.
45. Initial Total-Area Results of Triple-Junction Devices of Area 0.268cm^2 made at ~3Å/s on Al/ZnO Back Reflector.
46. Average Total-Area Results of Small-Area a-Si Alloy Top Cell on 2"x2" Stainless Steel Substrate with no Back Reflector.
47. Average Total-Area Results (λ>530nm) of Small-Area a-SiGe Alloy Middle Cell on a 2"x2" Stainless Steel Substrate with no Back Reflector.
48. Total-Area Results (λ>630nm) of Small-Area Bottom Cell on 2"x2" Al/ZnO Substrate.
49. Total-Area Results of Small-Area Triple-Junction Cell on 2"x2" Al/ZnO Substrate.
50. Initial Results of Unencapsulated Modules on Al/ZnO Back Reflector.
51. Initial Results of Encapsulated Modules on Al/ZnO Back Reflector.
52. Light-Soaked Results of Encapsulated Modules on Al/ZnO Back Reflector.

Summary

Objectives

The principal objective of this R&D program is to expand, enhance and accelerate knowledge and capabilities for the development of high-performance, two-terminal multijunction hydrogenated amorphous silicon alloy cells and modules with low manufacturing cost and high reliability. The program goal is to obtain 12% stable modules that will qualify IEEE-Std 1262-1995 reliability testing.

Approach

In order to improve efficiency, United Solar uses a spectrum-splitting, triple-junction cell structure. In this configuration, the top cell uses an amorphous silicon alloy of ~1.8eV bandgap to absorb the blue photons. The middle cell uses an amorphous silicon germanium alloy (~20% germanium) of ~1.6eV bandgap to capture the green photons. The bottom cell has ~40% germanium to reduce the bandgap to ~1.4eV to capture the red photons. The cells are deposited on stainless steel with a predeposited silver/zinc oxide back reflector to facilitate light trapping. A thin layer of antireflection coating is applied to the top of the cell to reduce reflection loss.

During the course of the program, research activities were carried out in the following five areas:

1. Fundamental studies to improve our understanding of materials and devices.
2. Deposition of small-area cells using a radio-frequency (rf) technique to obtain higher deposition rates.
3. Deposition of small-area cells using a modified very high frequency (MVHF) technique to obtain higher deposition rates.
4. Large-area cell research to obtain the highest module efficiency.
5. Cells and modules made using production parameters in a large-area reactor to advance the state-of-the-art production technology.

Status/Accomplishments

1. Fundamental Studies

We have previously shown that hydrogen dilution plays a very important role in improving material and cell performance. The highest efficiency cells are obtained when the intrinsic material is deposited at a level of hydrogen dilution that is at the threshold between amorphous and microcrystalline transition. A systematic study of a-Si and a-SiGe alloy solar cells near the transition has been undertaken. The cell thickness investigated is between 1000Å and 5000Å. We have achieved better performance in the top and middle component cells. Details are given in Section 2.

2. Cells Deposited at High Rates using RF

Component and triple-junction cells have been deposited at ~3Å/s in a small-area reactor using conventional RF glow discharge. Sections 3 and 5 describe the work. The following has been accomplished:

i. Deposited single-junction top cells (~0.25cm^2) on stainless steel substrates without back reflector using a-Si alloy at 3Å/s and achieved a total-area stabilized cell efficiency of 4.7% measured under global AM1.5 after 1000 hours of one-sun light soaking at 50^{o}C.

ii. Deposited single-junction middle cells (~0.25cm^2) on stainless steel substrates without back reflector using a-SiGe alloy at 3Å/s and achieved a total-area stabilized power output of 2.8mW/cm^2

measured under global AM1.5 with a λ>530nm filter after 1010 hours of one-sun light soaking with an appropriate filter at 50°C.

iii. Deposited single-junction bottom cells (~0.25cm^2) on optimized back reflector using a-SiGe alloy at 3Å/s and achieved a total-area stabilized power output of 3.2mW/cm^2 measured under global AM1.5 with a λ>630nm filter after 1000 hours of one-sun light soaking with an appropriate filter at 50°C.

iv. Deposited triple-junction cells (~0.25cm^2) on optimized back reflector at 3Å/s and achieved a total-area stabilized efficiency of 10.3% measured by NREL after 1010 hours of one-sun light soaking at 50°C.

3. Cells Deposited at High Rates using MVHF

Component and triple-junction cells have been deposited at ~6-8Å/s in a small-area reactor using MVHF excitation. Sections 4 and 5 describe the work. The following has been accomplished:

i. Deposited single-junction top cells (~0.25cm^2) on stainless steel substrates without back reflector using a-Si alloy at 6-8Å/s and achieved a total-area stabilized cell efficiency of 5.4% measured under global AM1.5 after 1000 hours of one-sun light soaking at 50°C.

ii. Deposited single-junction middle cells (~0.25cm^2) on stainless steel substrates without back reflector using a-SiGe alloy at 6-8Å/s and achieved a total-area stabilized power output of 2.9mW/cm^2 measured under global AM1.5 with a λ>530nm filter after 1000 hours of one-sun light soaking with an appropriate filter at 50°C.

iii. Deposited single-junction bottom cells (~0.25cm^2) on optimized back reflector using a-SiGe alloy at 6-8Å/s and achieved a total-area stabilized power output of 2.6mW/cm^2 measured under global AM1.5 with a λ>630nm filter after 1000 hours of one-sun light soaking with an appropriate filter at 50°C.

iv. Deposited double-junction a-Si/a-SiGe alloy solar cells (~0.25cm^2) on optimized back reflector at 6-8Å/s and achieved a total-area initial efficiency of 10.6% measured under global AM1.5 spectrum. The stable total-area efficiency is 8.5%.

4. Large-area Module Research

Uniformity in deposition over a large area is key to the achievement of high module efficiency. We use a large-area reactor where the component cells are deposited over one-square-foot area and the uniformity is investigated by evaluating the performance of small-area cells deposited over the entire area. Using this method, we have made high efficiency component cells and have fabricated large-area, triple-junction modules. The work is described in Section 6. The highlights are given below:

i. Deposited array of single-junction top cells (~0.268cm^2) on stainless steel substrates without back reflector using a-Si alloy over areas greater than 900cm^2 and achieved an average total-area stabilized cell efficiency measured under global AM1.5 of 5.4% after 1031 hours of one-sun light soaking at 50°C.

ii. Deposited array of single-junction middle cells (~0.268cm^2) on stainless steel substrates without back reflector using a-SiGe alloy over areas greater than 900cm^2 and achieved an average total-area stabilized power output measured under global AM1.5 with λ>530nm filter of 3.7mW/cm^2 after 1655 hours of one-sun light soaking with an appropriate filter at 50°C.

iii. Deposited array of single-junction bottom cells (~0.268cm^2) on optimized back reflector substrates using a-SiGe alloy over areas greater than 900cm^2 and achieved an average total-area stabilized power output measured under global AM1.5 with λ>630nm filter of 3.4mW/cm^2 after 1076 hours of one-sun light soaking with an appropriate filter at 50^{o}C.

iv. Deposited array of triple-junction cells (~0.268cm^2) on optimized back reflector substrates using optimized component cells over areas greater than 900cm^2 and achieved an average total-area stabilized efficiency measured under global AM1.5 of 11.6% after 1067 hours of one-sun light soaking at 50^{o}C.

v. Achieved 11.9% initial aperture-area (~920cm^2) efficiency on an encapsulated triple-junction module as measured by NREL. Light soaking at NREL led to a stable aperture-area efficiency of 10.5% as measured by NREL.

5. Cells and Modules made Using Production Parameters in Large-Area Reactor

This work was initiated towards the end of the program. The goal was to explore means of enhancing the efficiency of the commercial product using deposition conditions to be used in the upcoming 25MW/year production machine. A large-area reactor was used and cells and modules were fabricated on Al/ZnO back reflector. The work is described in Section 7. The highlights are as follows:

i. Deposited array of single-junction top cells (~0.268cm^2) on stainless steel substrates without back reflector using a-Si alloy at ~3Å/s over an area 460cm^2 and achieved an average total-area stabilized efficiency measured under global AM1.5 of 5.1mW/cm^2.

ii. Deposited array of single-junction middle cells (~0.268cm^2) on stainless steel substrates without back reflector using a-SiGe alloy at ~3Å/s over an area 460cm^2 and achieved an average total-area stabilized power density measured under global AM1.5 with λ>530nm filter of 2.8mW/cm^2.

iii. Deposited single-junction bottom cells (~0.268cm^2) on Al/ZnO back reflector substrates using a-SiGe alloy at ~3Å/s and achieved a total-area stabilized power density measured under global AM1.5 with λ>630nm filter of 2.6mW/cm^2.

iv. Deposited triple-junction cells (~0.268cm^2) on Al/ZnO back reflector substrates using optimized component cells at ~3Å/s and achieved a total-area stabilized efficiency measured under global AM1.5 of 9.1%.

v. Achieved an initial aperture-area efficiency of 10.6% on an encapsulated triple-junction module of aperture area 458cm^2 measured under global AM1.5. The stable aperture-area efficiency after 520 hours of light soak was ~9.1%.

Major Publications

1. Guha, S.; Yang, J.; Banerjee, A.; Sugiyama, S. (1998). "Material issues in the commercialization of amorphous silicon alloy thin-film photovoltaic technology." *Mater. Res. Soc. Symp. Proc.* **507**, 99.
2. Yang, J.; Sugiyama, S.; Guha, S. (1998). "Effect of excitation frequency on the performance of amorphous silicon alloy solar cells." *Mater. Res. Soc. Symp. Proc.* **507**, 157.
3. Chen, C.C.; Lubianiker, Y.; Cohen, J.D.; Yang, J.; Guha, S.; Wickboldt, P.; Paul, W. (1998). "The electronic structure, metastability and transport properties of optimized amorphous silicon-germanium alloys." *Mater. Res. Soc. Symp. Proc.* **507**, 769.

4. Mahan, A.H.; Reedy, R.C., Jr.; Iwaniczko, E.; Wang, Q.; Nelson, B.P.; Xu, Y.; Gallagher, A.C.; Branz, H.M.; Crandall, R.S.; Yang, J.; Guha, S. (1998). "H out-diffusion and device performance in *n-i-p* solar cells utilizing high temperature hot wire a-Si:H i-layers." *Mater. Res. Soc. Symp. Proc.* **507**, 119.
5. Jiang, L.; Schiff, E.; Wang, Q.; Guha, S.; Yang, J. (1998). "Grazing incidence measurements of polarized electroabsorption and light soaking effect on amorphous silicon based solar cells." *Mater. Res. Soc. Symp. Proc.* **507**, 631.
6. Yang, J.; Banerjee, A.; Lord, K.; Guha, S. (1998). "Correlation of component cells with high efficiency amorphous silicon alloy triple-junction solar cells and modules." *2nd World Conference and Exhibition on Photovoltaic Solar Energy Conversion Proceedings*. Vienna, Austria, 387.
7. Guha, S.; Yang, J.; Banerjee, A.; Hoffman, K.; Call, J. (1998). "Manufacturing issues for large volume production of amorphous silicon alloy photovoltaic modules." *NCPV Photovoltaics Program Review Proc.-1998,* 88.
8. Jiang, L.; Wang, Q.; Schiff, E.; Guha, S.; Yang, J. (1998). "Polarized electroabsorption spectra and light soaking of solar cells based on hydrogenated amorphous silicon." *Appl. Phys. Lett*. **72**, 1060.
9. Chen, C.; Zhong, F.; Cohen, J.D.; Yang, J.; Guha, S. (1998). "Evidence for charged defects in intrinsic glow-discharge hydrogenated amorphous silicon-germanium alloys." *Phys Rev. B* **57** Rapid Communications, 4210.
10. Guha, S.; Yang, J.; Williamson, D.L.; Lubianiker, Y.; Cohen, J.D.; Mahan, A.H. (1999). "Structural, defect, and device behavior of hydrogenated amorphous Si near and above the onset of microcrystallinity." *Appl. Phys. Lett.* **74**, 1860.
11. Yan, B.; Yang, J.; Guha, S.; Gallagher, A. (1999). "Analysis of plasma properties and deposition of amorphous silicon alloy solar cells using very high frequency glow discharge." *Mater. Res. Soc. Symp. Proc.* **557**, 115.
12. Yang, J.; Guha, S. (1999). "Amorphous silicon alloy materials and solar cells near the threshold of microcrystallinity." *Mater. Res. Soc. Symp. Proc.* **557**, 239.
13. Mahan, A.H.; Yang, J.; Guha, S.; Williamson, D.L. (1999). "Structural changes in a-Si:H films deposited on the edge of crystallinity." *Mater. Res. Soc. Symp. Proc.* **557**, 269.
14. Lyou, J.H.; Schiff, E.A.; Hegedus, S.S.; Guha, S.; Yang, J. (1999). "Infrared electroabsorption spectra in amorphous silicon solar cells." *Mater. Res. Soc. Symp. Proc.* **557**, 457.
15. Banerjee, A.; Yang, J.; Guha, S. (1999). "Optimization of high efficiency amorphous silicon alloys based triple-junction modules." *Mater. Res. Soc. Symp. Proc.* **557**, 743.
16. Sopori, B.: Madjdpour, J.; Zhang, Y.: Chen, W.; Guha, S.; Yang, J.; Banerjee, A.; Hegedus, S. (1999). "Optical modeling of a-Si solar cells." *Mater. Res. Soc. Symp. Proc.* **557**, 755.
17. Palinginis, K.C.; Cohen, J.D.; Yang, J.; Guha, S. (1999). "Defect bands in a-Si-Ge:H alloys with low Ge content." *J. Non-Cryst. Solids* **266-269**, p. 665.
18. Guha, S.; Yang, J. (1999). "Science and technology of amorphous silicon alloy photovoltaics." *IEEE Trans. Electron Devices*. **46**, 2080.
19. Guha, S. (1999). "Multijunction solar cells and modules." in *Technology and Applications of Amorphous Silicon*, edited by R.A. Street, Springer.
20. Guha, S.; Yang, J.; Banerjee, A. (2000). "Amorphous silicon alloy photovoltaic research present and future." *Progress Photovolt. Res. Appl.* **8**, 141.
21. Yue, G.; Han D.; Williamson, D.L.; Yang, J.; Lord, K.; Guha, S. (2000). "Electronic states of intrinsic layers in n-i-p solar cells near amorphous to microcrystalline silicon transition studied by photoluminescence spectroscopy." *Appl. Phys. Lett.* **77,** 3185.
22. Lubianiker, Y.; Cohen, J.D.; Lubarsky, G.; Rosenwaks, Y.; Yang, J.; Guha, S. (2000). "Structural and electronic properties of optimized a-Si:H films." *J. Non-Cryst. Solids* **266-269,** 253.
23. Mahan, A.H.; Yang, J.; Guha, S.; Williamson, D.L. (2000). "Structural changes in a-Si:H film crystallinity with high H dilution." *Phys. Rev. B.* **61**, 1677.
24. Guha, S.; Yang, J.; Banerjee, A.; Lord, K.; Yan, B. (2000). "Science and technology of amorphous silicon alloy photovoltaics—accomplishments and challenges." *NCPV Program Review Meeting Proc.-2000*, Denver, CO, 31.

25. Yue, G.; Han, D.; Ganguly, G.; Wang, Q.; Yang, J.; Guha, S. (2000). "Characterization for the onset of crystallization of amorphus to microcrystalline silicon by optical spectroscopies." *NCPV Program Review Meeting Proc.-2000*, Denver, CO, 16-19 April 2000.
26. Yue, G.; Han, D.; Yang, J.; Guha, S. (2000). "Thickness and interface layer effects on the amorphous silicon film property studied by various photoluminescence excitation wave lengths." *Mat. Res. Soc. Symp. Proc.* **609**, A5.9.
27. Palinginis, K.C.; Cohen, J.D.; Yang, J.C.; Guha, S. (2000). "A critical test of defect creation models in hydrogenated amorphous silicon alloys." *Mat. Res. Soc. Symp. Proc.* **609**, A3.3.
28. Williamson, D.L.; Marr, D.W.M.; Nelson, B.P.; Iwaniczko, E.; Yang, J.; Yan, B.; Guha, S. (2000). "Small-angle neutron scattering from device quality a-Si:H and a-Si:D prepared by PECVD and HWCVD." *Mat. Res. Soc. Symp. Proc* **609**, A16.2.
29. Yang, J.; Lord, K.; Guha, S.; Ovshinsky, S.R. (2000). "Amorphous silicon alloy solar cells near the threshold of amorphous to microcrystalline transition." *Mat. Res. Soc. Symp. Proc.* **609**, A15.4.
30. Koval, R.; Jiao, L.; Niu, X.; Lu, Z.; Ganguly, G.; Yang, J.; Guha, S.; Collins, R.W.; Wronski, C.R. (2000). "Kinetics of light induced changes in protocrystalline thin film materials and solar cells." *Mat. Res. Soc. Symp. Proc.* **609**, A15.5.
31. Voyles, P.M.; Treacy, M.M.J.; Jin, H-C.; Abelson, J.R.; Gibson, J.M.; Yang, J.; Guha, S.; Crandall, R.S. (2000). "Comparative fluctuation microscopy study of medium-range order in hydrogenated amorphous silicon deposited by various methods." *Mat. Res. Soc. Symp. Proc.* **609**, A2.4.
32. Yang, J.; Banerjee, A.; Lord, K.; Guha, S. (2000). "Status of amorphous silicon alloy solar cells and modules made near the onset of microcrystallinity." *28th IEEE PV Specialists Conference*, Anchorage, AK, 742.
33. Mahan, A.H.; Beyer, W.; Williamson, D.L.; Yang, J.; Guha, S. (2000). "An explanation for the low temperature H evolution peak in hydrogenated amorphous silicon films deposited 'on the edge of crystallinity'." *Phi. Mag. Lett.* **80**, 647.
34. Yan, B.; Yang, J.; Lord, K.; Guha, S. (2001). "Annealing kinetics of amorphous silicon alloy solar cells made at various deposition rates." *Mat. Res. Soc. Symp. Proc.* **664,** A25.2.
35. Crandall, R.; Yang, J.; Guha, S. (2001). "Defect density profiling in light-soaked and annealed hydrogenated amorphous silicon solar cells." *Mat. Res. Soc. Symp. Proc.* **664,** A19.2.
36. Cohen, D.; Heath, J.T; Palinginis, K.C.; Yang, J.; Guha, S. (2001). "Light-induced annealing of deep defects in low Ge fraction a-Si:H alloys: Further insights into the fundamentals of light-induced degradation." *Mat. Res. Soc. Symp. Proc.* **664,** A12.5.
37. Yang, J.; Yan, B.; Guha, S. (2001). "Amorphous silicon and silicon-germanium alloy solar cells deposited by VHF at high rates." *Mat. Res. Soc. Symp Proc.* **664,** A11.3.
38. Yue, G.; Han, D.; Yang, J.; Lord, K.; Yan, B.; Guha, S. (2001). "Effects of hydrogen dilution on hydrogenated amorphous silicon films and solar cells studied by Raman and photoluminescence spectroscopy." *Mat. Res. Soc. Symp. Proc.* **664,** A9.7.
39. Wang, Q.; Iwaniczko, E.; Yang, J.; Lord, K.; Guha, S. (2001). "High quality amorphous silicon germanium alloy solar cells made by hot wire CVD at 10 Å/s." *Mat. Res. Soc. Symp.* **664,** A7.5.
40. Cohen, J.D.; Heath, J.; Palinginis, K.; Yang, J.; Guha, S. (2001). "Insights into the mechanisms of light-induced degradation from studies of defects in low Ge fraction a-Si,Ge:H alloys." *19th International Conference on Amorphous and Microcrystalline Semiconductors Proc.-2001,* Nice, France (in press).
41. Gunes, M.; Johanson, R.E.; Kasap, S.O.; Yang, J.C.; Guha, S. (2001). "Conductance fluctuations in undoped hydrogenated amorphous silicon-germanium alloy thin films." *19th International Conference on Amorphous and Microcrystalline Semiconductors Proc., 2001,* Nice, France (in press).
42. Spanakis, E.; Stratakis, E.; Tzanetakis, P.; Fritzsche, H.; Guha, S.; and Yang, J. (2001). "Light-induced stress in a-$Si_{1-x}Ge_x$:H alloys and its correlation with the Staebler-Wronski effect." *NICE*.
43. Lyou, J.; Schiff, E.; Guha, S.; Yang, J. (2001). "Electroabsorption measurements and built-in potentials in amorphous silicon-germanium solar cells." *Appl. Phys. Lett.* **78**, 1924.
44. Lord, K.; Yan, B.; Yang, J.; Guha, S. (2001). "Light-induced Increase in the open-circuit voltage of thin-film heterogeneous silicon solar cells." *Appl. Phys. Lett.* (in press).

45. Tsu, D.V.; Chao, B.S.; Ovshinsky, S.R.; Jones, S.J.; Yang, J.; Guha, S.; Tsu, R. (2001). "Heterogeneity in hydrogenated silicon: Evidence for the intermediately ordered chainlike objects." *Phy. Rev. B* **63**, 125338.
46. Guha, S.; Yang, J.; Banerjee, A.; Yan, B.; Lord, K. (2001). "Mass production of amorphous silicon alloy photovoltaic modules." *Technical Digest of the International PVSEC-12* Jeju, Korea. **18-1**, 561.
47. Palinginis, K.C.; Cohen, J.D.; Guha, S.; Yang, J.C. (2001). "Experimental evidence indicating a global mechanism for light-induced degradation in hydrogenated amorphous silicon." *Phy. Rev. B* **63,** 201203(R).

Section 1

Introduction

This report describes the research performed under NREL Subcontract No. ZAK-8-17619-09. The research program is intended to expand, enhance and accelerate knowledge and capabilities for the development of high-performance, two-terminal multijunction amorphous silicon (a-Si) alloy cells and modules with low manufacturing cost and high reliability.

In order to improve efficiency, United Solar uses a spectrum-splitting, triple-junction cell structure. In this configuration, the top cell uses an amorphous silicon alloy of ~1.8eV bandgap to absorb the blue photons. The middle cell uses an amorphous silicon germanium alloy (~20% germanium) of ~1.6eV bandgap to capture the green photons. The bottom cell has ~40% germanium to reduce the bandgap to ~1.4eV to capture the red photons. The cells are deposited on stainless steel substrate with a predeposited silver/zinc oxide back reflector to facilitate light trapping. A thin layer of antireflection coating is applied to the top of the cell to reduce reflection loss.

The major research activities conducted under this program were:

1. Fundamental studies to improve our understanding of materials and devices: the work included development and analysis of a-Si alloy and a-SiGe alloy materials prepared near the threshold of amorphous-to-microcrystalline transition and study of solar cells fabricated using these materials.

2. Deposition of small-area cells using a radio-frequency (rf) technique to obtain higher deposition rates.

3. Deposition of small-area cells using a modified very high frequency (MVHF) technique to obtain higher deposition rates.

4. Large-area cell research to obtain the highest module efficiency.

5. Optimization of solar cells and modules fabricated using production parameters in a large-area reactor.

Results on 1 are described in Section 2. Data on higher deposition rates are given in Sections 3, 4, and 5. Module research activities are detailed in Section 6. Investigation of production-compatible technology for cell and module fabrication is discussed in Section 7.

Section 2

a-Si Alloy and a-SiGe Alloy Materials and Solar Cells Near the Threshold of Amorphous-to-Microcrystalline Transition

2.1. Introduction

Our earlier work has demonstrated the beneficial effect of hydrogen dilution during film growth in obtaining high quality a-Si alloys. Materials grown using high dilution exhibit a more ordered film microstructure and higher initial and stabilized solar cell efficiency. We have reported 13% stable cell efficiency and 10.5% aperture-area module efficiency using a triple-junction triple-bandgap structure. During the course of this contract, we discovered that the best material is obtained at a hydrogen dilution level just below the threshold of amorphous-to-microcrystalline transition. This material is characterized by an improved intermediate range order and may contain a small volume fraction of microcrystallites. This section describes the work on a-Si alloy and a-SiGe alloy materials and solar cells prepared near the threshold of amorphous-to-microcrystalline transition.

2.2. a-Si and a-SiGe Alloys Deposited on the Transition Edge using Hydrogen Dilution Profiling

Hydrogen dilution of the process gases has been used to obtain high quality materials and solar cells. Hydrogen dilution is known to promote growth of microcrystallites. The best quality material is grown at a dilution just below the threshold of amorphous-to-microcrystalline transition (Tsu et al. 1997, Koh et al. 1998, Yang et al. 1997). The onset of microcrystallinity also depends on the thickness of the film. The V_{oc} of solar cells has been found to decrease as the transition takes place. Measurement of V_{oc} can, therefore, be used as a tool to determine at what thickness the material becomes microcrystalline (Guha et al. 1999). We have used this technique to investigate the transition in a-Si and a-SiGe alloys and found that the critical dilution depends on the Ge-content in the alloy. The highest quality a-SiGe alloy cells use a profiling of Ge-content as a function of thickness to obtain a graded bandgap cell so as to aid minority carrier transport (Yang et al. 1997). We have changed the amount of hydrogen dilution as the germanium concentration changes to obtain the optimum material throughout the thickness of the cell. This resulted in higher cell efficiency.

Single-junction *n i p* solar cells were grown on stainless steel substrates in a multichamber system. Small-area ($\leq$0.25 cm^2) cells were obtained by depositing top contacts over the 4cm x 4cm substrate area. Gas mixtures of disilane in hydrogen and disilane and germane in hydrogen, respectively, were used to deposit the intrinsic layers of the a-Si and a-SiGe alloy solar cells. The hydrogen dilution was varied to obtain the threshold for amorphous-to-microcrystalline transition. The range of cell thickness investigated was between 1000 and 5000Å which is typical in making high-efficiency solar cells.

Figure 1 shows the thickness dependence of the V_{oc} of a-Si alloy solar cells as a function of hydrogen dilution. R refers to the standard dilution that we use in our laboratory for obtaining the highest cell efficiency. For each experiment, several devices are measured and data recorded. For regular dilution R, the V_{oc} is essentially independent of the intrinsic layer thickness for up to 5000Å indicating that the intrinsic layer is still amorphous. In these samples, the variation of V_{oc} on a given substrate is very small. As the dilution is increased to 1.2R and for a thickness of less than 3000Å, the V_{oc} remains nearly constant. Beyond 3000Å, however, some cells exhibit lower V_{oc}. For a thickness of 5000Å, the dispersion in V_{oc} becomes large and the lowest value of V_{oc} is lower than that of the 3000Å cell. For the 1.4R samples, the value of V_{oc} becomes progressively lower and shows a spread even for a 1600 Å-thick device. In fact, the dispersion for the 5400Å sample is as large as 200mV. A higher dilution of 1.6R resulted in a further decrease in V_{oc}. In addition, as the cell thickness reaches 5000Å, there is a substantial microcrystalline inclusion in the device, which is reflected by the smaller spread in V_{oc} and its low value. At the highest dilution (2R), V_{oc} drops to ~0.5V even

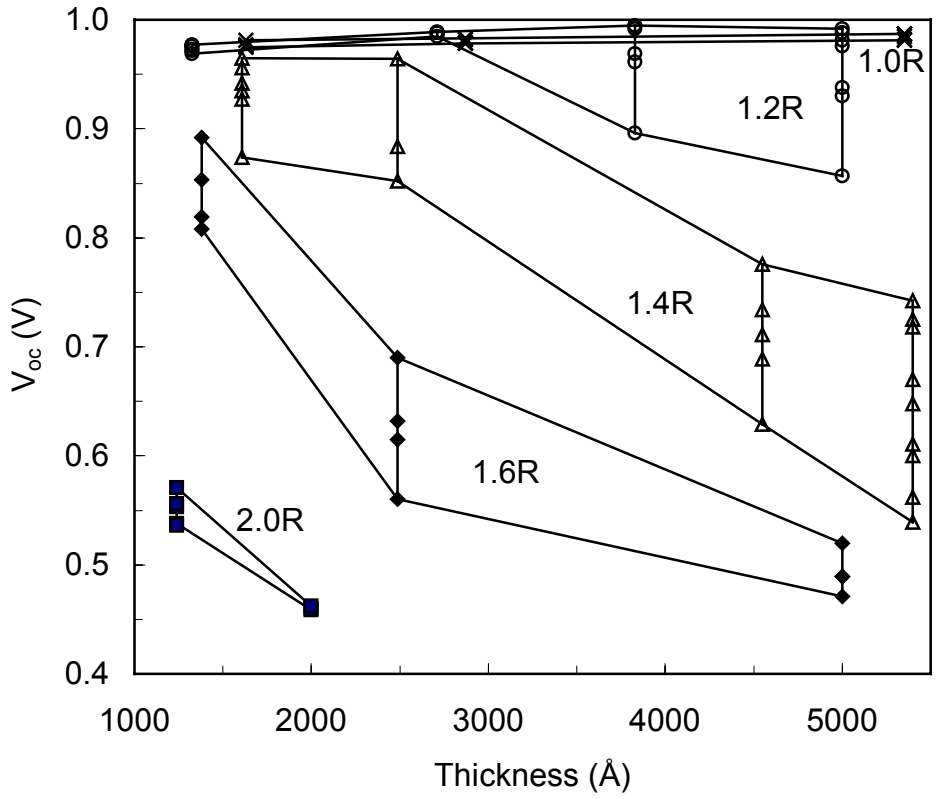

Figure 1. Thickness dependence of V_{oc} of a-Si alloy cells deposited with different hydrogen dilution.

for the smallest thickness. A factor of two change in hydrogen dilution can result in a substantial change in V_{oc}, from 1V to 0.5V. When the material is 'on the edge', any small variation in deposition conditions can push the material over the edge. For the best quality material, it is thus advisable to find the "edge" conditions and then reduce the hydrogen dilution somewhat to arrive at a more desirable region.

The thickness dependence of V_{oc} on a-SiGe alloy solar cells with ~40% Ge has also been studied and the results are plotted in Fig. 2. The following observations are made. First, due to the narrow bandgap of the a-SiGe alloy, V_{oc} takes on lower values. Second, for a dilution of 1.4R, V_{oc} remains rather constant and without much dispersion for a thickness of up to ~3000Å. This is in contrast to the case of a-Si alloy where 1.4R has already resulted in a spread in V_{oc} (see Fig. 1). Third, the amorphous-to-microcrystalline transition occurs at >1500 Å for the 1.9R cell, which is characterized by a lowering and spread in V_{oc}. This is again in contrast with the a-Si alloy in that a dilution of 2R has already pushed a-Si alloys over the edge. We should point out that the optimization of a-SiGe alloy solar cells is more complex than the a-Si alloy cells. Other deposition parameters can significantly influence the cell performance. While the dependence of V_{oc} on the thickness and dilution can serve as a guide to establish the threshold for a given set of deposition parameters, one must also optimize other conditions to assure good cell performance.

From Figs. 1 and 2 it is observed that for a cell thickness of ~2000Å, the spread in V_{oc} occurs near 1.4R for a-Si alloys, and near 1.9R for a-SiGe alloys. The fact that the critical dilution for amorphous-to-microcrystalline transition increases with incorporation of Ge is not surprising. It is well known that one can obtain more ordered material if the adatom mobility of the impinging species on the growing surface is large (Matsuda 1996). Hydrogen dilution is believed to passivate the growing surface so as to increase the adatom mobility, and this explains the improved order with increasing hydrogen dilution resulting eventually in the formation of microcrystallites. The predominant species for the growth of high quality a-SiGe alloys are SiH_3 and GeH_3. Since GeH_3 is heavier than SiH_3, a higher hydrogen dilution is necessary as the Ge-content increases to give the GeH_3 species enough mobility at the growing surface.

We have previously shown that profiling of Ge-concentration as a function of thickness increases the built-in field within the cell and helps the hole transport (Guha et al. 1989). The highest cell efficiency was obtained in a cell where the Ge-concentration was changed continuously with the highest amount near the *p-i* interface. Since the optimum hydrogen dilution depends on the Ge-concentration, we have changed the hydrogen dilution during the growth of the intrinsic layer as a function of thickness with the dilution being the highest when the Ge-content is the highest. The results on two cells of the same thickness, with and without profiling of hydrogen dilution during growth, are shown in Table 1. The cells were deposited on stainless steel substrate with silver/zinc oxide back reflector; and measurements were made under global AM1.5 illumination with a cut-on filter of wavelength greater than 610nm to more appropriately evaluate the a-SiGe alloy solar cells. It is clearly seen that hydrogen dilution profiling improves the fill factor of the cell, indicating a better transport property of the minority carriers.

Table 1. Current-Voltage Characteristics of Graded Bandgap a-SiGe Alloy Solar Cells With and Without Hydrogen Profiling.

Hydrogen Profiling	J_{sc} (mA/cm^2)	V_{oc} (V)	FF	P_{max} (mW/cm^2)
Yes	9.25	0.782	0.642	4.64
No	9.35	0.785	0.608	4.46

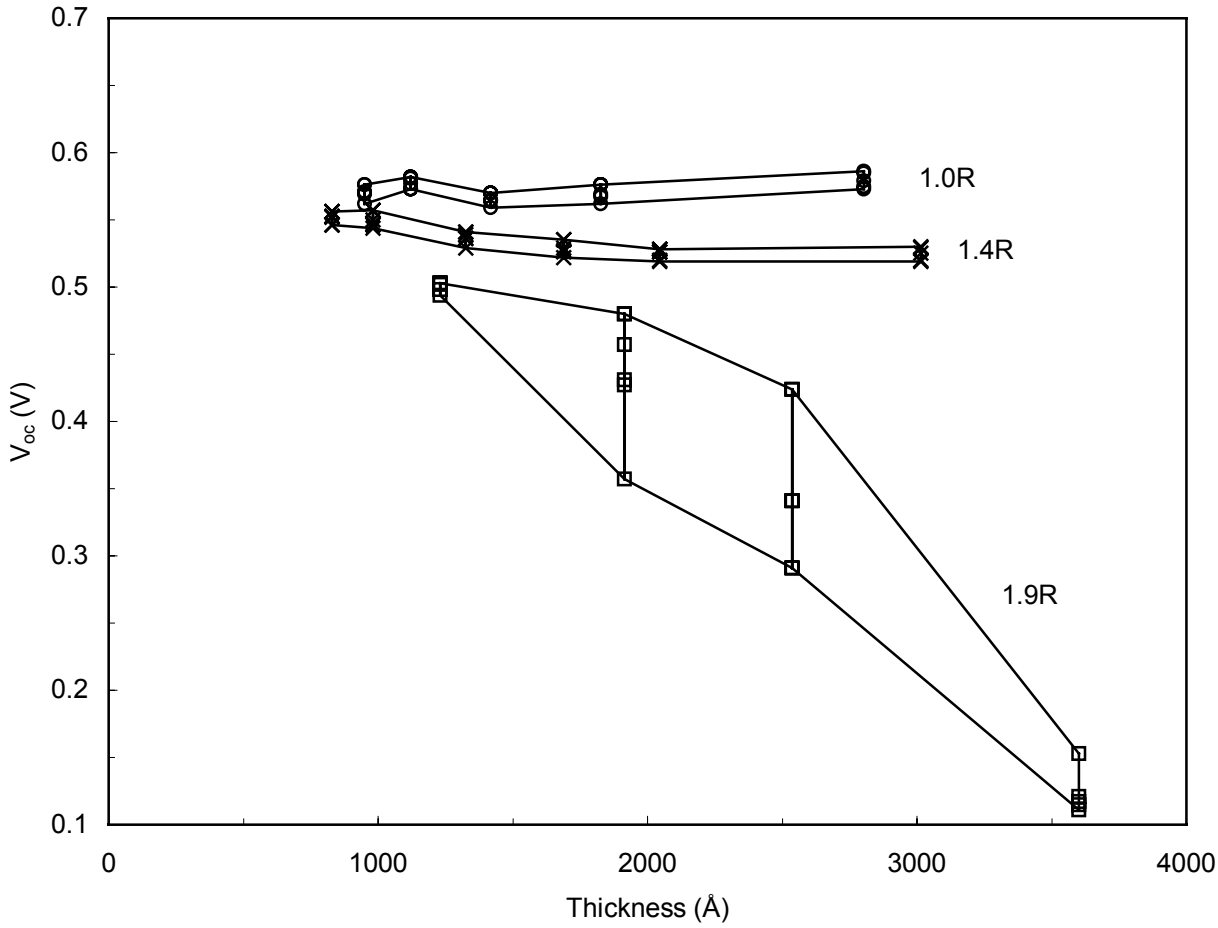

Figure 2. Thickness dependence of V_{oc} of a-SiGe alloy cells deposited with different hydrogen dilution.

It is also interesting to point out that profiling of hydrogen dilution improves the quality of both a-Si and a-SiGe alloy solar cells, but the profiling directions are different. For a-Si alloy cells, since there is a tendency toward transition to microcrystallinity with increasing thickness, the dilution has to be reduced as the film thickness increases. For the a-SiGe alloy with the graded bandgap structure, on the other hand, since the Ge-concentration increases as a function of thickness, the hydrogen dilution has to increase as the thickness increases.

We have used the measurement of V_{oc} as a tool to obtain the amorphous-to-microcrystalline transition in a-Si and a-SiGe alloy solar cells. For a given thickness, the critical amount of hydrogen dilution at the threshold is found to increase as the Ge-concentration increases. This has helped us in designing high efficiency graded bandgap a-SiGe alloy solar cells in which hydrogen dilution increases with increasing Ge-content during the growth of the intrinsic layer.

2.3. Increase in V_{oc} with Light Soaking of Mixed Phase Solar Cells

The best a-Si alloy solar cells have been made at a dilution ratio just below the onset of microcrystallinity (Yang et al. 1997, 1999). Raman scattering and high-resolution transmission electron microscopy revealed that the high quality intrinsic material contains intermediate-ordered chain-like objects, suggesting a heterogeneous structure (Tsu et al. 1997, 2001). As the dilution ratio is increased and exceeds a certain threshold value, the microcrystalline volume fraction grows and results in a mixed-phase structure, finally reaching a substantially microcrystalline configuration. In addition, we have found that there is onset of partial microcrystallinity as the films grow thicker and is accompanied by a sharp drop in the solar cell open-circuit voltage (V_{oc}) (Guha et al. 1999).

Light soaking and annealing experiments were conducted on a series of a-Si:H *n i p* solar cells prepared using a wide range of hydrogen-dilution ratios. The resultant solar cells exhibit initial V_{oc} ranging from greater than 1.0V to less than 0.5V, encompassing the amorphous, mixed-phase, and microcrystalline intrinsic layers. After one-sun light soaking at 50°C for 150 hours, cells in the amorphous and microcrystalline regions show a small reduction in V_{oc}, while those in the mixed phase display an enhancement of various amounts in V_{oc}. Subsequent annealing substantially restores the original V_{oc} values. An increase of as large as 150mV, representing a 20% V_{oc} enhancement, is observed for some cells after an intense 30-sun light soaking for 2 hours. We believe that the light-induced enhancement in V_{oc} can be attributed to a decreasing microcrystalline volume fraction and/or size during light soaking.

a-Si:H *n i p* solar cells were deposited on stainless steel substrate using a radio-frequency glow discharge technique. Indium tin oxide (ITO) dots of 0.05cm^2 were deposited on top of the *p* layer as the top contact. Each substrate contains typically over 30 ITO dots on a 4cm x 4cm area. The intrinsic layer was deposited using a wide range of hydrogen-dilution ratios to produce solar cells of amorphous, mixed, and microcrystalline phases. Current density versus voltage (J-V) characteristics was measured at 25°C under AM1.5 illumination and also in the dark. Unless otherwise specified, light soaking was conducted under one-sun intensity at 50°C and annealing was done at 150°C for 2 hours.

Figure 3 plots the dependence of initial V_{oc} versus hydrogen dilution for cells with an intrinsic layer thickness of 2500Å, where R refers to the standard dilution ratio we use in our laboratory for obtaining the highest efficiency solar cells (Yang et al. 1997). As the dilution is increased and approaches R=1, V_{oc} shows a slight increase, due to a slight widening of the optical bandgap and improvement of intermediate-range order (Yang et al. 2000). As the dilution is further increased to R>1.2, V_{oc} begins to drop sharply and shows a large degree of dispersion, reflecting the heterogeneous nature of the material over the 4cm x 4cm substrate area. The lowering of V_{oc} can be correlated to an increase of volume fraction and size of low-bandgap microcrystallites that are embedded in a high-bandgap amorphous matrix. As the dilution approaches R~2, the dispersion diminishes and converges to a low V_{oc} value of ~0.45V, indicating a substantial microcrystalline inclusion.

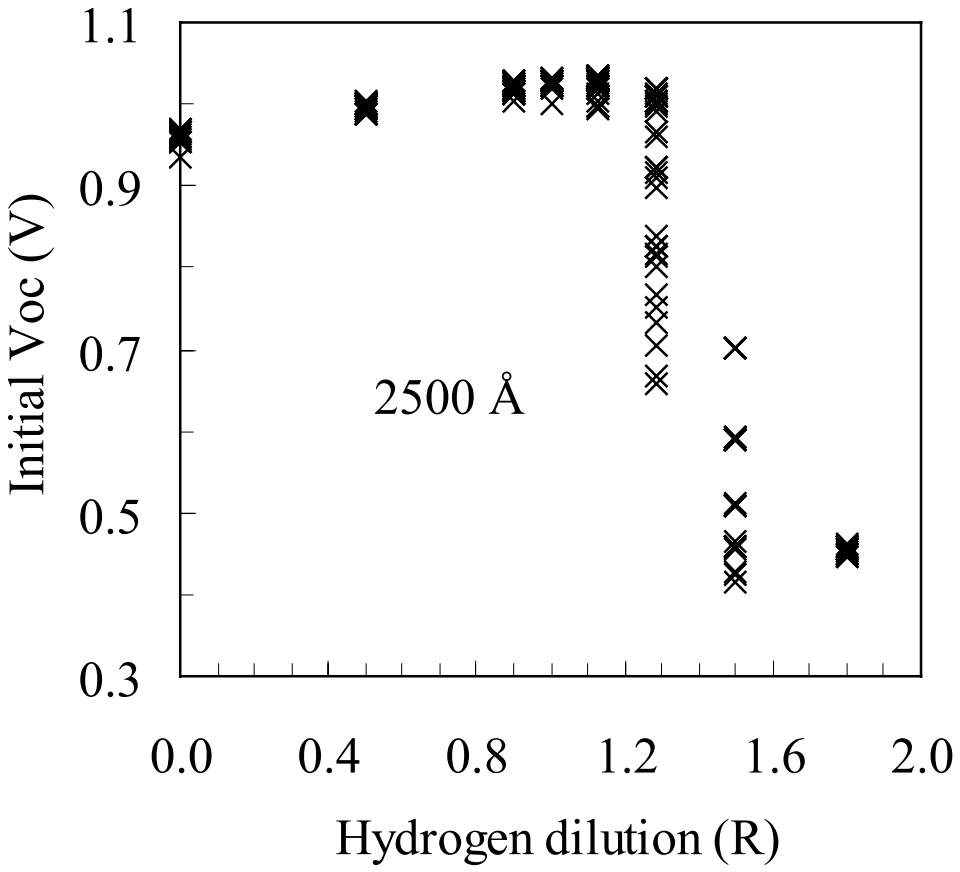

Figure 3. Dependence of initial V_{oc} on hydrogen dilution ratio.

The effect of light soaking on V_{oc} for the cells with $0.8 < R < 1.6$ is plotted against the initial V_{oc} in Fig. 4. For the cells in the substantially microcrystalline ($V_{oc} < 0.5$ V) and amorphous ($V_{oc} > 1$ V) regions, light soaking causes a small reduction in V_{oc}. For the mixed-phase cells, light soaking gives rise to an increase in V_{oc} of various amounts. For the cells with initial V_{oc} slightly higher than 0.5V or slightly lower than 1V, the increase is small. The largest increase occurs around V_{oc}=0.8V, nearly halfway between 0.5V and 1V. We have also light soaked cells having a thicker (~5000Å) intrinsic layer. The V_{oc} increase is more pronounced and shows a symmetric behavior with the largest increase centered near V_{oc} = 0.75V (see Fig. 4). For cells with an *i*-layer thickness of ~1μm, the V_{oc} increase is even higher and exceeds 100 mV. We have also light soaked a 5000Å i layer cell under an intense 30-sun light for 2 hours, and a dramatic increase of 150mV or 20% of the original V_{oc} is observed near V_{oc} = 0.7V; the data are also included in Fig. 4. We should point out that the majority of the V_{oc} increase under one-sun intensity occurs in less than 20 hours. Additional light soaking produces only a marginal increase. All the V_{oc} changes due to light soaking are substantially restored upon subsequent annealing at 150°C for 2 hours. Annealing of the cells prior to light soaking has little effect on the initial V_{oc}.

In addition, we have studied dark J-V characteristics of the cells with different phases before and after light soaking. Figure 5(a) shows dark J-V for a cell in the amorphous region with an initial V_{oc} = 1.030V. A straight line representing a typical diode characterized by $J=J_o \exp(qV/nkT)$ is observed. After light soaking, the quality factor n is increased from 1.80 to 1.84 and the saturated current density J_o goes up from 7.5×10^{-13}A/cm^2 to 2.8×10^{-12}A/cm^2, consistent with an increase in defect density and recombination due to the Staebler-Wronski effect (Staebler 1977). For cells in the microcrystalline region, dark J-V (not shown) exhibits high currents throughout the voltage range measured, and simply shifts to even higher currents after light soaking. For cells in the mixed phase that show a large increase of V_{oc} after light soaking, the initial dark J-V exhibits a two-segment feature as shown for a cell with an initial V_{oc} = 0.843V in Fig. 5(b). After light soaking, the dark current in the low-voltage ($V < 0.4$V) segment increases and is similar to the amorphous case of Fig. 5(a). In contrast, the dark current in the high-voltage ($V > 0.4$V) segment is suppressed after the light soak implying an increase in the resistance of the material or increase in the barrier height of the diode.

Based on the above experimental data, we now discuss possible causes for the V_{oc} increase. We propose that the increase is associated with a reduction in the microcrystalline volume fraction or size. We suggest that the material in the mixed phase is unstable; the volume fraction or the size of the microcrystallites in this material could change easily as is apparent from the scatter in the V_{oc} values, even in solar cells on the same sample across its surface area. When the volume fraction or size of the microcrystallites is very small ($V_{oc} > 1$V) or very large ($V_{oc} < 0.5$V), the carrier transport and cell performance are dominated by their respective amorphous or microcrystalline properties. Only when the microcrystallinity is in the mixed-phase transitional region does the change in the microstructure affect the V_{oc} significantly. This explains the observed dependence of the V_{oc} increase with respect to the initial V_{oc}.

Light exposure has been shown to cause structural changes in the material, and the reduction in the volume fraction or size of the microcrystallites could result from this structural change. Moreover, recent studies on the light-induced volume expansion show a larger effect on materials near the amorphous-to-microcrystalline transition region than in the amorphous region. This also supports the view that the material in the transition region is less stable. These studies are consistent with our observations. The notion that the change in V_{oc} is caused by the changes in the microstructure is also consistent with the dark J-V characteristics of Fig. 5 (b). The fact that the high-voltage segment shows a reduced current after light soaking can be explained as resulting from a reduction in the microcrystalline fraction.

Although it is reasonable to argue that a change in the volume fraction or size of the microcrystallites can cause the observed V_{oc} variation, the process of the microstructure change is not well understood. Grain boundaries can produce a significant effect in the hydrogen-induced conversion of crystallites to amorphous

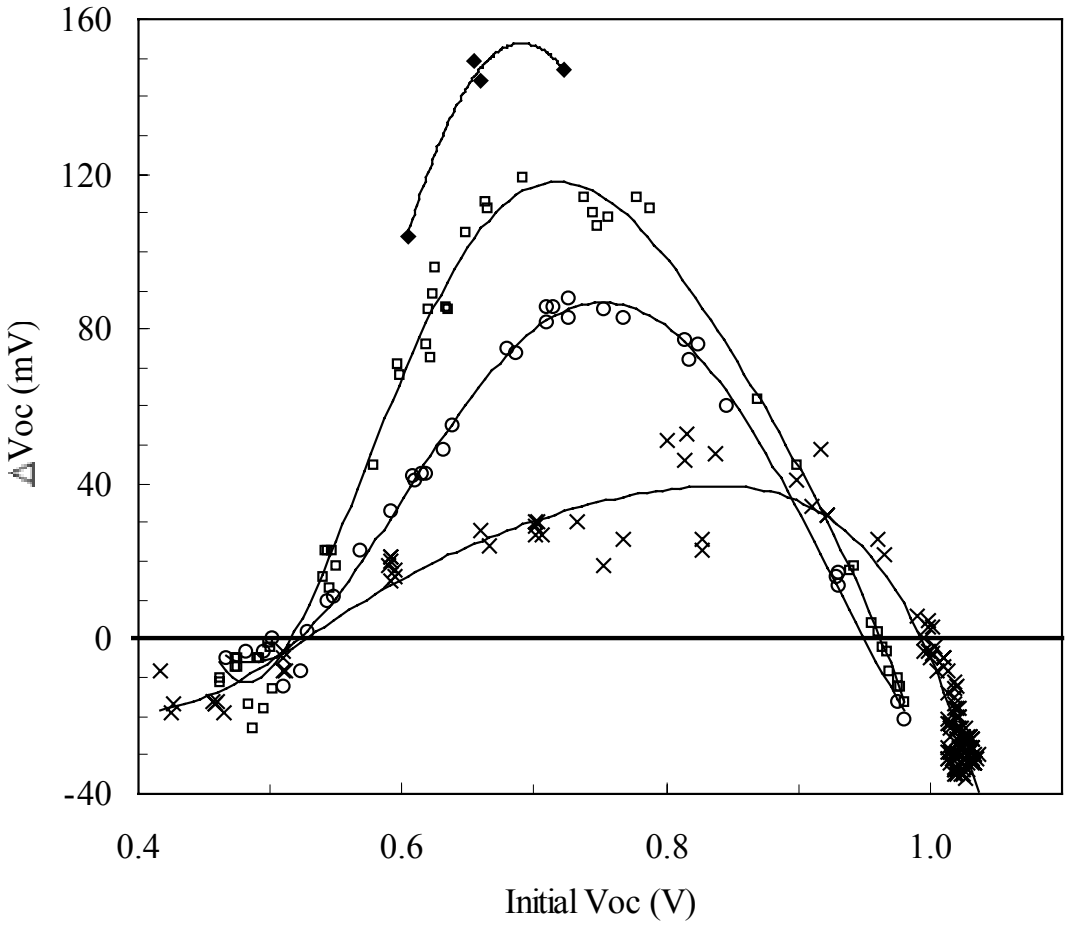

Figure 4. One-sun light-induced changes in V_{oc} versus initial V_{oc} for cells with *i* layer thickness of 2500Å (x), 5000Å (o), and 1μm (□). ◆ denotes changes produced by 30-sun light soaking on a 5000Å cell. The solid lines are polynomial fits to the data and serve as a guide to the eye.

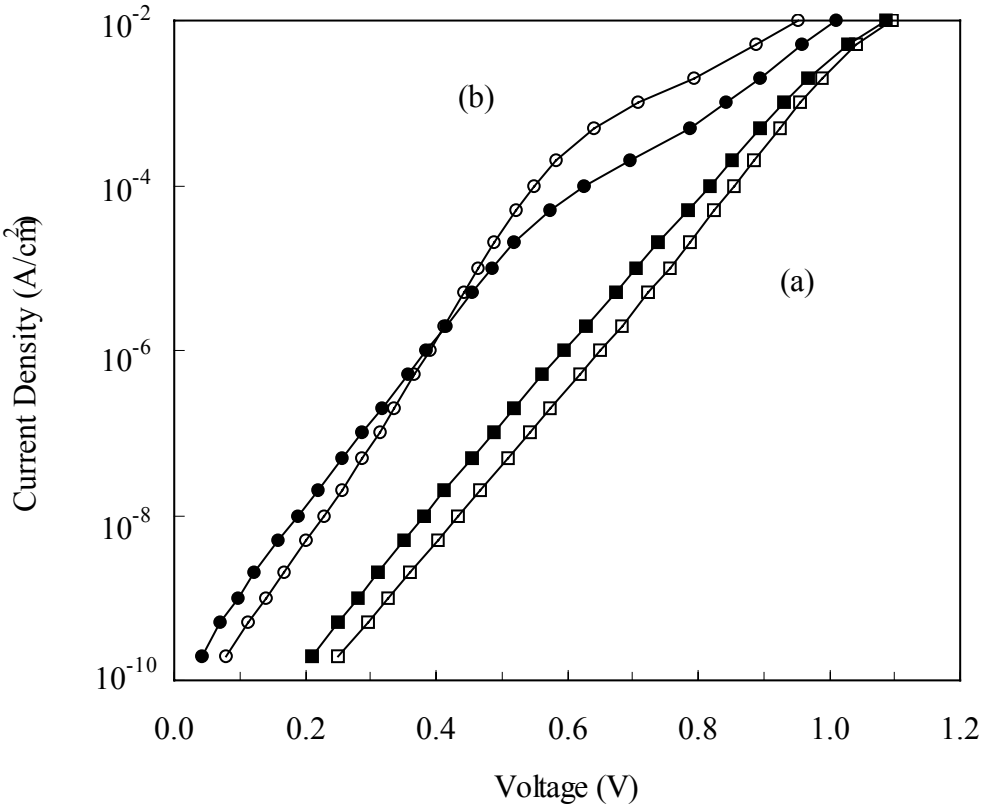

Figure 5. Dark J-V characteristics of solar cells in the (a) annealed (□) and light-soaked (■) states in the amorphous phase, and (b) annealed (○) and light-soaked (●) states in the mixed phase.

silicon, a process that reduces the strained Si-Si bonds. Nuclear magnetic resonance and infrared spectroscopy confirm that in an amorphous matrix containing crystallites, most of the hydrogen clusters in the grain boundaries (Mahan et al. 2000). It is reasonable to assume that the hydrogen content in the crystallites is much lower than the grain boundaries. There exist many strained (or weak) Si-Si bonds in crystallites near the grain boundaries. During light soaking, some strained Si-Si bonds are broken; hydrogen moves in and terminates some of the broken bonds. This effectively causes the shell layer of the grains to become more disordered. Although the microscopic picture is complicated, we can expect two consequences: the defect density increases after light soaking, and the region near the grain boundaries becomes more disordered or changes to amorphous. The latter reduces the size of the grains and the microcrystalline volume fraction, thus the enhanced V_{oc}.

We should point out that previous studies have reported observations of small (<50 mV) V_{oc} increases after light soaking (Isomura et al. 1998, Yang et al. 1994, Siamchai et al. 1995, Longeaud et al. 1999, Roca i Cabarrocas et al. 1998). However, the cause of the increase was attributed to a light-induced activation of boron in the *p* layer (Roca i cabarrocas et al. 1998), a voltage shift in the dark J-V characteristics (Isomura et al. 1998), or not given (Yang et al. 1994, Siamchai et al. 1995, Longeaud et al. 1999). In this study, we observe a much larger effect that depends on the bulk properties of the solar cells such as the intrinsic layer thickness or microcrystallinity. The phenomenon is observed only for cells in the mixed phase with the maximum effect occurring in the middle of the amorphous-to-microcrystalline transition region. We suggest the light-induced effect is due to a reduction in the microcrystalline volume fraction or size.

Using optimized hydrogen dilution, state-of-the-art single-junction, top, middle, and bottom component cells have been fabricated. The single-junction cells have characteristics optimized for use in the triple-junction structure. The top cells are a-Si alloy with a bandgap of 1.8eV and deposited on bare stainless steel substrates. The top cells were characterized under an AM1.5 global spectrum. The middle component cells are a-SiGe alloy with a band gap of ~1.6eV and were deposited on bare stainless steel substrates. The middle cells were characterized under an AM1.5 global spectrum with a λ>530nm filter. The bottom cells, also a-SiGe alloys with a bandgap of ~1.4eV, were deposited on a textured Ag/ZnO coated stainless steel substrate. The bottom cells were characterized under AM1.5 global illumination with a λ>630nm filter. The characteristics of the improved cells which are the best obtained to date are listed in Table 2. With improved hydrogen dilution, the stabilized total-area P_{max} of the top, middle, and bottom cells are 5.74 mW/cm^2, 3.92 mW/cm^2, and 3.92 mW/cm^2, respectively.

Table 2. Total-Area J-V Characteristics of Component Cells Deposited with Optimized Hydrogen Dilution.

Cell	State	J_{sc} (mA/cm^2)	V_{oc} (V)	FF	P_{max} (mW/cm^2)
Top	initial	8.4	1.024	0.773	6.65
	stable	8.1	0.990	0.711	**5.74**
Middle	initial	9.6	0.754	0.679	4.90
	stable	9.0	0.722	0.600	**3.92**
Bottom	initial	11.3	0.631	0.671	4.81
	stable	10.3	0.609	0.622	**3.92**

2.4. Microdoping

Amorphous silicon solar cells fabricated with hydrogen dilution near the amorphous to microcrystalline transition edge exhibit the best initial and stabilized performance. It was reported (Sheng et al. 2001) that subtle doping with boron in a-Si films near this transition edge reduces the number of sub-bandgap states in the initial and light soaked states as measured by the constant photocurrent method. Microdoping with

boron was proposed to prevent microcrystallite formation, promote the ordered growth and reduce the states associated with the microcrystallites.

We fabricated several a-Si alloy solar cells with increased hydrogen dilution with varying levels of boron doping. Accompanying films were deposited on 7059 glass in order to measure the activation energy to assess the shift in the Fermi level with doping. Light J-V characteristics of the solar cells were measured in the initial and light soaked states. The initial light J-V characteristics were found to degrade with increasing boron microdoping. Additionally, the stability of the light J-V characteristics was not improved with boron microdoping.

Table 3 lists the initial and light-soaked J-V characteristics of cells deposited with the varying hydrogen dilution ratios and boron doping. As the boron doping is increased in the cells deposited with the optimum hydrogen dilution, the initial performance becomes worse. The light induced degradation, however, is similar (~17%) for the cells deposited with and without boron doping.

The cells deposited with higher hydrogen dilution (on-the-edge) exhibit lower initial and stabilized efficiencies than the cells deposited with the optimal hydrogen dilution. The lower performance is due to the increased microcrystallite content. The light induced degradation for all of these cells, however, is less ~10%. The performance of the cell deposited with 10ppm BF_3 is similar to the cell with no BF_3, and the performance of the cell deposited with 25ppm BF_3 is considerably worse.

Further increases in the hydrogen dilution results in even lower initial and stabilized performance. So far we have not observed any improvement from the use of boron microdoping on the initial or light-soaked performance of solar cells. One possible explanation is that the parameter space used by Sheng *et al.* may not permit the growth of ordered material without considerable microcrystalline growth. The parameter space used at United Solar Systems Corp. may allow for a more ordered growth without the need for boron to inhibit microcrystalline growth.

2.5. Summary

The use of hydrogen dilution during deposition was extensively studied over the course of the contract. A 13% stable cell and a 10.5% aperture-area module were reported using a triple-junction structure. The best material is obtained at a dilution just below the threshold of amorphous-to-microcrystalline transition. This material has an improved intermediate range order and may contain a small volume fraction of microcrystallites. Profiling of the hydrogen dilution was found to improve cell performance for both a-Si and a-SiGe alloys. The profiling directions are different, decreasing with thickness for a-Si alloys and increasing for a-SiGe alloys. These studies have led to a systematic method for depositing the best cells to date.

Table 2. Initial and Light Soaked J-V Characteristics of a-Si Alloy Cells Deposited with Various BF_3/Si_2H_6 Ratios.

Hydrogen dilution	BF_3 (ppm BF_3/Si_2H_6)	Conditions	J_{sc} (mA/cm^2)	V_{oc} (V)	FF	P_{max} (mW/cm^2)	Deg. (%)
optimum	0	Initial	11.90	1.010	0.687	8.26	
		500hrs	11.40	0.972	0.615	6.81	17
optimum	1	Initial	11.60	1.004	0.686	7.99	
		500hrs	11.20	0.970	0.620	6.74	16
optimum	5	Initial	11.50	0.998	0.693	7.95	
		500hrs	11.20	0.972	0.617	6.72	16
optimum	10	Initial	11.30	1.009	0.685	7.81	
		500hrs	10.80	0.968	0.618	6.46	17
optimum	25	Initial	11.70	1.006	0.665	7.83	
		500hrs	11.00	0.965	0.607	6.44	18
optimum	50	Initial	11.50	0.996	0.638	7.31	
		500hrs	10.70	0.960	0.585	6.01	18
on-the-edge	0	Initial	10.7	0.987	0.709	7.49	
		500hrs	10.4	1.000	0.649	6.75	10
on-the-edge	10	Initial	10.6	1.005	0.718	7.65	
		500hrs	10.3	1.002	0.661	6.82	11
on-the-edge	25	Initial	10.8	0.979	0.697	7.37	
		500hrs	10.1	0.989	0.658	6.57	11
over-the-edge	0	Initial	11.2	0.812	0.595	5.41	
		500hrs	10.8	0.826	0.559	4.99	8
over-the-edge	10	Initial	10.8	0.849	0.611	5.60	
		500hrs	10.6	0.855	0.563	5.10	9
over-the-edge	25	Initial	11.1	0.800	0.443	3.93	
		500hrs	11.1	0.755	0.405	3.39	14
over-the-edge	0	Initial	12.3	0.480	0.506	2.99	
		500hrs	11.6	0.449	0.448	2.33	22
over-the-edge	10	Initial	12.1	0.610	0.353	2.61	
		500hrs	11.7	0.565	0.342	2.26	13
over-the-edge	25	Initial	12.5	0.526	0.360	2.37	
		500hrs	11.9	0.471	0.352	1.97	17

Section 3

Status of a-Si Alloy Solar Cells Deposited with RF at 3Å/s

3.1. Introduction

Efforts were made to increase the total-area efficiencies of the triple-junction cells deposited by 13.56MHz RF at 3Å/s. Such a high deposition rate does not produce the best quality cells. However, this work is important in view of the fact that most manufacturing plants employ a deposition rate ~3Å/s in order to save on costs. The deposition parameters, such as hydrogen dilution, were optimized for best performance. Small-area cells (total-area = 0.268cm^2, active-area = 0.25cm^2) were evaluated with J-V and quantum efficiency measurements. The light J-V measurements were made under an AM1.5 global dc-source ORC solar simulator. The light soaking was done under one-sun, 50^{0}C, and open-circuit conditions for >1000 hours. To evaluate the performance of the triple-junction devices, single-junction *n i p* cells were fabricated in a similar manner to the triples. Top and middle component cells were deposited directly onto stainless steel substrates; bottom cells were deposited on stainless steel substrates precoated with silver/zinc oxide back reflectors. Indium tin oxide (ITO) dots were used to isolate sixteen 0.268 cm^2 devices on each 2" x 2" substrate. Finally, gold grids were evaporated on the 0.268cm^2 cells.

3.2. Component Cells

Single-junction a-Si alloy top cells were deposited on stainless steel substrates at 3Å/s. The J-V characteristics were measured under an AM1.5 global spectrum. The stable results of cell BMW3405 were obtained after 1000 hours of light soak. The initial and stabilized characteristics are listed in Table 4. The total-area P_{max} degraded by 20% from 5.9% to 4.7%.

Table 4. Initial and Stable J-V Characteristics of an a-Si Alloy Top Cell Deposited at 3Å/s on Stainless Steel Substrate.

Sample BMW	Active-area (cm^2)	Total-area (cm^2)	Light Soak (Hours)	J_{sc} (mA/cm^2)	V_{oc} (V)	FF	P_{max} (mW/cm^2)	
							Active-area	Total-area
3405	0.25	0.268	0	8.73	0.967	0.749	6.3	5.9
			1000	8.56	0.904	0.646	5.0	4.7
Phase III milestone		***1.0***	***1000***					***5.1***

Single-junction a-SiGe alloy middle cells were deposited at 3Å/s on stainless steel substrates. The cells were measured under an AM1.5 global spectrum filtered through a λ>530nm long-pass filter. The cell BMW4410 was light soaked for 1010 hours and the stable J-V characteristics measured. The initial and stabilized J-V characteristics are listed in Table 5. The total-area P_{max} > 530nm degraded by 28%, from 3.9 to 2.8mW/cm^2.

Table 5. Initial and Stable J-V Characteristics of an a-SiGe Alloy Middle Cell Deposited at 3Å/s on Stainless Steel Substrate (λ>530nm).

Sample BMW	Active-area (cm^2)	Total-area (cm^2)	Light Soak (Hours)	J_{sc} (mA/cm^2)	V_{oc} (V)	FF	P_{max}>530nm (mW/cm^2)	
							Active area	Total area
4410	0.25	0.268	0	9.26	0.710	0.632	4.2	3.9
			1010	8.83	0.666	0.518	3.1	2.8
Phase III milestone		***1.0***	***1000***					***3.2***

Single-junction a-SiGe alloy bottom cells were deposited at 3Å/s on Ag/ZnO coated stainless steel substrates. The cells were characterized under an AM1.5 global spectrum filtered through a λ>630nm long-pass filter. Cells BMW5832 and RF9473 were light soaked for 1000 hours and the stable characteristics measured. The initial and stabilized J-V characteristics are listed in Table 6. The stabilized total-area P_{max} > 630nm is ~3.2mW/cm^2 for both samples and meets the Phase III milestone of 3.2mW/cm^2.

Table 6. Initial and Stable J-V Characteristics of an a-SiGe Alloy Bottom Cell Deposited at 3Å/s on Ag/ZnO Back Reflector (λ>630 nm).

Sample	Active-area (cm^2)	Total-area (cm^2)	Light Soak (Hours)	J_{sc} (mA/cm^2)	V_{oc} (V)	FF	P_{max}>630nm (mW/cm^2)	
							Active area	Total area
BMW5832	0.25	0.268	0	10.42	0.613	0.638	4.1	3.8
			1000	9.96	0.587	0.583	3.4	3.2
RF9473	0.25	0.268	0	10.84	0.609	0.641	4.2	3.9
			1000	10.32	0.582	0.579	3.5	3.2
Phase III milestone		***1.0***	***1000***					***3.2***

3.3. Triple-Junction Cells

Triple-junction cells were deposited at 3Å/s on Ag/ZnO coated stainless steel substrates. Cell BMW3547 was light soaked under AM1.5 global for 1010 hours and the J-V characteristics measured. The cell was also measured by NREL. The stabilized J-V characteristics measured at United Solar and NREL are listed in Table 7 for two devices. The stabilized J-V and quantum efficiency plots are shown in Figs. 6 and 7, respectively.

Table 7. Initial and Stable J-V Characteristics of a Triple-junction Cell Deposited at 3Å/s Measured at United Solar and NREL.

Sample BMW3547	State	Total-area (cm^2)	J_{sc} (mA/cm^2)	V_{oc} (V)	FF	Active-area η(%)	Total-area η(%)
#42 United Solar	Initial	0.268	7.48	2.266	0.769	13.0	12.1
#42 United Solar	Stable	0.268	6.92	2.193	0.727	11.03	10.3
#42 NREL	Stable	0.2709	6.440	2.187	0.6905		9.7
#23 United Solar	Initial	0.268	7.48	2.286	0.758	13.0	12.1
#23 United Solar	Stable	0.268	6.92	2.193	0.721	10.94	10.2
#23 NREL	Stable	0.2700	6.751	2.181	0.6782		10.0

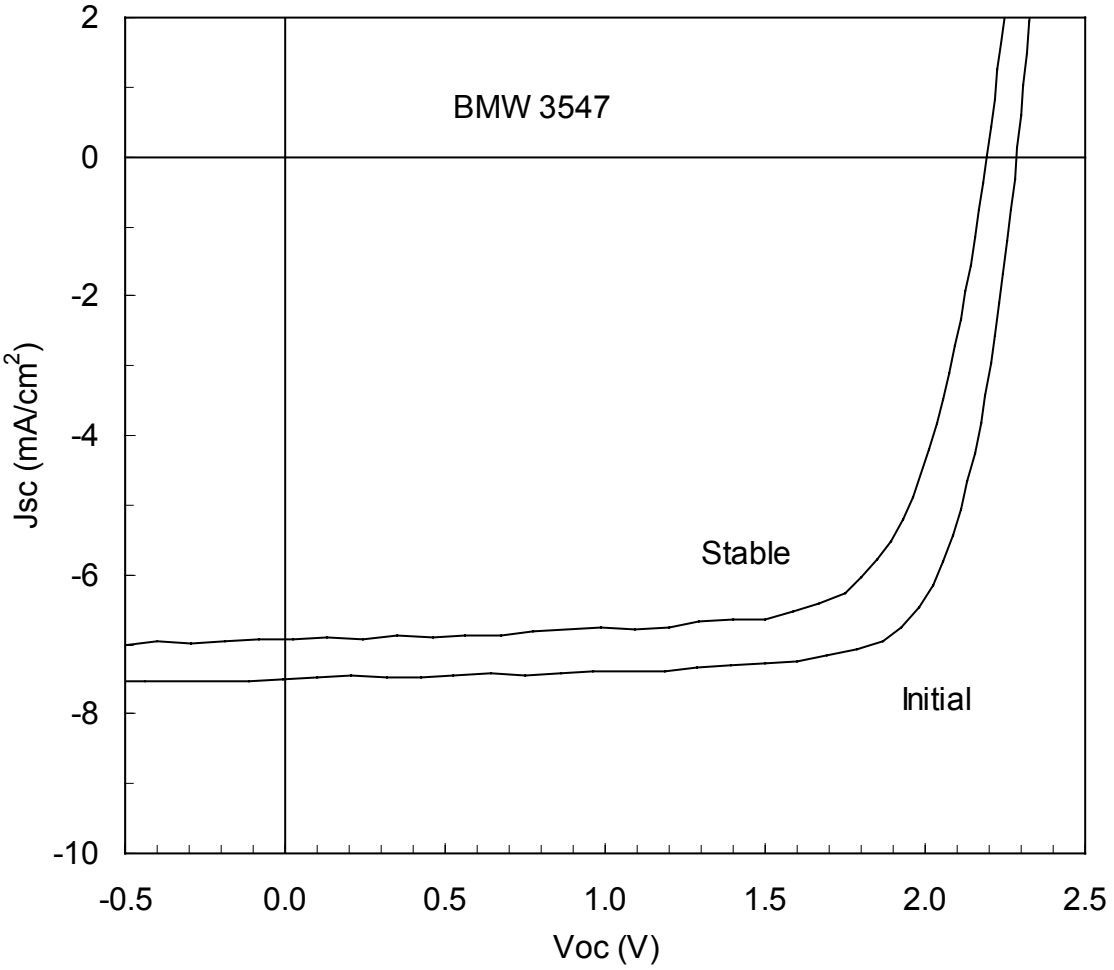

Figure 6. Initial and stabilized J-V characteristics of a triple-junction cell deposited at 3Å/s on an Ag/ZnO back reflector.

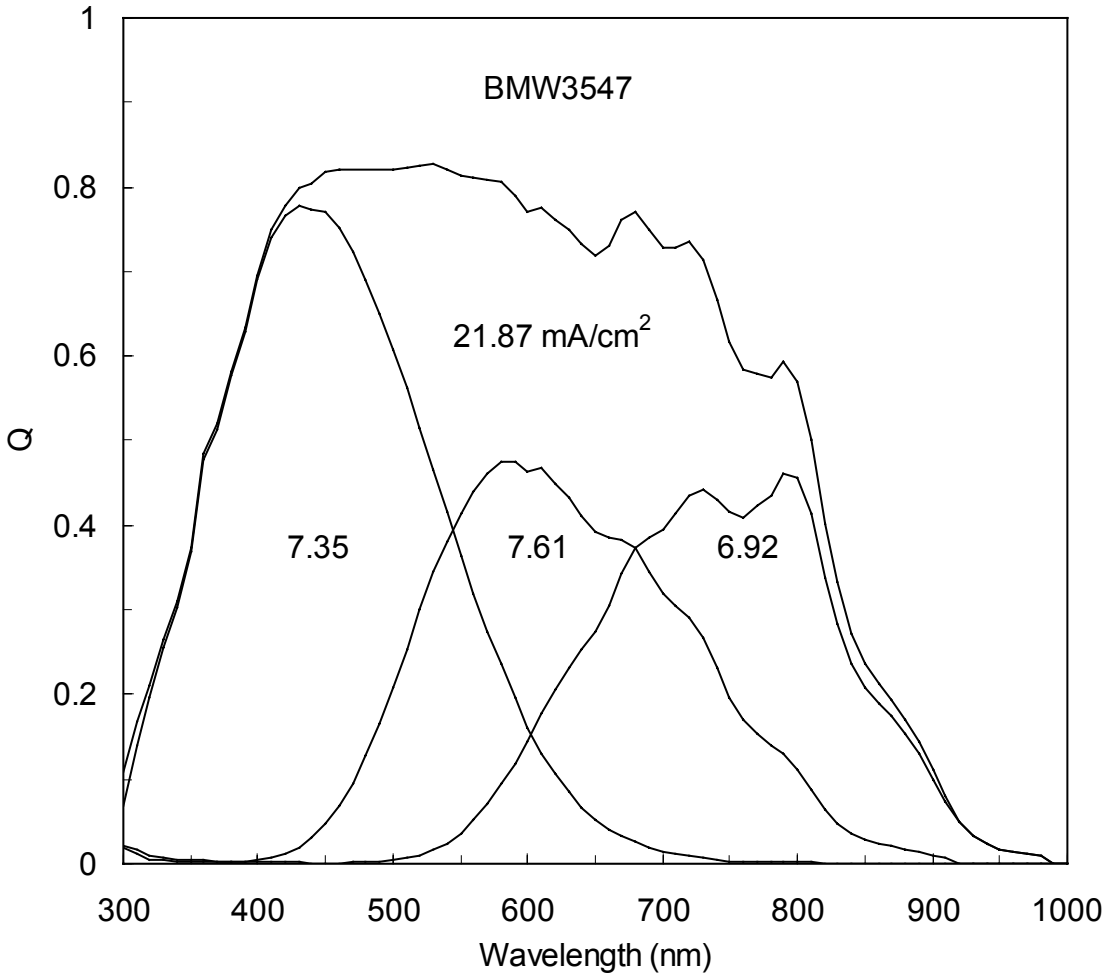

Figure 7. Stabilized quantum efficiency of a triple-junction cell deposited at 3Å/s.

Section 4

Modified Very-High-Frequency (MVHF) Plasma Enhanced Chemical Vapor Deposition of a-Si and a-SiGe Alloy Solar Cells at High Deposition Rates

4.1. Introduction

High deposition rates are attractive because of increased throughput and reduced manufacturing costs. RF (13.56MHz) and MVHF (75MHz) PECVD can be used to attain high deposition rates. In an earlier study, we have shown that an increase in the deposition rate of a-Si alloys using 13.56MHz led to an increase in microvoid density resulting in poorer cell performance and stability (Guha et al. 1992). We also found that the microstructure of the material depends critically on the deposition conditions such as the degree of hydrogen dilution during the film growth (Tsu et al. 1997). Solar cells made using 2.45GHz microwave excitation with a deposition rate of ~100Å/s have exhibited high initial efficiencies (Guha et al. 1995). An optimum deposition condition for high quality materials may exist for a given excitation frequency. Currently, the highest stabilized efficiencies are obtained using conventional RF-PECVD at a rate of 1Å/s. We have reported initial and stabilized active-area efficiencies of 14.6% and 13.0%, respectively, using the low-rate RF-PECVD technique (Yang et al. 1997).

More than ten years ago, Chatham and Bhat (Chatham et al. 1989) used very-high-frequency (VHF) PECVD to deposit a-Si alloy solar cells at high deposition rates. They demonstrated an efficiency of 9.7% for an a-Si alloy solar cell made at 18Å/s using a frequency of 110 MHz. Since then, many groups have used this technique to deposit a-Si alloy materials and devices. The group at Utrecht studied the properties of the VHF plasma (Harmers et al. 1997) and deposited a-Si alloy solar cells (Van Spark et al. 1996) and thin film transistors. They obtained an initial efficiency of 10% (Van Spark et al. 1996). The group at Neuchâtel showed that VHF-PECVD has advantages over RF-PECVD for depositing microcrystalline silicon (μc-Si) at high rates (Shah et al. 1997). They deposited μc-Si single-junction and a-Si/μc-Si double-junction solar cells.

In our laboratory, we have used an MVHF-PECVD (MVHF) system to deposit a-Si and a-SiGe alloy solar cells. We found that a-Si alloy solar cells made with MVHF at 6Å/s show similar initial performance as those made with RF at 3Å/s and the stability of 6Å/s MVHF cells is better than the 3Å/s RF cells (Yang et al. 1998). To further improve the performance of the MVHF solar cells made at high deposition rates, we need to understand the difference in the plasmas excited by RF and MVHF, and search for further improvement of the solar cells. For this purpose we have systematically studied the ion energy distribution of MVHF and RF plasmas as well as the effects of ion bombardment on the performance of a-Si and a-SiGe alloy solar cells. It has been shown that high H_2 dilution can improve the performance and stability of a-Si alloy solar cells made with RF plasmas at low deposition rates (Guha et al. 1981). However, the effect of H_2 dilution on the solar cells made with MVHF at high rates is not clear. Recent studies on the effects of H_2 dilution on the a-Si and a-SiGe alloy solar cells are summarized.

Both the initial performance and stability of single-junction a-Si alloy cells fabricated by MVHF at 6-10Å/s are superior to the 3Å/s RF a-Si alloy cells. High deposition rate a-SiGe alloy middle cells fabricated with RF and MVHF exhibit similar characteristics. MVHF bottom cells currently exhibit inferior initial and stabilized performance compared to the RF bottom cells.

4.2. Correlation of Process Parameters of MVHF Plasma and Device Performance of a-Si and a-SiGe Alloy Solar Cells

4.2.1. Ion Energy Distribution of RF and MVHF Plasma and the Effect of Ion Bombardment on a-Si and a-SiGe Alloy Solar Cells

A parallel plate capacitance reaction chamber (MVHF chamber), which was adapted to a multi-chamber PECVD system, was designed to have the capability to couple RF (13.65MHz) and VHF (75MHz) frequencies to the plasma. The substrate can be grounded, externally biased, or floated, which gives the flexibility to study the effects of ion bombardment. A retarding field analyzer was installed in the plasma chamber to measure the energy distribution of positive ions. The details of the ion energy distribution experiments are presented elsewhere (Yan et al. 1999). The ion energy distributions of H_2, Ar, SiH_4 and their mixtures were studied as functions of excitation frequency, RF or VHF power density and pressure. a-Si and a-SiGe alloy component cells were made with various conditions, such as different pressures, gas flow rates, substrate temperatures, and external biases.

Figure 8 shows the energy distribution of ions in H_2 plasma with 75MHz excitation, where the VHF power was 10W. At a low pressure (0.1 Torr), a sharp peak appears at 22eV with full width at half-maximum of ~6eV. The cut-off at the high-energy side is sharp. This value could be the plasma potential. However, at high pressure (1.0 Torr), the peak of ion energy distribution shifts to zero and the width becomes significantly broader. Similar measurements were carried out for the RF plasma. Figure 9 shows the energy distribution of the RF plasma with the same conditions as in Fig. 8 except that the excitation frequency was 13.56MHz. The peak position is much higher (37eV) than that shown in Fig. 8, and the distribution is also much broader (18eV). No high-energy ions reach the substrate at 1.0 Torr just as in the MVHF case. The positive ion current that reaches the substrate is about five times higher in the MVHF plasma than in the RF plasma.

The shifting and broadening of the ion energy distribution with the increase in pressure could result from the collision of positive ions with neutral species when the ions travel through the sheath. The collision not only transfers energy to neutral species but also has a probability to exchange charge. The charge-exchange collision yields low energy neutral radicals that reduce the energy of the ions as measured by the retarding field analyzer. This process is significant in Ar plasma since the charge-exchange collision cross-section is very large for Ar ions (Gallagher 1999). Experimentally, we found that the ion energy distribution collapsed even at low pressure for Ar plasma (0.1 Torr).

Compared with pure H_2 plasma, a mixture of SiH_4 and H_2 shifts the ion energy distribution to a lower energy, as shown in Fig. 10. This shift probably indicates that the plasma potential is higher for pure H_2 plasma than for the plasma with H_2 and SiH_4 mixture. This phenomenon is similar for both RF and MVHF plasmas.

The increase of excitation power slightly shifts the energy distribution of MVHF plasma to a higher energy as shown in Fig. 11. The shape of the ion energy distribution remains unchanged within experimental error. It probably means that the plasma potential is increased by the high power since the peak-to-peak voltage increases with the increase of power level. However, for an RF plasma there is no significant change at the cut-off energy, instead the shape of the distribution is changed. Figure 12 compares the ion energy distribution for RF plasma of 3W and 30W. Since the plots are in arbitrary units, we can only say that the ratio of the high-energy peak to the broad low-energy shoulder increases with the increase of RF power. The mechanism responsible for the difference in the power dependence between RF and MVHF is not clear at this stage.

From the ion energy distribution measurements we have learned the following. First, the ion bombardment occurs only at low pressures. For normal device deposition pressures, there is no significant ion

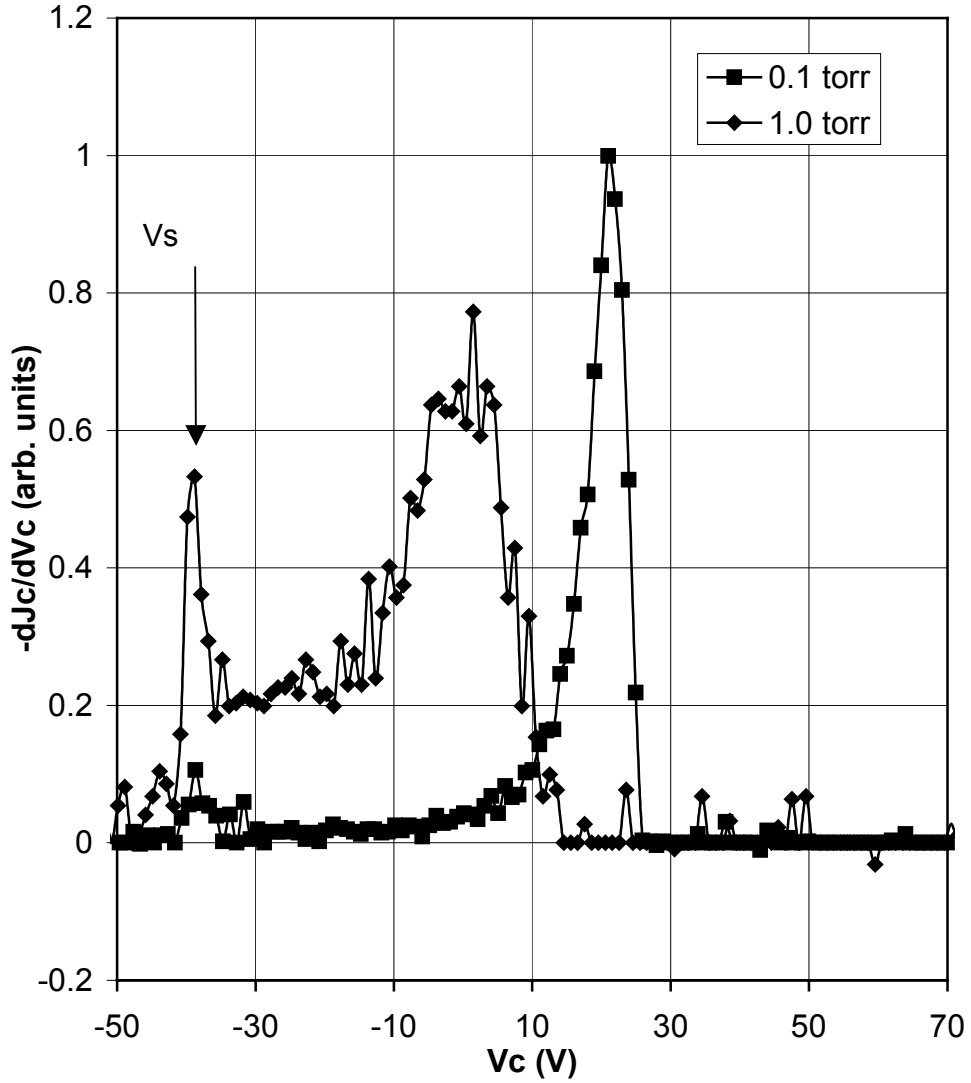

Figure 8. The energy distribution of positive ions reaching the substrate in a H_2 plasma excited by 75MHz VHF. The pressures were 0.1 and 1.0 Torr and VHF power was 10W.

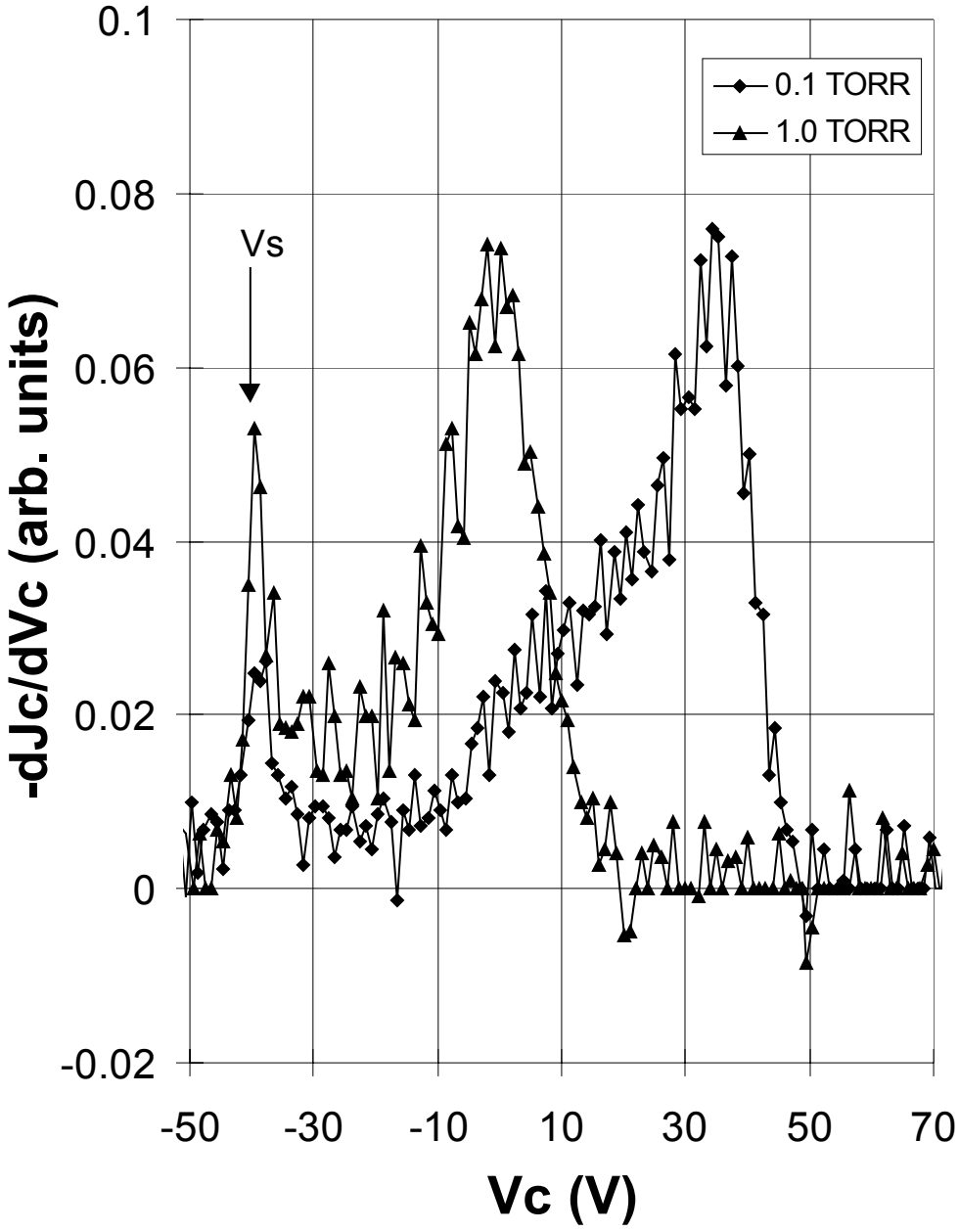

Figure 9. The positive ion energy distribution of a H_2 plasma excited by 13.56MHz RF. Other conditions are the same as in Fig. 8.

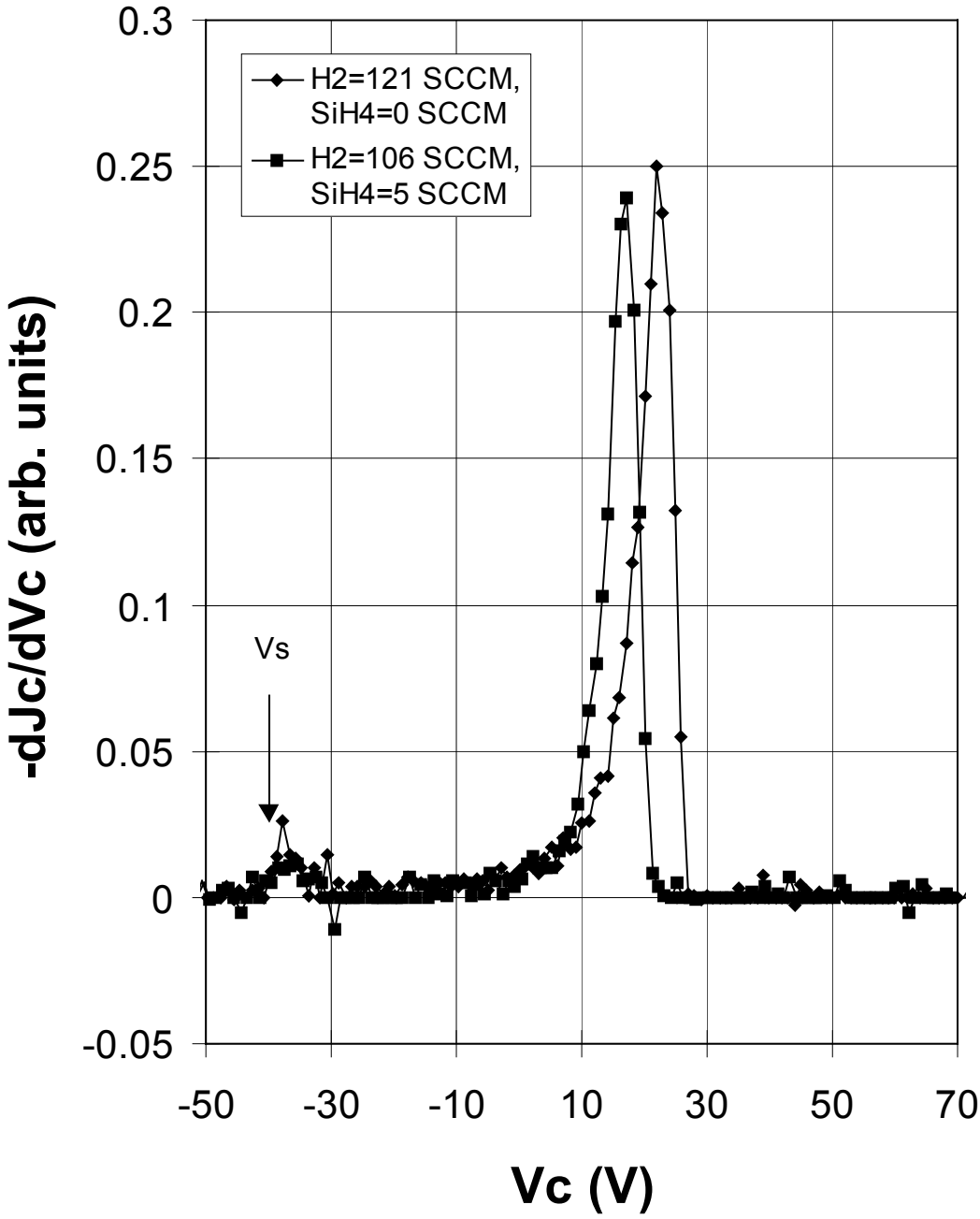

Figure 10. Comparison of the positive ion energy distribution of pure H_2 plasma and plasma with H_2 and SiH_4 mixture. The measurements were made at 0.1Torr with 11W VHF power.

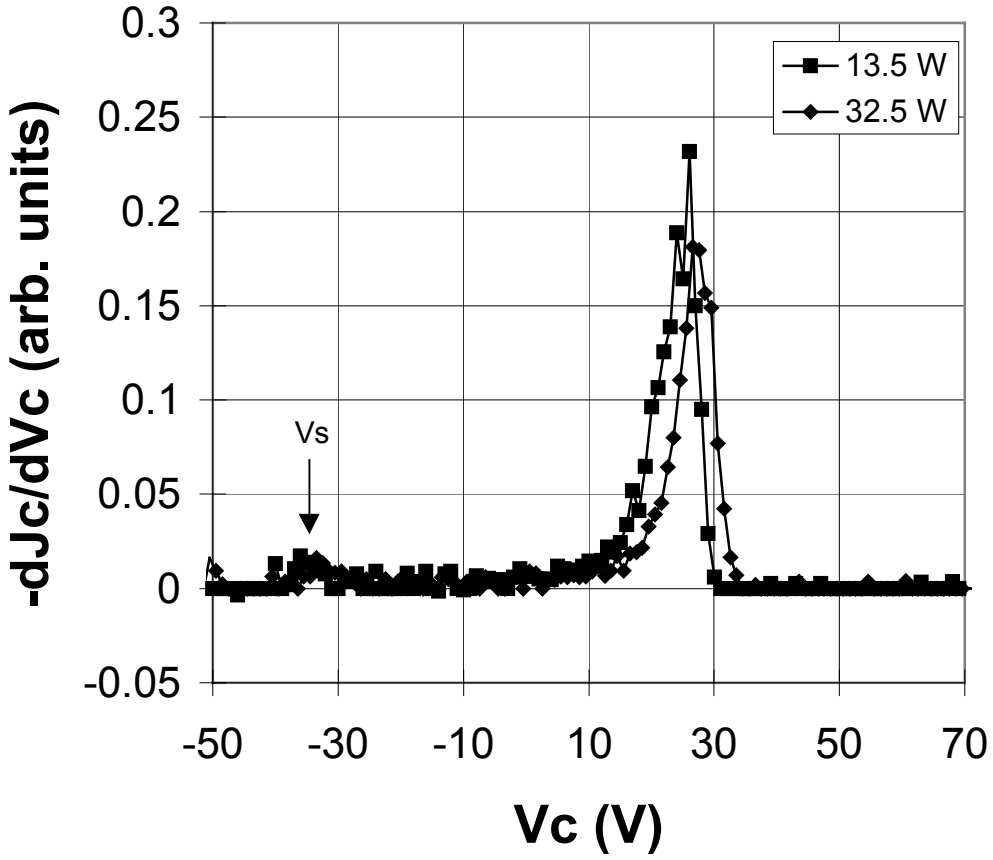

Figure 11. Ion energy distribution with two VHF powers for H_2 plasma at 0.1 Torr.

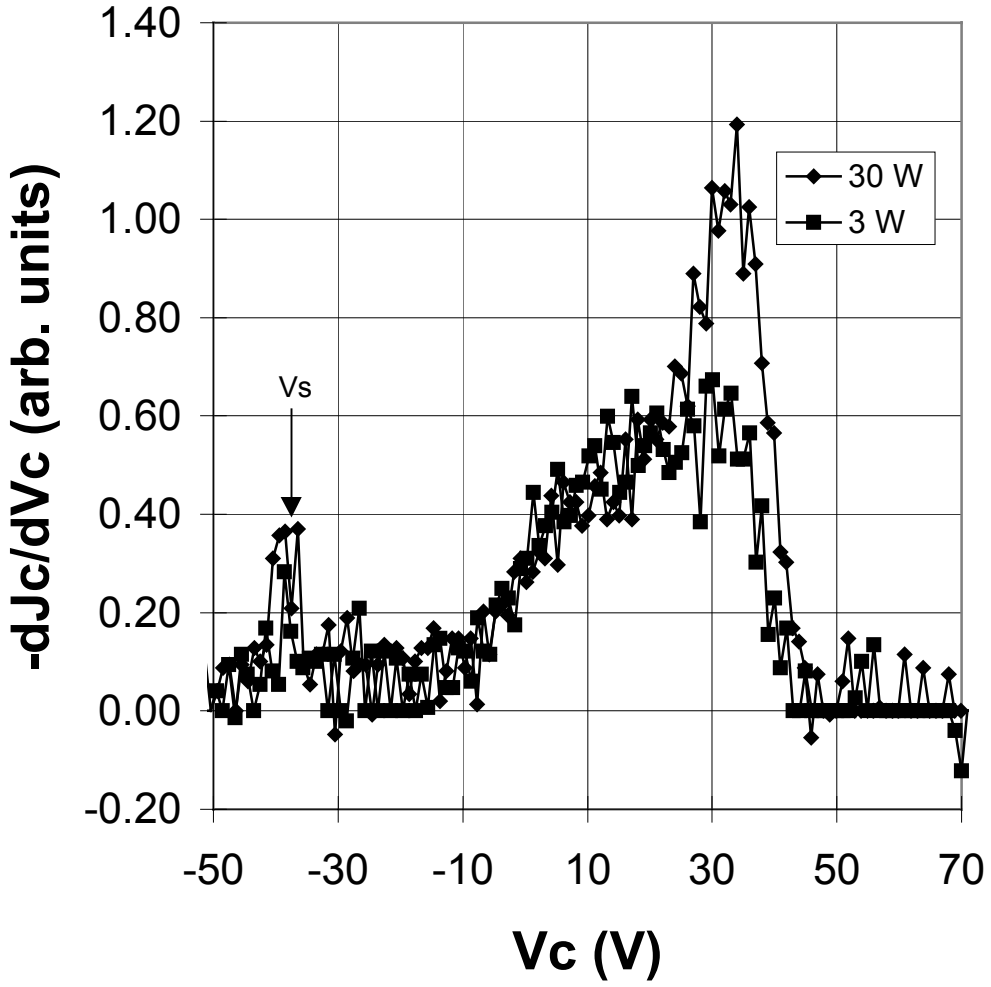

Figure 12. Ion energy distribution with two RF powers for H_2 plasma at 0.1Torr.

bombardment from the plasma itself. Second, at low pressures, the ion bombardment is higher in RF plasma than in MVHF plasma. Third, the positive ion flux is higher in MVHF plasma than in RF plasma.

In order to find out whether the ion bombardment is beneficial for making a-Si alloy solar cells with MVHF, we have performed systematic studies of the effects of pressure and external bias on a-Si alloy solar cells. Table 8 summarizes the characteristics of 2100Å thick a-Si alloy solar cells deposited on stainless steel substrate as a function of deposition pressure of the intrinsic layers. The deposition rate is significantly influenced by the deposition pressure. The cell made at 0.1 Torr is not as good as the cells made at 1.0 Torr or 1.5 Torr although the deposition rate is only 4.4Å/s. This is probably due to the ion bombardment. On the other hand, at pressures greater than 2.0 Torr, the V_{oc} and FF drop that may be attributed to occurrence of polymerization in the plasma.

Table 9 summarizes the performance of a-Si alloy solar cells deposited at 0.1 Torr with different external DC biases. The positive and negative biases slightly reduce and enhance the deposition rate, respectively. The FF of the positively biased cells is better than the one deposited on a floating substrate. The negative bias significantly reduces the FF. Physically, a positive bias reduces the energy and flux of the positive ions and a negative bias accelerates the positive ions toward the substrate. Therefore, we may conclude that ion bombardment is not beneficial for making a-Si alloy solar cells using MVHF with current conditions.

Table 8. Characteristics of a-Si Alloy Solar Cells made at Different Pressures.

Sample VHF	J_{sc} (mA/cm^2)	V_{oc} (V)	FF	FF_b	FF_r	Efficiency (%)		Rate (Å/s)	Thickness (Å)	Pressure (Torr)
						Active	Total			
7666	9.75	0.991	0.698	0.767	0.684	6.74	6.27	4.4	2170	0.1
7689	11.2	0.976	0.702	0.759	0.706	7.66	7.12	14.0	2530	1.0
7664	10.55	0.990	0.719	0.781	0.706	7.41	6.89	8.9	2135	1.5
7687	9.91	0.956	0.701	0.770	0.704	6.23	5.79	6.0	1810	2.0
7694	11.04	0.936	0.646	0.771	0.694	6.67	6.20	3.0	2085	2.5

Table 9. Characteristics of a-Si Alloy Solar Cells made at 0.1 Torr with Different Biases.

Sample VHF	J_{sc} (mA/cm^2)	V_{oc} (V)	FF	FF_b	FFr	Efficiency (%)		Rate (Å/s)	Thickness (Å)	Bias (V)
						Active	Total			
7716	9.67	0.989	0.695	0.759	0.681	6.64	6.18	4.2	2040	-5.6*
7717	9.84	0.998	0.702	0.778	0.689	6.89	6.41	4.1	2000	+30
7718	9.65	0.999	0.714	0.774	0.689	6.88	6.40	4.0	1980	+60
7738	9.74	1.000	0.705	0.767	0.679	6.87	6.39	4.1	2000	+90
7739	9.49	0.997	0.712	0.770	0.700	6.74	6.27	3.9	1930	+120
7740	9.48	1.005	0.721	0.780	0.695	6.87	6.39	3.9	1930	+150
7741	9.08	0.992	0.632	0.711	0.671	5.69	5.29	4.7	2280	-60
7742	8.42	1.005	0.617	0.691	0.635	5.22	4.85	4.9	2410	-120

*Self bias on floating substrate.

The pressure and external bias experiments were also carried out on a-SiGe alloy middle cell. The performance of the middle cell is strongly dependent on pressure. The cells made at low pressure (0.1Torr) show relatively poor performance. The external bias probably has more effect at low pressure than at high pressure. Therefore, we first made a-SiGe alloy middle cells at low pressure with different biases on the stainless steel substrate. The characteristics of these cells are listed in Table 10. The I-V measurements were made under an AM1.5 solar simulator with a 530nm cut-on filter. The negative bias increases V_{oc} and decreases J_{sc} that implies reduced Ge incorporation in the a-SiGe alloy layer. The positive bias has very little effect on the performance of the cell. Since our best a-SiGe alloy cell is made at high pressure, we examined the effect of bias for cells made at high pressure. The results are shown in Table 11. Similar to

Table 10. Characteristics of a-SiGe Alloy Middle Cells Made at Low Pressure with External Bias.

Sample VHF	J_{sc} (mA/cm^2)	V_{oc} (V)	FF	FF_b	FF_r	P_{max} (mW/cm^2)		Thickness (Å)	V_{bias} (V)
						Active	Total		
7763	7.3	0.697	0.579	0.637	0.567	3.0	2.8	1410	-6.2*
7766	7.0	0.699	0.579	0.623	0.578	2.8	2.6	1493	+60
7775	7.2	0.688	0.562	0.593	0.561	2.8	2.6	1484	+120
7767	4.7	0.812	0.625	0.671	0.613	2.4	2.2	1471	-60
7776	6.3	0.762	0.612	0.632	0.606	2.9	2.7	1493	-120

*Self bias on floating substrate.

Table 11. Characteristics of a-SiGe Alloy Middle Cells Made at High Pressure with External Bias.

Sample VHF	J_{sc} (mA/cm^2)	V_{oc} (V)	FF	FF_b	FF_r	P_{max} (mW/cm^2)		Thickness (Å)	V_{bias} (V)
						Active	Total		
7788	8.34	0.751	0.648	0.696	0.659	4.06	3.78	1675	-7.2*
7801	8.71	0.739	0.618	0.679	0.635	3.98	3.70	1630	-6.7*
7802	8.46	0.747	0.640	0.701	0.644	4.04	3.76	1620	+30
7803	8.49	0.739	0.638	0.697	0.645	4.00	3.72	1710	+60
7789	8.48	0.735	0.638	0.686	0.652	3.96	3.68	1665	+120
7804	8.64	0.736	0.625	0.685	0.632	3.97	3.69	1630	-30
7805	8.76	0.736	0.587	0.686	0.592	3.78	3.52	1740	-60
7790	8.39	0.731	0.572	0.690	0.579	3.51	3.26	1715	-120

*Self bias on floating substrate.

the low pressure case, the positive bias does not affect the cell performance, but the negative bias reduces the FF. It should be pointed out that the negatively biased cells are slightly thicker than the unbiased and positively biased cells.

4.2.2. Effect of Hydrogen Dilution on a-Si and a-SiGe Alloy Solar Cells made Near the Formation of Microcrystalline Silicon

H_2 dilution has been found to improve the performance and stability of RF a-Si alloy solar cells. The best a-Si and a-SiGe alloy solar cells were made with a hydrogen dilution level just below the threshold of microcrystalline silicon formation (Yang et al. 1999). The effect of H_2 dilution on the MVHF solar cells may be different for RF. The red FF drops with the increase of H_2 dilution within a certain range. This indicates that high H_2 dilution is not beneficial to making good material and devices in the range investigated. To clarify the different effects of H_2 dilution between RF deposition and MVHF deposition, systematic studies of H_2 dilution on a-Si and a-SiGe alloy solar cells were conducted.

The characteristics of a-Si solar cells made with different SiH_4 flow rates are plotted in Fig. 13. All other deposition parameters were kept the same. These cells were designed to have an intrinsic layer thickness of about 2100Å. It is clear that when the SiH_4 flow is less than 4sccm, all the parameters, J_{sc}, V_{oc} and FF, drop with a decrease of SiH_4 flow rate. This phenomenon is probably related to the formation of microcrystallites. For these experimental conditions, the threshold level of microcrystallization is ~4sccm. The FF under AM1.5 and red light illumination increases with an increase in SiH_4 flow rate above 4sccm. J_{sc} slightly increases and V_{oc} slightly decreases. The cell made with a SiH_4 flow rate of 8sccm exhibits the best overall performance with the other deposition parameters kept the same. In addition, the deposition rate increases with an increase in the SiH_4 flow rate. For a SiH_4 flow rate of 2sccm, the deposition rate was 4.2Å/s, while it was 8.8Å/s for a flow rate of 10sccm.

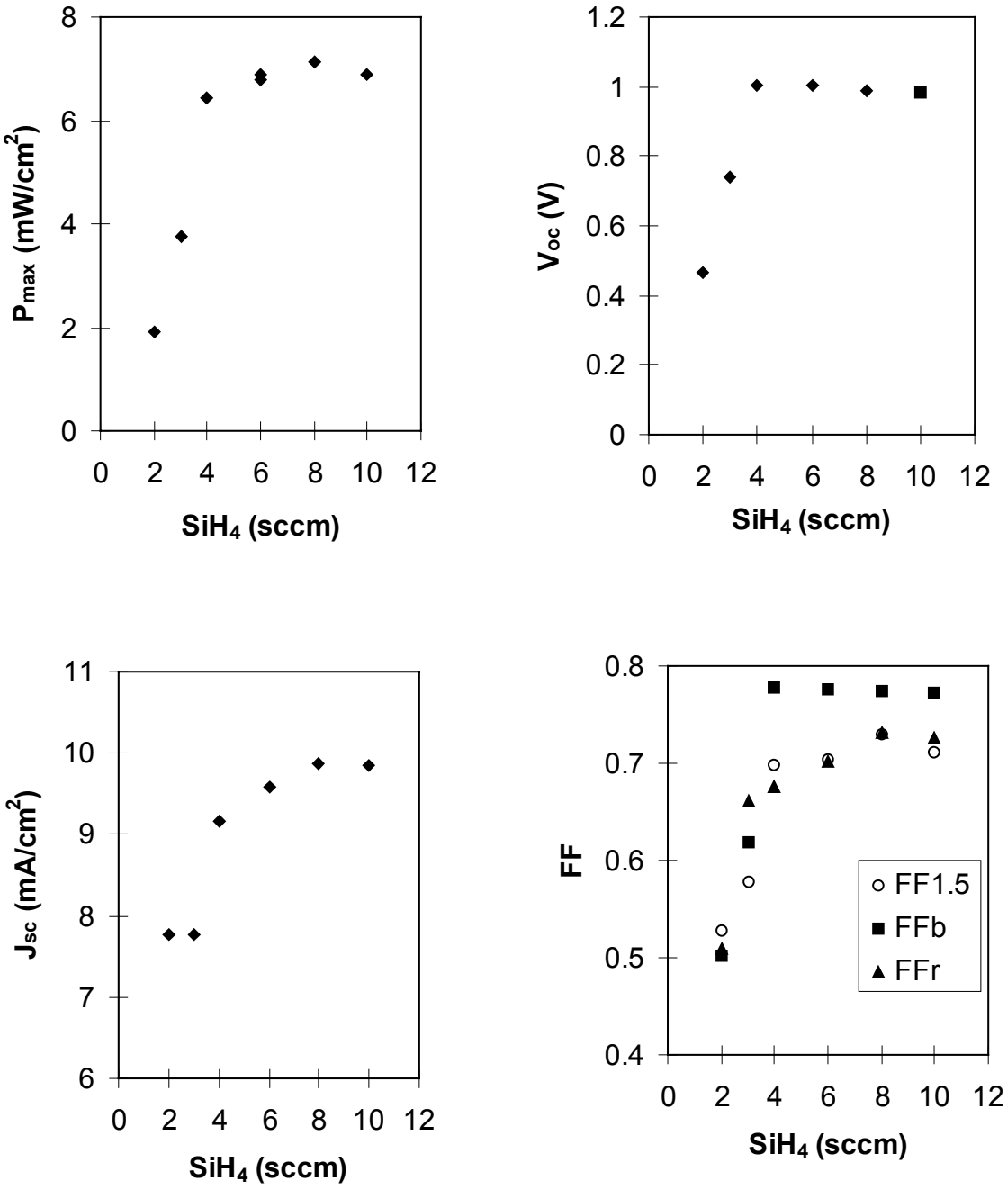

Figure 13. Characteristic parameters for 2100Å thick a-Si alloy solar cells made at different SiH_4 flow rates on stainless steel substrate.

The microcrystalline formation also depends on the cell thickness (Yang et al. 2000). Figure 14 shows the V_{oc} as a function of cell thickness for various hydrogen dilution levels. The different gas flow rates in the figure refer to SiH_4 gas. Higher flow rates imply lower dilution and vice versa. The results show that the V_{oc} decreases with increasing cell thickness. The thickness at which the V_{oc} dramatically drops corresponds to the microcrystalline formation. A high hydrogen dilution level leads to a sharper transition on the thickness scale. By controlling the hydrogen dilution level, we have made a-Si alloy solar cell with V_{oc} greater than 1.02V at a deposition rate as high as 8-9Å/s.

Similar experiments were made on a-SiGe alloy middle cells with a thickness of about 1500Å. The cells were deposited on stainless steel (ss) and on Ag/ZnO back reflector (BR). For this study, we kept the deposition rate at ~6Å/s by changing the VHF power for different flow rates. Figures 15 and 16 show the FF of a-SiGe alloy middle cells on ss and on BR, respectively, as a function of H_2 flow rate. For all cells, the active gas flow rate and other deposition conditions were kept the same. Although the fill factor of the a-SiGe alloy cells on ss is largely independent of the H_2 flow rate as indicated in Fig. 15, the corresponding value on BR decreases with increase of H_2 flow rate for H_2 flow rate greater than 130sccm. Below this value, the fill factor is independent of the H_2 flow rate. The different behavior observed for the cells on ss and BR may be attributed to the texture of the BR. Microcrystallization may occur more easily on textured surfaces than on smooth surfaces. We speculate that the cells made on BR with H_2 flow rate greater than 130sccm contain some microcystallites. The cells on ss do not show the microcrystalline features.

There would not be microcrystalline formation for the above conditions for the RF-PECVD case. It has been reported that the threshold of H_2 dilution for microcrystallization is much lower in VHF deposition than in RF deposition (Platz et al. 1998). From the current experiments it is clear that the H_2 dilution level has to be reduced for fabricating a-Si and a-SiGe alloy solar cells using MVHF. Since the threshold of H_2 dilution depends on other deposition conditions such as pressure, VHF power and substrate temperature, the appropriate H_2 dilution level has to be determined experimentally for a specific deposition regime.

4.2.3. Study of Amorphous Silicon Alloy Solar Cells Deposited using Fluorine Containing Gases

It is well known that hydrogen dilution can significantly improve the quality and stability of amorphous silicon alloy materials and devices. The best a-Si alloy solar cells are made at H_2 dilution levels slightly lower than the formation of microcrystallites. Although the role of H_2 dilution to improve a-Si alloy solar cells is not very clear, it is believed that the etching effect of hydrogen in the plasma improves the quality and stability of a-Si alloy materials. Experimentally, it was found that the intermediate range order was improved by high H_2 dilution.

We have used MVHF glow discharge technique to deposit a-Si alloy materials for solar cells at high deposition rates (Yang et al. 1998, Yan et al. 1999). However, the high-rate MVHF solar cells are not as good as the low-rate RF solar cells. For a-SiGe alloy cells, the difference between the performance of the RF low-rate solar cells and the VHF high-rate solar cells is greater. It is well known that fluorine also has a strong etching effect. We have investigated the effect of fluorine in the plasma on the performance of a-Si and a-SiGe alloy solar cells for the MVHF high-rate deposition case.

Amorphous silicon alloy solar cells were deposited on bare stainless steel substrates using MVHF system at high deposition rates (6-13Å/s) and conventional RF glow discharge system at low deposition rates (1-2Å/s). The thickness of the intrinsic layer was ~2200-2600Å. The baseline cells were made with H_2 and SiH_4 (or Si_2H_6) mixture at different H_2 dilution ratios. SiF_4 or HF was introduced into the plasma as fluorine sources. The deposition rate was adjusted by changing the RF or VHF power.

Figure 17 plots the J-V characteristics of a-Si alloy solar cells made with RF at low rates. Gas flow ratio is defined as $HF/(Si_2H_6+HF)$ or $SiF_4/(Si_2H_6+SiF_4)$. It is clear that the fill factor decreases with the increase

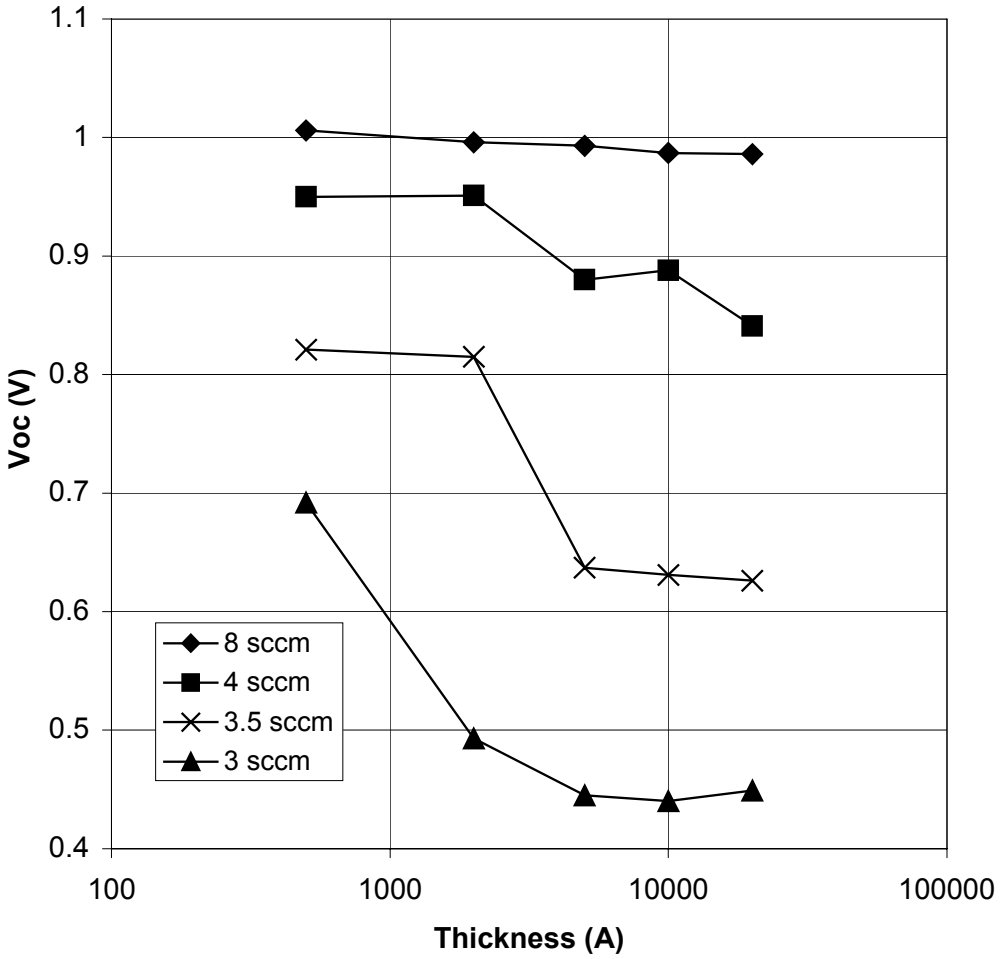

Figure 14. V_{oc} as a function of thickness of intrinsic layer for a-Si alloy solar cells made using MVHF at deposition rate ~8-9Å/s. The four gas flow rates refer to SiH_4 gas.

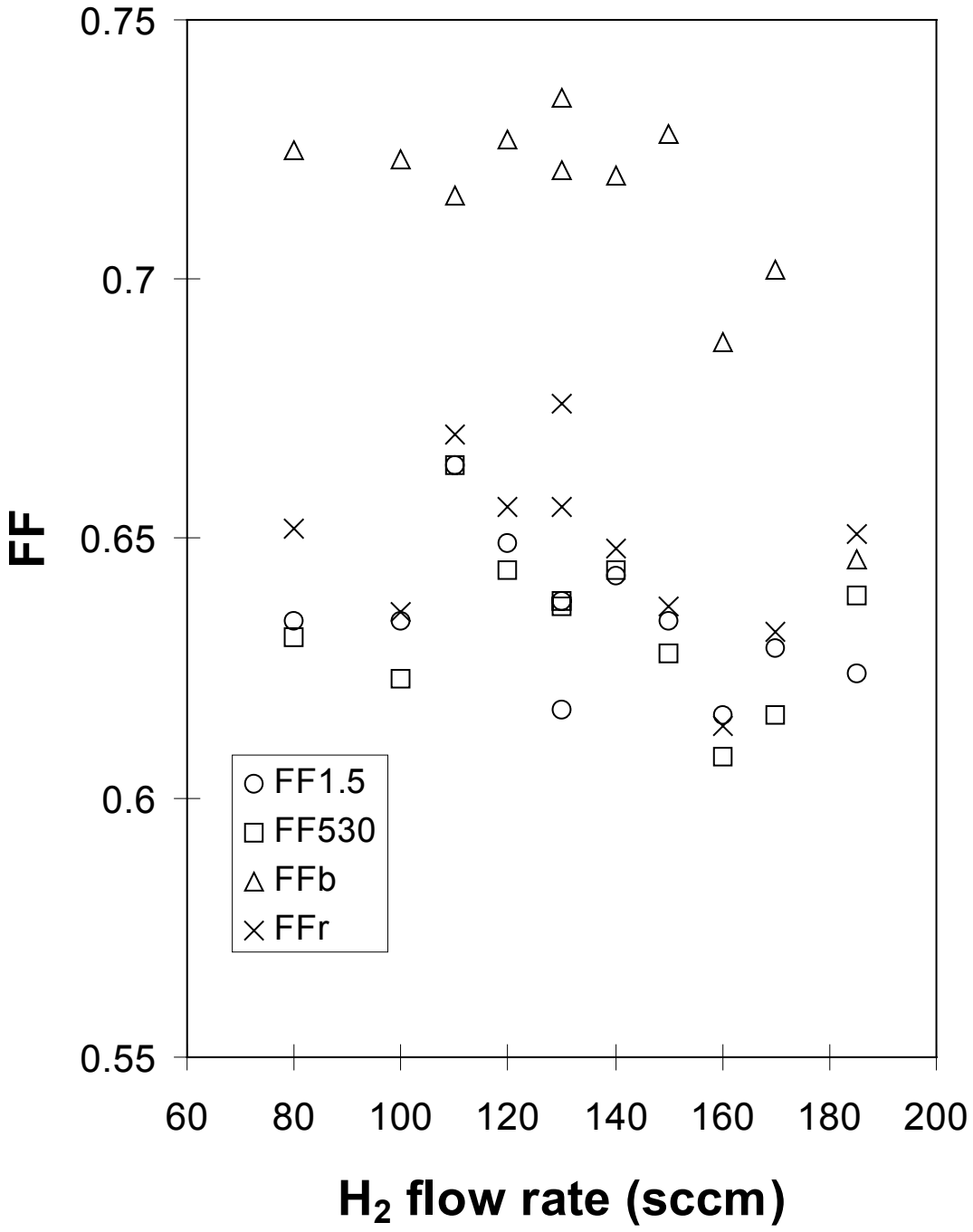

Figure 15. Fill factor of a-SiGe alloy solar cells on stainless steel as a function of H_2 flow rate. The cells were made at ~6Å/s.

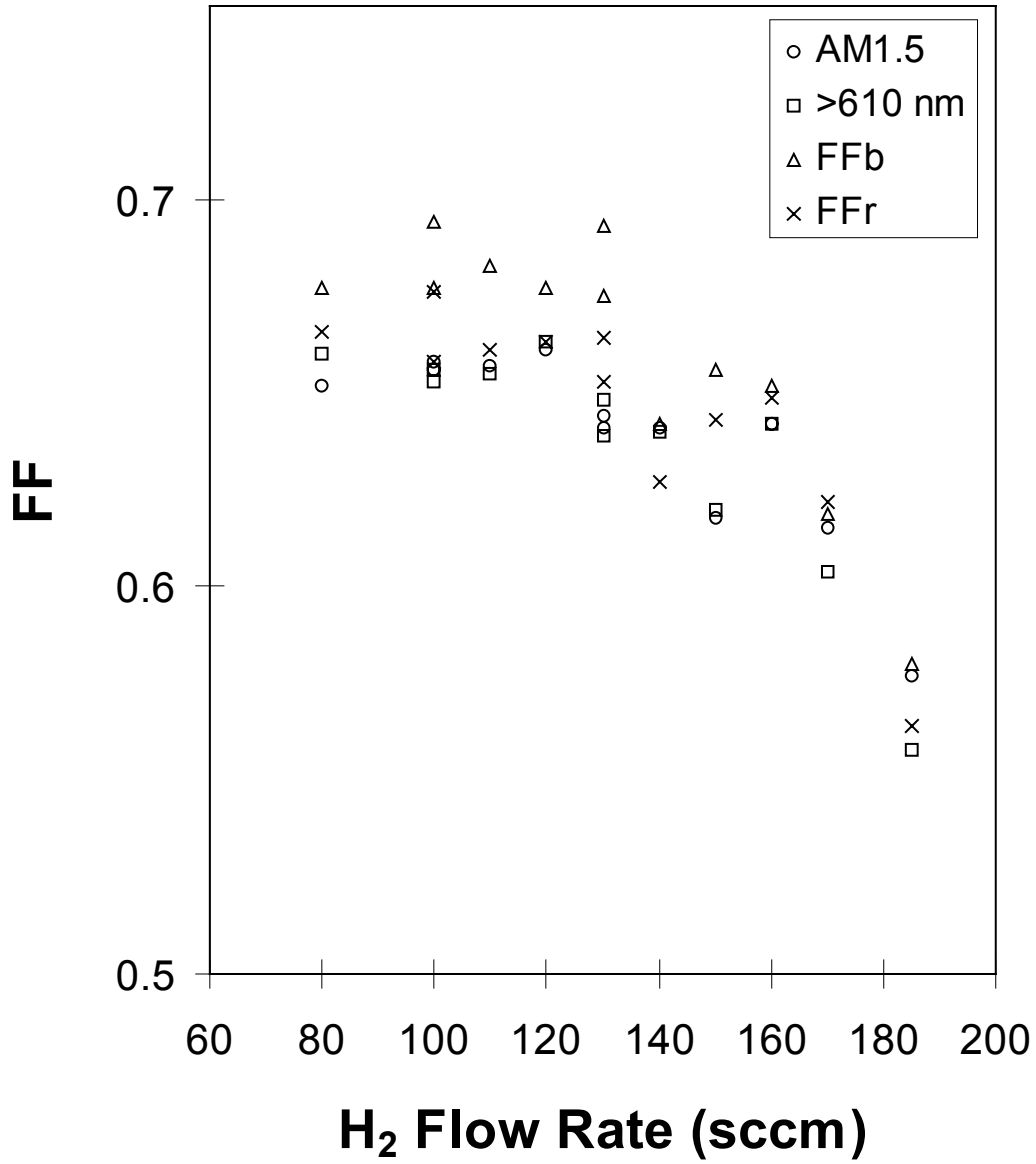

Figure 16. Fill factors of a-SiGe alloy solar cells on BR as a function of H_2 flow rate. The deposition conditions were the same as in Fig. 15.

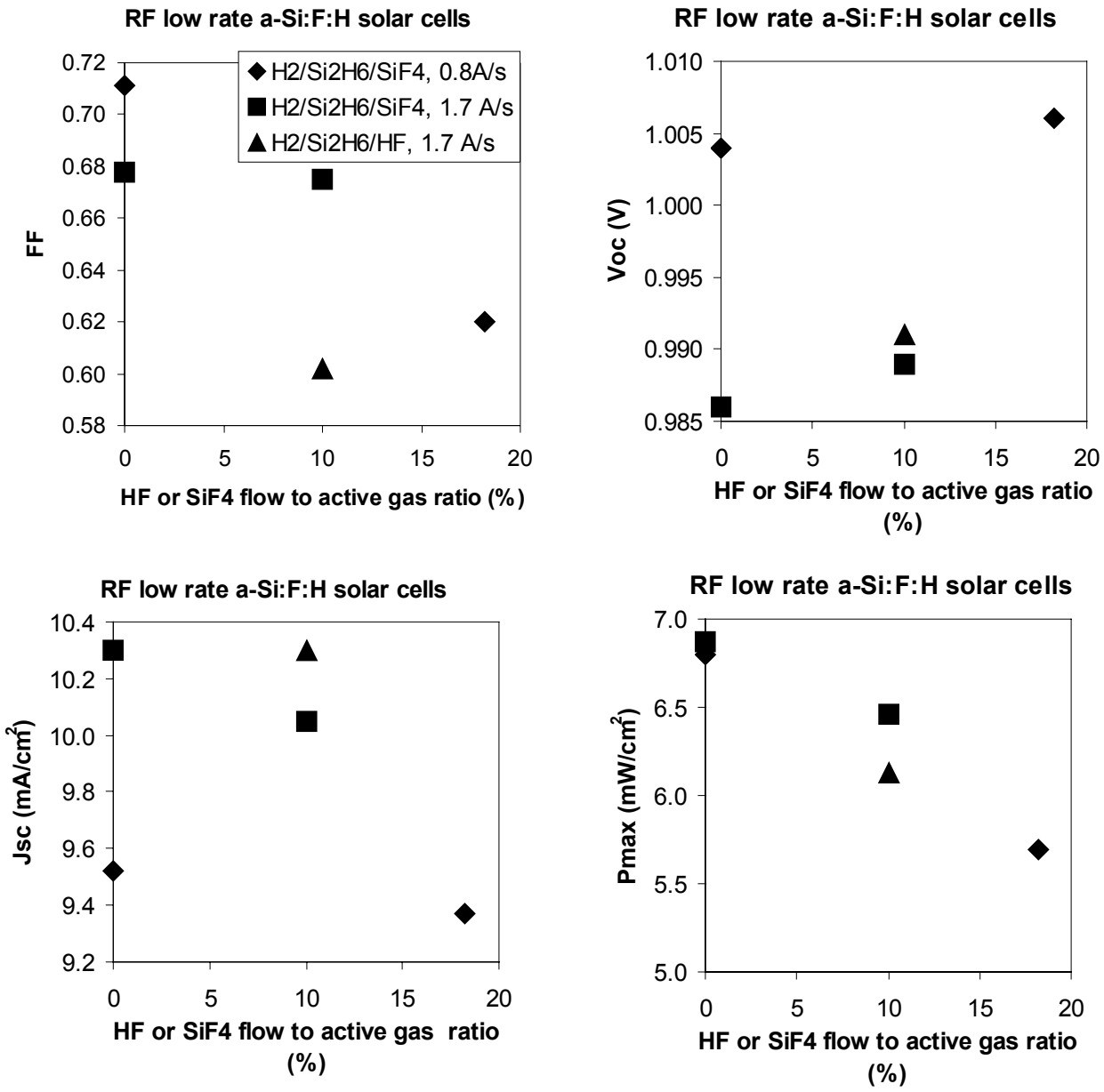

Figure 17. Characteristics of a-Si:F:H solar cells as a function of gas flow ratio HF/(Si_2H_6+HF) or SiF_4/(Si_2H_4+SiF_4). The cells were made with RF at low deposition rates.

of fluorine containing gas flow ratios. This is the main factor that leads to the overall poorer performance of the cells. Use of HF instead of SiF_4 leads to worse cell performance.

Figure 18 plots the J-V characteristics of a-Si alloy solar cells made with MVHF at deposition rate ~8-9Å/s. It is interesting to note that the FF of the cells made with SiF_4 is relatively insensitive to the SiF_4 flow ratios of up to 20%. The FF drops slightly for SiF_4 flows greater than 20%. However, the performance of the cells made with HF decreases dramatically with the increase of HF flow. Again, HF seems to have a greater effect than SiF_4.

Introduction of fluorine-containing gases into the plasma leads to lower deposition rate. In order to keep the same deposition rate we had to increase the VHF power. This result indicates that fluorine-containing gases have extra etching effect. The phenomenon that the cell performance starts to deteriorate when SiF_4 flow is more than 20% may be due to etching by both hydrogen and fluorine. Therefore, if we reduce the H_2 dilution and add a certain amount of SiF_4, we may find a regime for making good solar cells with SiF_4. For this purpose, we made two sets of a-Si alloy solar cells with different SiF_4 flow ratios at reduced H_2 flow rates.

Tables 12 and 13 summarize the solar cell performance made with the H_2 dilution ratios reduced by factors of two and four, respectively. The results show that up to 33% of SiF_4 in the gas phase, the cell performance is not sensitive to the SiF_4 flow ratio within experimental error. At 50% of SiF_4, the cell performance is poorer. The reduction of the performance at 50% of SiF_4 is less for the H_2 dilution reduced by a factor of four than by a factor of two.

The comparison of the stability of a-Si alloy solar cells made with 20% of SiF_4 and without SiF_4 is listed in Table 14. The cells were light-soaked under a white light intensity of 100mW/cm^2 at 50^{0}C for 1350 hours. The result shows that the solar cell made with 20% of SiF_4 in the gas phase has a stability similar to the cell made without SiF_4.

Table 12. J-V Characteristics of a-Si Alloy Solar Cells made with Different SiF_4 Gas Flow Rates. The H_2 Flow Rate was Reduced by a Factor of Two from the Baseline. The Deposition Rate is ~8-9Å/s.

Run #	P_{max} (mW/cm^2)	J_{sc} (mA/cm^2)	V_{oc} (V)	FF	Comments
MVHF8422	6.16	9.58	0.961	0.669	No SiF_4
MVHF8423	6.24	9.93	0.959	0.655	20% SiF_4
MVHF8426	6.39	10.04	0.962	0.662	33% SiF_4
MVHF8427	5.77	9.75	0.942	0.628	50% SiF_4

Table 13. J-V Characteristics of a-Si Alloy Solar Cells made with Different SiF_4 Gas Flow Rates. The H_2 Flow Rate was Reduced by a Factor of Four from the Baseline. The Deposition Rate is ~8-9Å/s.

Run #	P_{max} (mW/cm^2)	J_{sc} (mA/cm^2)	V_{oc} (V)	FF	Comments
MVHF8449	7.01	11.45	0.955	0.641	No SiF_4
MVHF8447	6.76	11.03	0.957	0.640	20% SiF_4
MVHF8446	6.81	10.94	0.951	0.655	33% SiF_4
MVHF8443	6.41	10.49	0.944	0.647	50% SiF_4

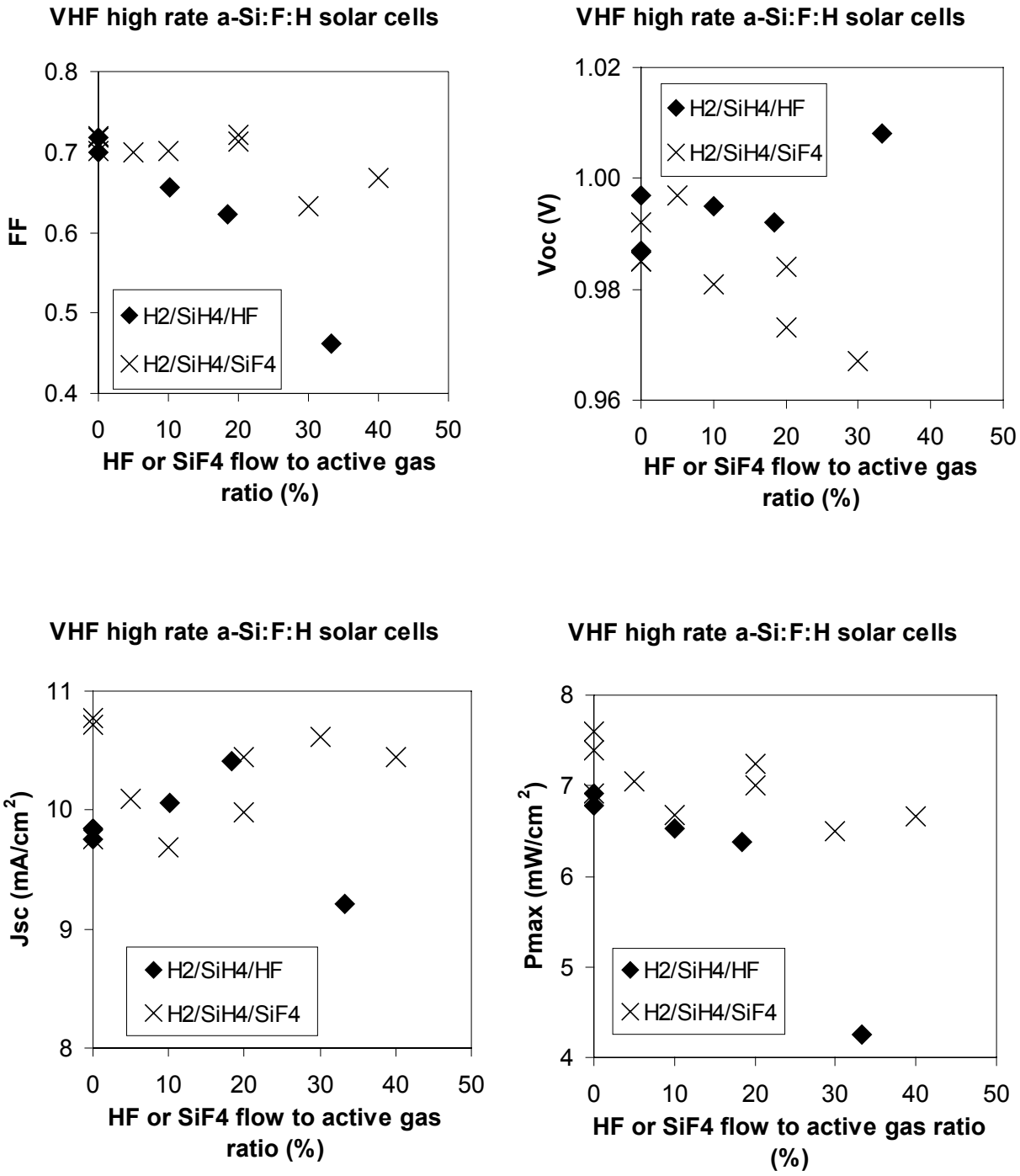

Figure 18. Characteristics of a-Si:F:H solar cells as a function of gas flow ratio HF/(SiH_4+HF) or SiF_4/(SiH_4+SiF_4). The cells were made with MVHF at deposition rate ~8-9Å/s. The cell thickness is ~2200Å.

Table 14. Comparison of Stability of a-Si Alloy Solar Cells made with 20% of SiF_4 and without SiF_4 in the Gas Phase. The Cells were made using MVHF at ~8-9Å/s.

Run#	State	P_{max} (mW/cm^2)	J_{sc} (mA/cm^2)	V_{oc} (V)	FF	Degradation (%)	Comment
MVHF8354	Initial	7.49	10.77	0.992	0.701		No SiF_4
	Stable	5.91	10.08	0.950	0.617	21.1	
MVHF8352	Initial	7.24	10.44	0.973	0.713		20% SiF_4
	Stable	5.70	9.62	0.934	0.635	21.3	

We have also studied the effect of adding fluorine-containing gases to the plasma on the a-SiGe alloy solar cells. As in the case of the a-Si alloy cell, there is no significant effect at low HF or SiF_4 flow ratio, but the cell performance becomes poorer when fluorine containing gas flow ratio is high. The stability of the cells made with fluorine containing gases is not better than that without fluorine.

In conclusion, using HF with either RF at low rates or MVHF at high rates results in poorer solar cell performance. A similar result was obtained for using SiF_4 with RF at low rates. However, using MVHF at high rates, the cell performance was not sensitive to SiF_4 flow ratios of up to 20% for high H_2 dilution. When the H_2 dilution ratio was reduced, the SiF_4 flow ratio can go up to more than 33% without deteriorating the cell performance. Solar cells made with 20% of SiF_4 or without SiF_4 have similar stability.

4.2.4. a-Si and a-SiGe Alloy Solar Cells made with Amplitude-Modulated MVHF Glow Discharge

It has been reported that for the VHF technique, the deposition rate of a-Si alloy materials can be increased by modulating the amplitude of the excitation source (Biebericher et al. 2000). The deposition rate was shown to be three times higher with a modulation frequency of 100kHz than that with a continuous-wave (CW) plasma. The amplitude modulation is accomplished by superimposing a modulation square-wave pulse on the VHF excitation and then varying the modulation frequency. The higher deposition rate is believed to be due to the high-energy electrons present during the onset of plasma at each cycle of modulation. We have investigated the amplitude-modulated MVHF glow discharge process to explore the possibility of improving solar cell performance.

The MVHF system used in this study is the same as described in the above section. The VHF frequency is 75 MHz. The VHF signal is modulated with a square wave. The duty cycle was fixed at 50% and the modulation frequency was changed from 50Hz to 100kHz. In order to keep the same average power as the CW condition, the input power for the VHF-on duration was twice that of the CW VHF power. a-Si alloy and a-SiGe alloy single-junction solar cells were deposited on stainless steel substrate with various modulation frequencies.

Figure 19 shows the deposition rate of a-Si alloy as a function of modulation frequency. The deposition rate initially increases with increasing modulation frequency up to 100Hz and then decreases with further increase of modulation frequency. At modulation frequencies greater than 10kHz, the deposition rate is lower than that for the CW condition. Figure 20 shows the dependence of the self-bias on the modulation frequency. The qualitative behavior of the self-bias as a function of modulation frequency is similar to the corresponding behavior of the deposition rate. The value of the self-bias is proportional to the power coupled into the plasma. Therefore, we believe that higher modulation frequency leads to inefficient coupling of the VHF power to the plasma. If the power coupled to the plasma can be kept the same at the higher modulation frequencies, the deposition rate would be higher as shown by Biebericher et al. (2000).

The J-V results of a-Si alloy solar cells, made with intrinsic layer thickness ~2600Å, for various modulation frequencies are summarized in Table 15. The cell performance is poor at low modulation frequencies of 100Hz and 500Hz. At higher modulation frequencies (1-50kHz), the results improve. However, the best

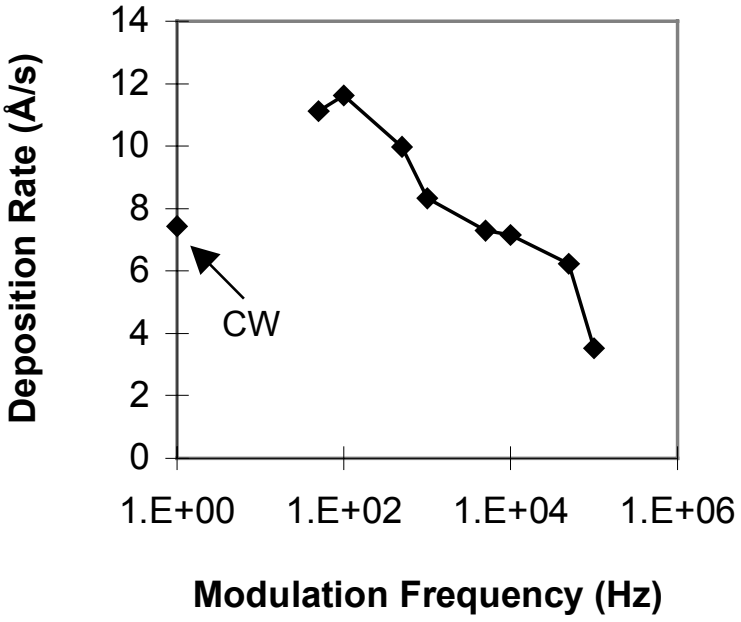

Figure 19. Deposition rate vs. modulation frequency for a-Si alloy materials.

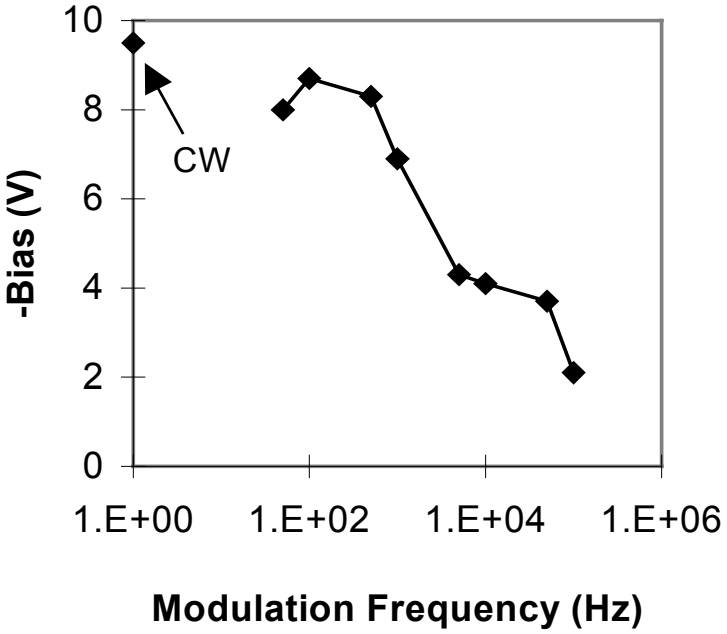

Figure 20. Self-bias vs. modulation frequency for a-Si alloy deposition.

Table 15. Initial Active-Area J-V Characteristics of a-Si Alloy Top Cells made with Various Modulation Frequencies (f). Other Deposition Parameters are the same except Deposition Time that was Adjusted to get a Similar Intrinsic Layer Thickness.

Sample No.	P_{max} (mW/cm^2)	J_{sc} (mA/cm^2)	V_{oc} (V)	FF	f (Hz)
10613	8.09	11.5	0.988	0.712	0
10614	3.00	7.40	0.799	0.502	100
10615	5.20	10.4	0.908	0.549	500
10616	7.08	10.83	0.954	0.684	1000
10617	7.67	11.24	0.979	0.697	5000
10618	8.01	11.53	0.987	0.704	50000

cell made with modulated plasma is not better than that made with the CW plasma. Qualitatively, the results are similar for a-SiGe alloy solar cells (flat bandgap) as shown in Table 16. At a modulation frequency of 500Hz, the cell performance is poor. At higher frequencies, 5kHz and 50kHz, the results are similar to the reference CW cell.

In summary, we have been unable to improve cell performance by amplitude modulation of MVHF glow discharge. The cell optimization process is complicated and it is difficult to improve upon the well-optimized reference CW cells. It is conceivable that in a different deposition regime such as different pressure, the cell results using MVHF modulation might be superior.

Table 16. Initial Active-Area J-V Characteristics of a-SiGe Alloy Middle Cells made with Various Modulation Frequencies (f). The Measurements were taken under AM1.5 Solar Simulator with a 530nm Cut-On Filter.

Sample No	P_{max} (mW/cm^2)	J_{sc} (mA/cm^2)	V_{oc} (V)	FF	f (Hz)
10649	4.06	9.25	0.715	0.612	0
10653	3.29	7.47	0.724	0.609	500
10561	3.94	8.45	0.735	0.633	5000
10652	4.10	9.15	0.735	0.610	50000

4.3. Bandgap Engineering of a-Si and a-SiGe Alloy Solar Cells

High efficiency solar cells require precise control of the interface layers in the device. Also, an appropriate bandgap profile is necessary for a-SiGe devices. In this section, we present the results of solar cells with different interface and bandgap profiles.

4.3.1. n/i and i/p Interfaces in a-Si Alloy Solar Cells

In general, the properties of the n/i and i/p interfaces are important for achieving high efficiency solar cells. By inserting optimized buffer layers at the interfaces, the device performance can be improved (Banerjee et al. 1995). Interface buffer layers have been incorporated in the 8-9Å/s MVHF a-Si alloy solar cells. Table 17 summarizes the J-V characteristics of two pairs of a-Si alloy top cells prepared at 8-9Å/s with and without the interface buffer layers. The intrinsic layers of #8913 and #8915 were made at a different hydrogen dilution level than those of #8914 and #8916. The table shows that the blue, red and AM1.5 fill factors are all improved by the buffer layers. In addition, short-circuit current density J_{sc} is also increased. The average gain from the buffer layers is ~7.5%.

Table 17. Initial Active-Area J-V Characteristics of a-Si Alloy Top Cells made at 8-9Å/s Using MVHF with and without Buffer Layers.

Run #	P_{max} (mW/cm^2)	J_{sc} (mA/cm^2)	V_{oc} (V)	$FF_{1.5}$	FF_b	FF_r	Comment
8913	5.86	8.02	1.006	0.726	0.779	0.700	Without buffers
8915	6.47	8.77	1.005	0.738	0.781	0.722	With buffers
8914	6.13	8.4	0.998	0.731	0.788	0.711	Without buffers
8916	6.45	8.8	0.993	0.738	0.801	0.733	With buffers

a-Si alloy solar cells fabricated using MVHF excitation have been improved by the incorporation of appropriate interface buffer layers and by optimizing other deposition parameters. Figures 21 and 22 show the J-V characteristics and quantum efficiency, respectively, of the best MVHF a-Si alloy top cell on stainless steel substrate made to date. The deposition rate of the intrinsic layer is ~6Å/s. The cell has an initial active-area efficiency of 6.96%, which is better than the old record and is similar to the best RF low-rate cell as shown in Table 18. Also, the performance of a-Si alloy cells on AgZnO back reflector has been improved. An initial efficiency of 10.2% has been achieved for a device made at 8.7Å/s.

Table 18. New and Old Best Initial Active-Area Results of MVHF Top Cell made on Stainless Steel Substrate at ~6Å/s. The Results of the Best RF Low-Rate (~1Å/s) Top Cell is also shown.

Sample	P_{max} (mW/cm^2)	J_{sc} (mA/cm^2)	V_{oc} (V)	FF
MVHF NEW RECORD	6.96	9.05	1.016	0.757
MVHF OLD RECORD	6.61	8.84	1.002	0.746
RF 1 Å/s RECORD	7.15	9.03	1.024	0.773

4.3.2. n/i and i/p Interfaces in a-SiGe Alloy Middle Cells

Similar studies of n/i and i/p interface layers in a-SiGe alloy middle cells have been carried out. Table 19 gives an example of the effect of n/i and i/p buffer layers on the cell performance. Here, a-SiGe alloy middle cells were deposited using MVHF at 4-6Å/s on specular stainless steel substrate. The J-V characteristics were measured under an AM1.5 solar simulator with a 530nm cut-on filter. Inserting the buffer layers significantly improves all the parameters, especially FF and J_{sc}. The gain from the buffer layers is ~19.6%, which is greater than that of a-Si alloy top cells. This result indicates that the collection loss at the interfaces is large without the buffer layers. The bandgap discontinuity between the doped layers and intrinsic the a-SiGe alloy layer may result in defect states at the interface which enhances the recombination at the interfaces. The buffer layers probably passivate these defects. In addition, the buffer layers may prevent the back diffusion of photo-generated carriers near the doped layers.

The buffer layer in the above a-SiGe alloy solar cells is a thin layer of a-Si alloy. The discontinuity in bandgap between the a-Si buffer layer and the intrinsic a-SiGe layer may cause interface defects thereby

Table 19. J-V Characteristics of a-SiGe Alloy Middle Cells made using MVHF at 4-6Å/s with and without Buffer Layers. #8966 and #8973 have Different Buffer Layers.

Run #	P_{max} (mW/cm^2)	J_{sc} (mA/cm^2)	V_{oc} (V)	$FF_{1.5}$	FF_b	FF_r	Comment
8967	3.26	7.33	0.742	0.600	0.702	0.607	Without buffers
8966	3.88	8.26	0.756	0.622	0.702	0.652	With buffers
8973	3.90	8.11	0.752	0.639	0.705	0.664	With buffers

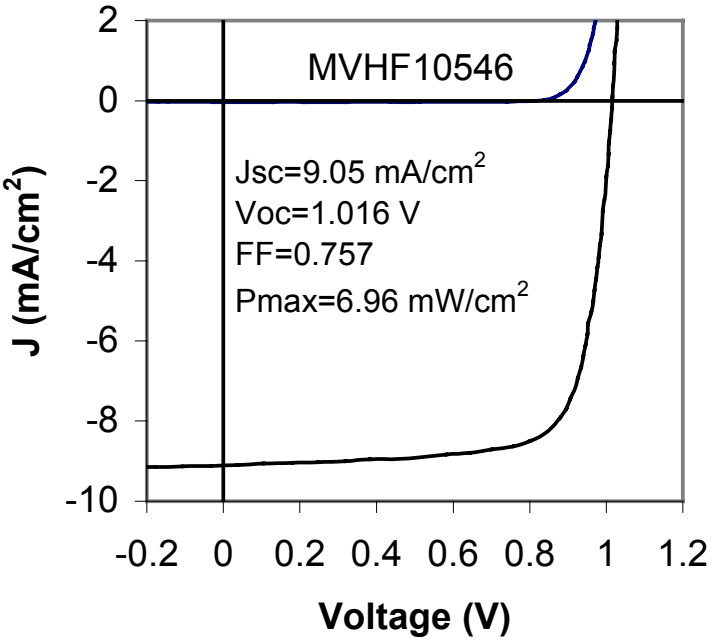

Figure 21. Initial active-area J-V characteristics of the best a-Si alloy top cell made with MVHF at ~6Å/s.

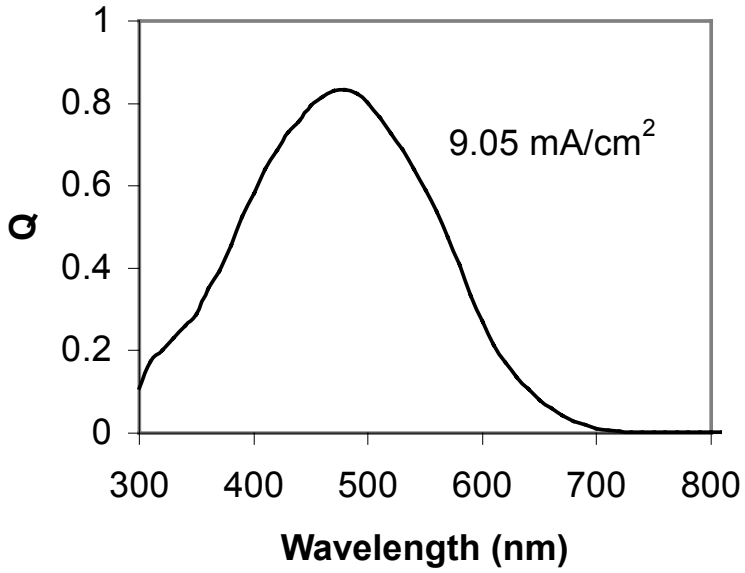

Figure 22. Initial active-area quantum efficiency of the best a-Si alloy top cell made with MVHF at ~6Å/s.

having a deleterious effect on cell performance. By ramping GeH_4 and Si_2H_6 flows, we have made bandgap-profiled buffer layers that have narrower bandgap near the a-SiGe intrinsic layer and wider gap near the doped layer. Table 20 shows the comparison of the a-SiGe alloy middle cell with standard a-Si alloy buffer layers (STD) and bandgap profiled buffer layers (PRF). A 3% gain has been realized in the long-wavelength response that manifests itself in an improved FF.

Table 20. Initial J-V characteristics of a-SiGe Alloy Middle Cells made with MVHF at 6Å/s with Standard and Profiled Buffer Layers.

Sample #	Light	P_{max} (mW/cm^2)	J_{sc} (mA/cm^2)	V_{oc} (V)	FF	FF_b	FF_r	Buffer
9766	AM1.5	6.66	14.42	0.762	0.606	0.709	0.643	STD
	>530 nm	4.04	8.92	0.741	0.611			
9773	AM1.5	6.86	14.35	0.762	0.627	0.706	0.658	PRF
	>530 nm	4.15	8.85	0.741	0.633			

4.3.3. Bandgap Profiling of a-SiGe Alloy Solar Cells

We have reported (Yan et al. 1999) that the difference in the performance of high rate MVHF solar cell and low rate RF cell increases with increasing Ge concentration in the film. There are two factors that may be responsible for the difference. First, the high-rate MVHF a-SiGe alloy materials are not as good as the low rate RF material. Second, there is an engineering difficulty for MVHF a-SiGe solar cells, namely, the bandgap profiling. It has been shown that a proper bandgap profiling can improve the cell performance significantly. In order to determine the limiting factor, we made comparison studies of a-SiGe alloy middle and bottom cells deposited using RF at low rate and MVHF at high rate.

Table 21 lists the J-V characteristics of the middle and bottom a-SiGe alloy cells made with and without bandgap profiling using RF at low rate and MVHF at high rate. Both the RF low-rate cells and the MVHF high rate cells were made in the same reactor. The middle cells were made on stainless steel substrate and measured under an AM1.5 solar simulator with a 530nm cut-on filter. The bottom cells were made on Ag/ZnO back reflector substrate and measured under an AM1.5 solar simulator with a 630nm cut-on filter. A gain ~10% in P_{max} was obtained by using bandgap profiling for the RF low-rate cells, but the gain is marginal (2.7%) for the MVHF cells. The difference between the flat gap low-rate RF cell and the flat gap high-rate MVHF cell is not very large. Indeed, from the P_{max} point of view, the MVHF middle cell is not worse than the RF flat bandgap middle cell. The relative insensitivity of bandgap profiling on cell performance for MVHF high-rate cells may be attributed to the fact that the deposition time is too short for the ratio of silicon to germanium and hence the bandgap to track the change in gas flow rate. Therefore, in order to get improvement in cell performance by bandgap profiling, further optimization for the gas flow rate was required.

Table 21. Comparison of Profiled and Flat Bandgap a-SiGe Alloy Middle Cells and Bottom Cells made with RF at ~1Å/s and MVHF at ~4-6Å/s.

Structure	Run #	P_{max} (mW/cm^2)	J_{sc} (mA/cm^2)	V_{oc} (V)	FF	Comment
RF	8155	4.04	9.78	0.736	0.561	Flat
Middle Cell	8188	4.55	9.61	0.727	0.668	Graded
RF	9209	3.86	10.61	0.628	0.580	Flat
Bottom Cell	9206	4.22	10.00	0.642	0.657	Graded
MVHF	7797	4.07	7.90	0.767	0.671	Flat
Middle Cell	7798	4.18	8.35	0.737	0.679	Graded
MVHF Bottom	7652	3.65	9.24	0.643	0.615	Flat
Cell	7653	3.75	9.67	0.641	0.605	Graded

In order to obtain a proper bandgap profile, we have optimized the gas flow ramping rate and achieved a gain of 8% which is significantly larger than the results of Table 21. Table 22 summarizes the J-V characteristics of the new set of middle cells with different bandgap profiles. Sample 9773 is the baseline cell with a flat bandgap (Flat). For sample 9774, GeH_4 and SiH_4 flow rates were changed in three steps (Step) with higher GeH_4 flow in the region near the p layer and lower flow in the region near the n layer. Sample 9775 had a continuous ramping (Cont) with the same average rate as 9774. It is found that a proper profile of bandgap increases the J_{sc} and FF. The gain in FF is mainly due to the improvement in the long wavelength region (FF_r). On the other hand, a large ramping (Over) decreases the fill factor for short wavelength (FF_b) and leads to a poorer overall performance (sample 9778). Thus, the performance of MVHF high-rate a-SiGe alloy middle cell has been improved by optimizing the bandgap profile. Sample 9775 is the best MVHF high-rate middle cell made to date. Figures. 23 and 24 show the J-V characteristics and quantum efficiency for this sample.

Table 22. Initial Active-Area J-V Characteristics of a-SiGe Alloy Middle Cells made with MVHF at 6Å/s with Different Bandgap Profiling.

Sample #	Light	P_{max} (mW/cm^2)	J_{sc} (mA/cm^2)	V_{oc} (V)	FF	FF_b	FF_r	Profile
9773	AM1.5	6.86	14.35	0.762	0.627	0.706	0.658	Flat
	>530nm	4.15	8.85	0.741	0.633			
9774	AM1.5	6.80	14.53	0.745	0.628	0.702	0.678	Step
	>530nm	4.34	9.07	0.730	0.655			
9775	AM1.5	6.93	14.57	0.755	0.630	0.702	0.666	Cont.
	>530nm	**4.47**	**9.09**	**0.742**	**0.662**			
9778	AM1.5	5.69	13.54	0.731	0.575	0.621	0.675	Over
	>530nm	3.84	8.51	0.719	0.628			

4.4. Optimized MVHF a-Si and a-SiGe Alloy Multijunction Cells

Using the optimized a-Si alloy top cell and thick a-Si alloy bottom cell, we have made same bandgap a-Si/a-Si alloy double-junction cells on Ag/ZnO back reflector. The best same gap cell exhibits an initial efficiency of 10.4%. Figures 25 and 26 show the J-V characteristics and quantum efficiency of the double-junction cell.

a-Si/a-SiGe alloy dual-bandgap double-junction structures on Ag/ZnO back reflector have also been fabricated. Cell optimization consists of proper current matching between the component cells. An example of the effect of current matching is shown in Table 23. The bottom cell in all case is an MVHF a-SiGe alloy material deposited at 6Å/s. The top cell is an MVHF a-Si alloy material deposited at 8Å/s of three different thicknesses. Device #8705 has the thinnest top cell and possesses the best FF. The thickest top cell case #8706 has the worst FF. The cell with highest efficiency, #8704, has the intermediate top cell thickness. Further optimization has led to an efficiency of 11.4%. The J-V characteristics and Q curves of the best device #9998 are shown in Figs. 27 and 28, respectively.

Compared with low-rate RF cells made using our LINE system, the MVHF high-rate double-junction cells suffer from low current of the a-SiGe alloy bottom cell. Low current for high-rate a-SiGe alloy solar cell appears to be an attribute of the high-rate MVHF process.

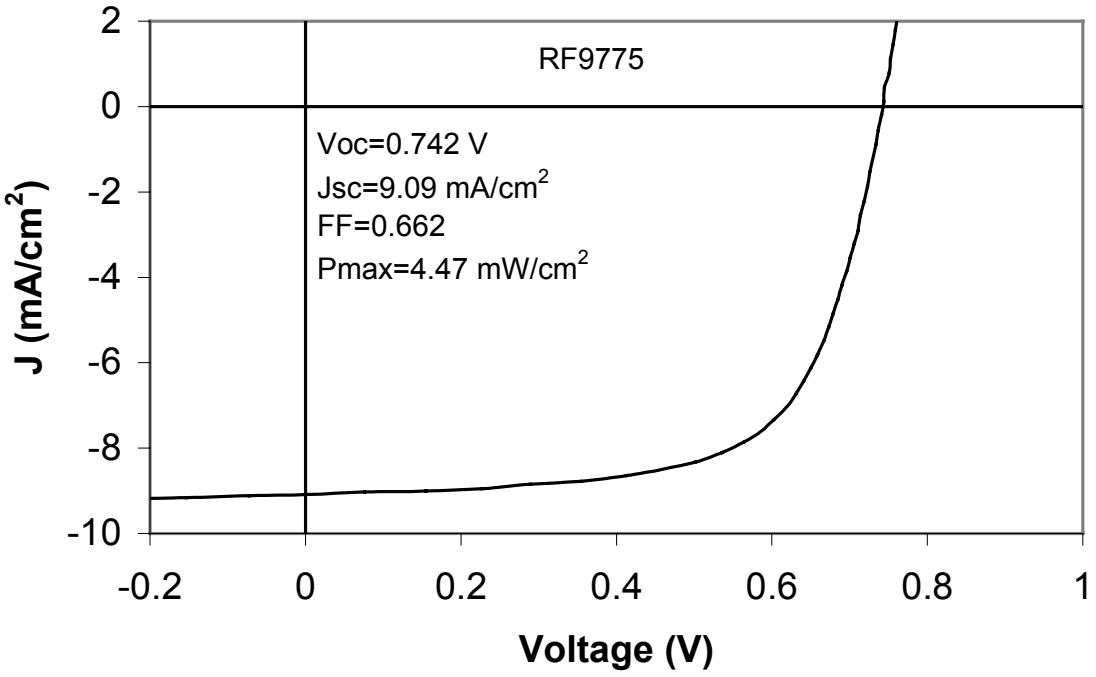

Figure 23. Initial active-area J-V characteristics of a-SiGe alloy middle cell made with MVHF at 6Å/s with an optimized bandgap profile.

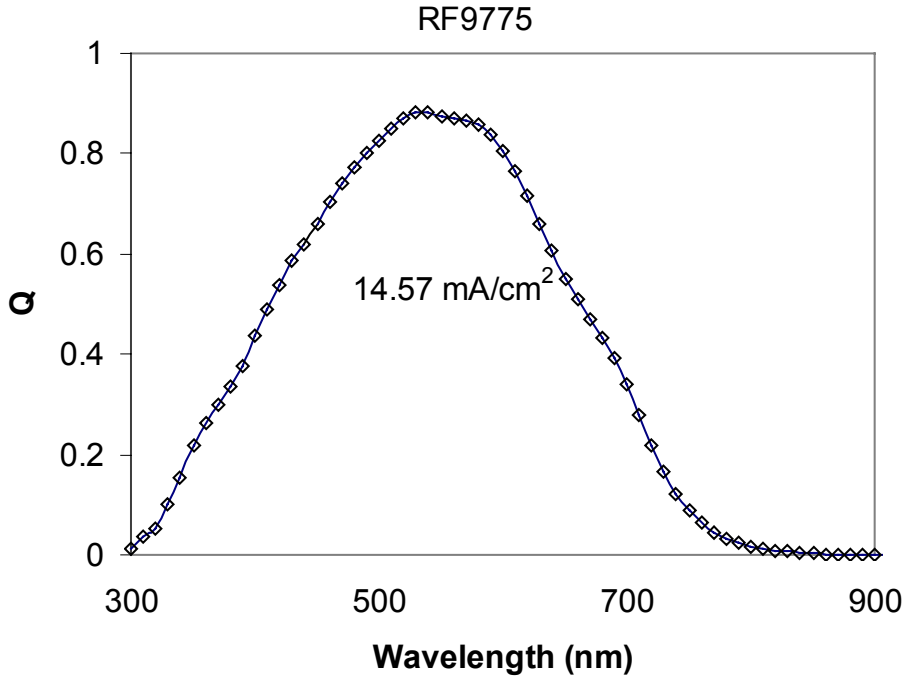

Figure 24. Initial active-area quantum efficiency of MVHF a-SiGe alloy middle cell shown in Fig. 23.

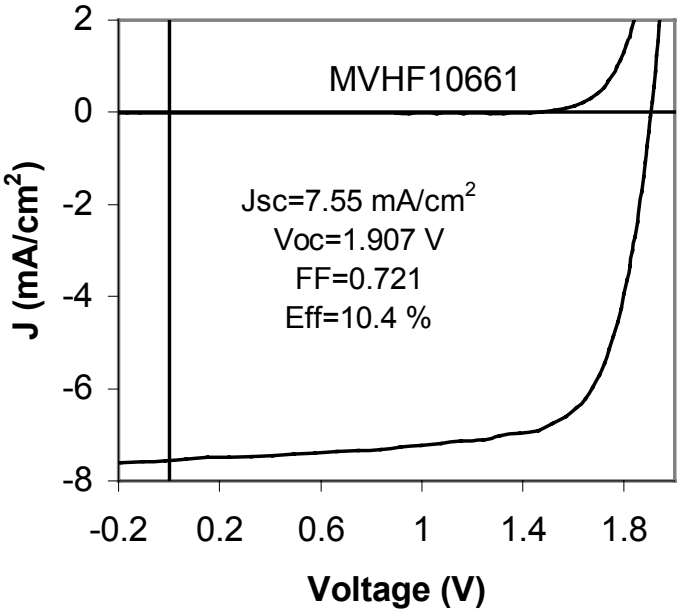

Figure 25. Initial active-area J-V characteristics of the best a-Si/a-Si alloy same bandgap double-junction cell made with MVHF at high rate.

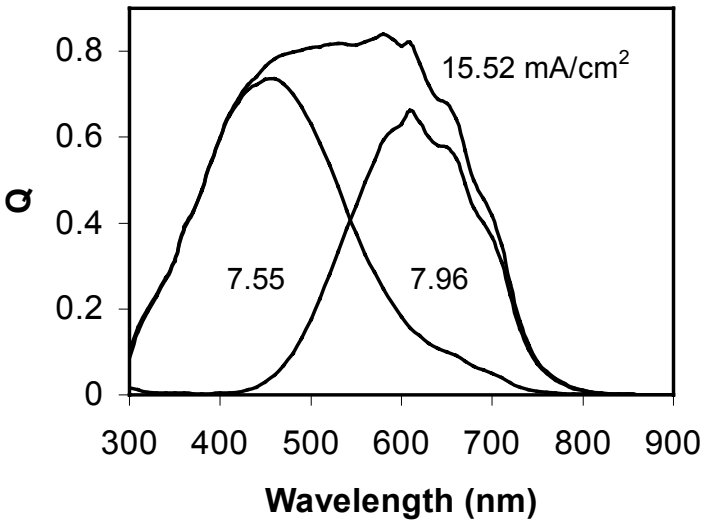

Figure 26. Initial active-area quantum efficiency of a-Si/a-Si alloy double-junction cell shown in Fig. 25.

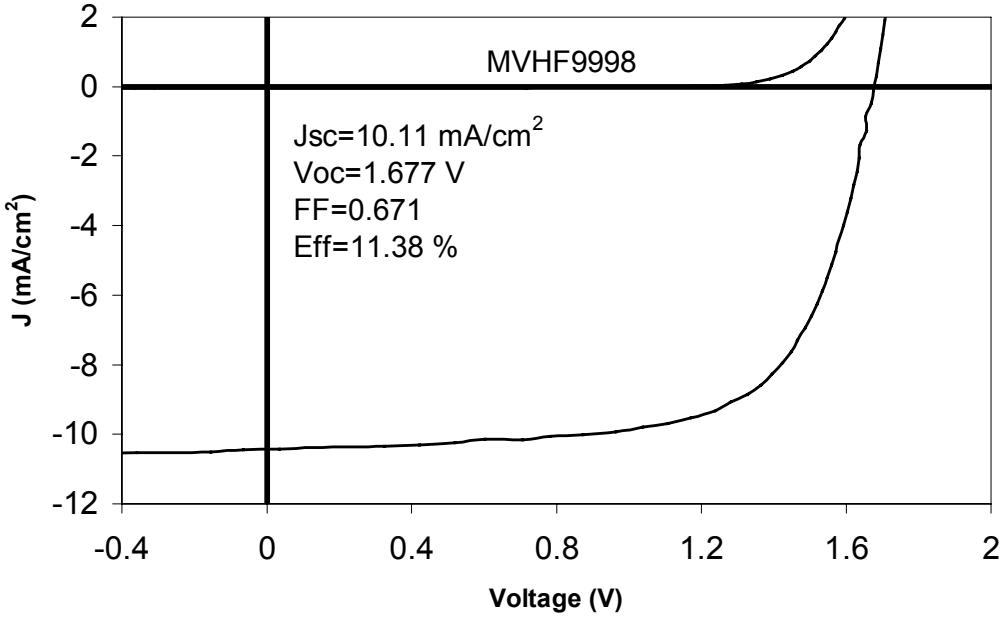

Figure 27. Initial active-area J-V characteristics of the best MVHF a-Si/a-SiGe alloy double-junction solar cell.

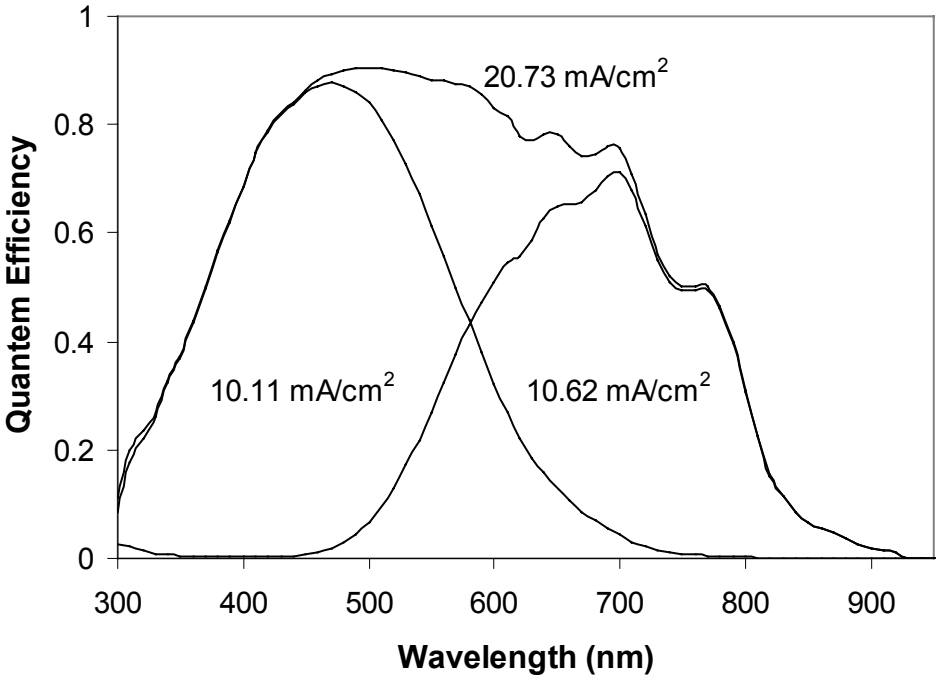

Figure 28. Initial active-area quantum efficiency of the MVHF a-Si/a-SiGe alloy double-junction cell shown in Fig. 27.

Table 23. Initial Active-Area Characteristics of a-Si/a-SiGe Dual-Gap Solar Cells with Different Current Matching. The Top Cells were made at ~8Å/s and the Bottom Cells at ~6Å/s.

Run #	P_{max} (mW/cm^2)	Top, J_{sc} (mA/cm^2)	Bottom, J_{sc} (mA/cm^2)	V_{oc} (V)	FF	Time of top cell
8705	10.92	9.81	10.46	1.672	0.666	185 sec
8704	11.04	10.12	10.50	1.668	0.654	195 sec
8706	10.74	10.22	10.02	1.670	0.642	205 sec

Limited effort has been directed towards the improvement of the performance of a-Si/a-SiGe/a-SiGe triple-junction solar cells prepared by the high-rate MVHF technique. An initial active-area efficiency of 11% has been achieved on such a device. The top cell has been deposited at 8Å/s and the middle and bottom cells have been prepared at 6Å/s. The J-V characteristics and quantum efficiency of the best triple-junction cells are plotted in Figs. 29 and 30, respectively.

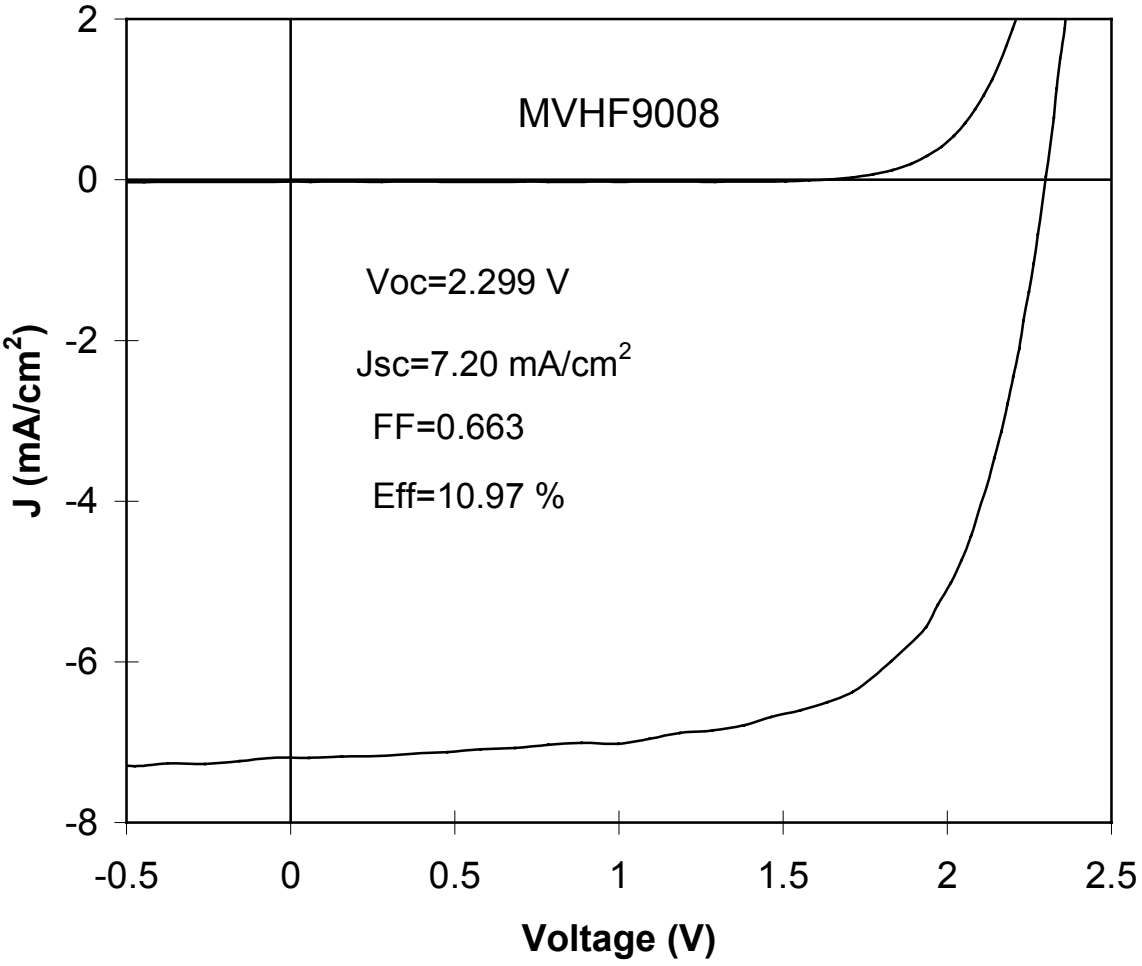

Figure 29. Initial active-area J-V characteristics of the best triple-junction cell made with MVHF at high rate.

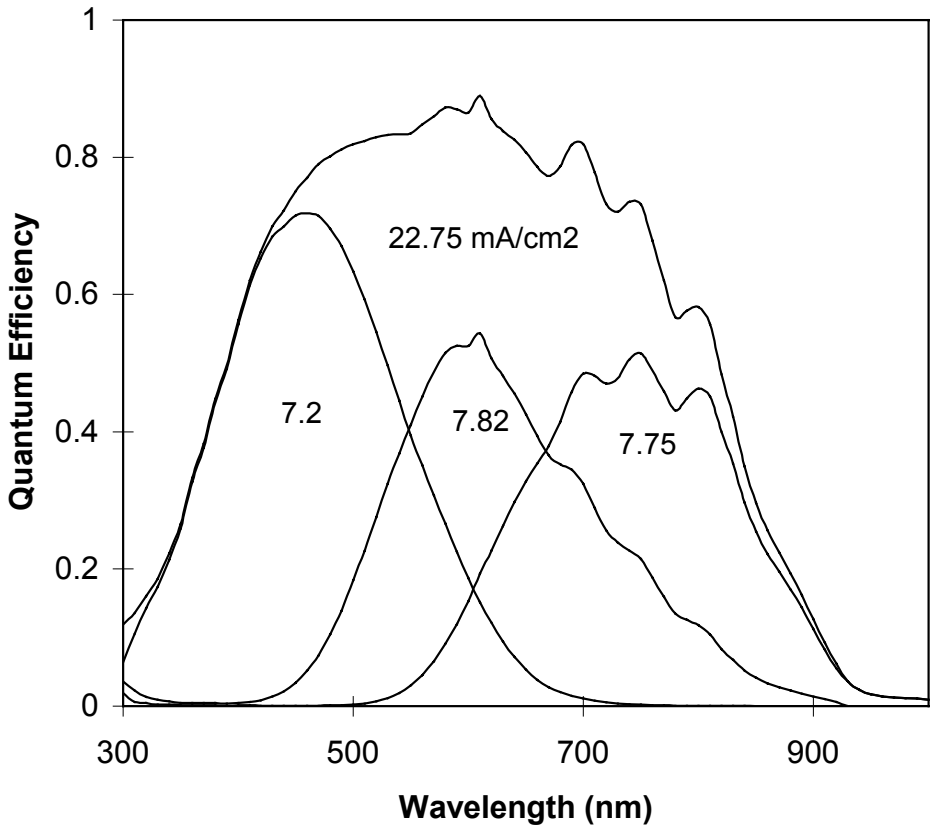

Figure 30. Initial active-area quantum efficiency of the best triple-junction cell made with MVHF at high deposition rate shown in Fig. 29.

Section 5

Stability of a-Si and a-SiGe Alloy Solar Cells made at Various Deposition Rates

5.1. Introduction

It has been found that the high rate deposition of a-Si and a-SiGe alloy solar cells with RF plasma deteriorates not only the initial cell performance, but also the stability. The materials deposited at high rate normally have high density of microvoids and dihydride structures that are responsible for the poorer stability. However, the high rate MVHF deposited a-Si alloy solar cells show initial performance and stability comparable to the low rate RF deposited cells. In order to obtain high efficiency stable multijunction solar cells, it is important to study the stability of a-Si and a-SiGe alloy devices made under various deposition conditions. In this section, we present the stability results of solar cells made using various conditions.

5.2. Initial Annealing of a-Si and a-SiGe Alloy Solar Cells

BP Solarex has reported that gradient temperature annealing at 170^{o}C for 30 minutes, 130^{o}C for 5 hours, and 125^{o}C for 24 hours improved the initial and stable efficiency of double-junction a-Si/a-SiGe solar cells. We have carried out an independent study to determine if the initial annealing can improve our solar cell performance too.

5.2.1. a-Si Alloy Solar Cells

In order to first optimize the initial anneal temperature, a single-junction a-Si alloy solar cell was prepared using MVHF at ~8Å/s. The cell was annealed sequentially at different temperatures for different times as shown in Table 24. The first two hours of anneal at 120^{o}C led to an increase in the FF from 0.717 to 0.722. The V_{oc} and J_{sc} were primarily unchanged and the efficiency increased slightly. Subsequent annealing at 150^{o}C for 2 hours followed by 20 hours annealing at 120^{o}C led to an enhancement in FF but degradation in V_{oc}. Further annealing at 135^{o}C for 20 hours did not improve FF any further but V_{oc} was affected. The annealing studies show that an annealing temperature of 120^{o}C is appropriate. Higher temperatures have a deleterious effect on the cell performance. In order to determine the right anneal time, a new sample was annealed for a longer time ~66 hours at 120^{o}C. The results show (data not presented here) that the 66 hour anneal has no negative impact on the cell performance. The longer anneal time of 66 hours (at 120^{o}C) was adopted as the standard annealing condition in order to ensure that the annealing effect was complete.

Having established the annealing conditions, the effect of initial annealing on the stability of two a-Si alloy single-junction cells prepared by conventional rf glow discharge was investigated. The first sample, L12682, was deposited with high H_2 dilution and the second, L12678, was deposited with no H_2 dilution. Each sample, consisting of 16 cells of total-area 0.268cm^2, was cut into two halves. One half was annealed

Table 24. J-V Characteristics of a MVHF a-Si Alloy Solar Cell at Different States.

States	P_{max} (mW/cm^2)	J_{sc} (mA/cm^2)	V_{oc} (V)	FF
Initial	8.00	11.4	0.977	0.717
120^{o}C, 2 hours	8.05	11.4	0.978	0.722
150^{o}C, 2 hours+120 ^{o}C 20 hours	8.05	11.4	0.975	0.724
135^{o}C 20 hours	7.90	11.3	0.971	0.719

at 120°C for 66 hours. The other half served as the reference. The two halves of the samples L12682 and L12678 were light-soaked at 50°C under one-sun, open-circuit conditions. The J-V characteristics of the solar cells were measured as a function of light soaking time. Table 25 summarizes the solar cell performance of the four halves for the initial, annealed, and light-soaked (stable) conditions. Figures 31 and 32 show the plots of FF versus light soaking time. Both sets showed improvement in FF after the initial annealing. However, after 20 hours of light soak both the annealed and reference samples attained similar values. For both sets, the stable performance of the annealed and reference samples were similar. The cell with high H_2 dilution attained saturation after about 100 hours of light soak but the one with no H_2 dilution did not exhibit stabilization after 1000 hours.

Table 25. J-V Characteristics of RF a-Si Alloy Cells L12682 and L12678 made with High H_2 Dilution and No H_2 Dilution, respectively. The Annealed and Reference Values are Designated as "anneal" and "ref.", respectively.

H_2 dilution	State	P_{max} (mW/cm^2)		J_{sc} (mA/cm^2)		V_{oc} (V)		FF	
		anneal	ref.	anneal	ref.	anneal	ref.	anneal	ref.
High (L12682)	initial	8.61	8.57	11.9	11.9	1.005	1.003	0.720	0.718
	anneal	8.63		11.7		1.009		0.731	
	stable	7.21	7.33	11.4	11.6	0.976	0975	0.648	0.648
None (L12678)	initial	7.64	7.67	12.2	12.1	0.939	0.942	0.667	0.673
	anneal	7.85		12.1		0.940		0.690	
	stable	5.37	5.43	11.3	11.4	0.890	0.890	0.534	0.535

5.2.2. a-SiGe Alloy Solar Cells

A similar experiment has been conducted for a-SiGe alloy solar cells. An MVHF a-SiGe alloy middle cell on stainless steel substrate was cut in half. One half was annealed at 120°C for 66 hours. The other half was the reference sample for comparison. Both halves were light-soaked for 675 hours under one-sun illumination with an appropriate cut-on filter. Table 26 shows results of the initial, annealed, and light-soaked states. As in the case of the a-Si alloy solar cell, there is a gain in FF and V_{oc} after the initial annealing. However, after about 100 hours of light-soak, both samples exhibited similar performance. It has been observed that after 20 hours of light-soak, the annealed sample showed superior J-V characteristics compared to the initial case. This result implies that the rate of degradation is slower for the a-SiGe alloy than for the a-Si alloy. Such a behavior is consistent with our earlier results.

5.2.3. Double-Junction a-Si/a-SiGe Alloy Solar Cells

Initial annealing studies have been carried out on a double-junction a-Si/a-SiGe alloy solar cell. The cell was made using the MVHF technique with high hydrogen dilution. The results are qualitatively similar to the single-junction devices. The results of the double-junction cells are shown in Table 27. There was a gain in P_{max} from 11.21 to 11.46mW/cm^2 after the initial annealing. This advantage was lost after the 100

Table 26. J-V Characteristics of MVHF a-SiGe Alloy Cell made with High H_2 Dilution at ~6Å/s. The Measurements were made under AM1.5 Solar Simulator with a 530nm Cut-On Filter. Annealed and Reference Halves are Designated as "anneal" and "ref.", respectively.

H_2 dilution	State	P_{max} (mW/cm^2)		J_{sc} (mA/cm^2)		V_{oc} (V)		FF	
		anneal	ref.	anneal	ref.	anneal	ref.	anneal	ref.
High	initial	4.74	4.66	9.41	9.16	0.737	0.739	0.684	0.688
	anneal	5.18		9.19		0.743		0.704	
	stable	3.26	3.40	8.69	8.82	0.686	0.699	0.548	0.551

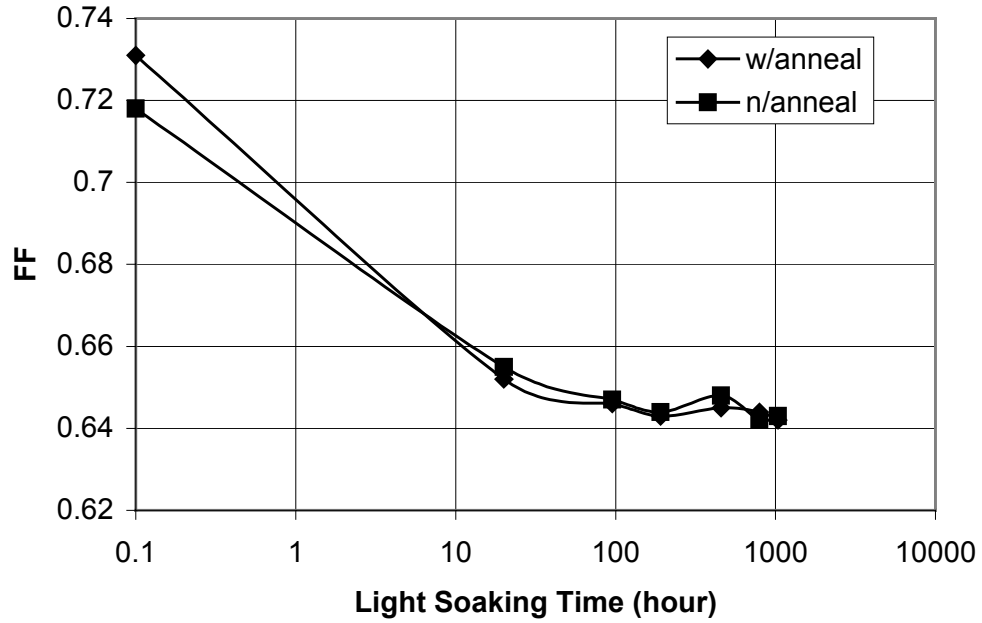

Figure 31. FF versus light soak time for the rf a-Si alloy solar cell made with high H_2 dilution. The diamond represents the cell with initial annealing, and the square represents the reference sample.

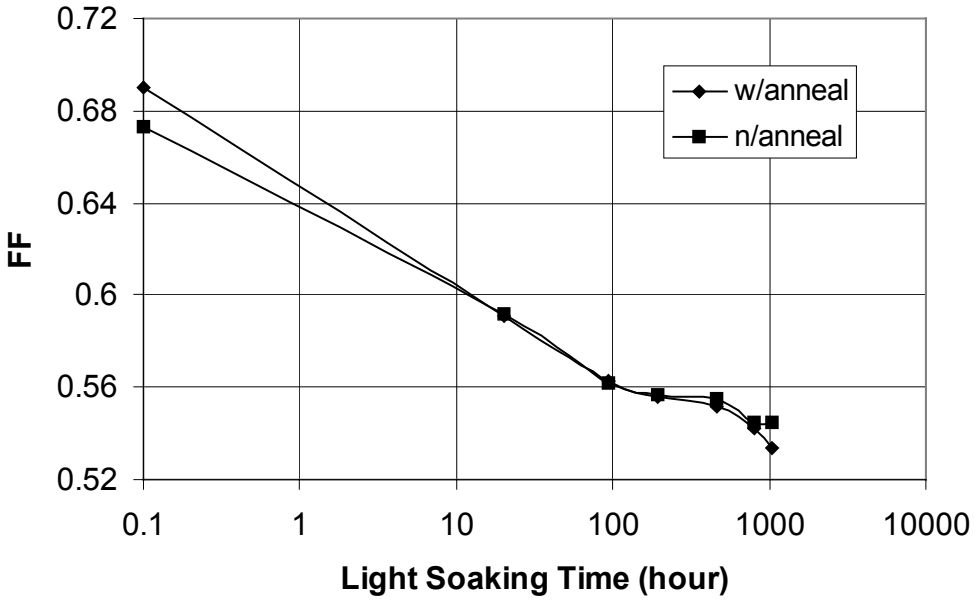

Figure 32. FF versus light soak time for the rf a-Si alloy solar cell made with no H_2 dilution. The diamond represents the cell with initial annealing, and the square represents the reference sample.

Table 27. Summary of J-V Characteristics of the MVHF a-Si/a-SiGe Alloy Double-Junction Cell made with High H_2 Dilution. The 'with' and 'without' stand for with Initial Annealing and without Initial Annealing.

States	P_{max} (mW/cm^2)		J_{sc} (mA/cm^2)		V_{oc} (V)		FF	
	with	without	with	without	with	without	with	without
Initial	11.21	11.15	10.6	10.6	1.673	1.667	0.632	0.631
Annealed	11.46		10.6		1.681		0.644	
604 H	9.74	9.75	10.3	10.3	1.609	1.610	0.588	0.588

hours of light soak. The annealed half and reference half of the substrate exhibited similar performance. After 604 hours of light soak, the P_{max} of the initial-annealed half and the reference-half were 9.74 and 9.75mW/cm^2, respectively.

In summary, we have carried out experiments on the effect of low-temperature, long-time initial annealing on the stability of a-Si alloy, a-SiGe alloy, and double-junction solar cells. Annealing at a temperature 120ºC improves FF and V_{oc}. Higher temperature annealing has a deleterious effect on V_{oc}. Earlier studies have shown that the intrinsic layer of the cells can withstand temperatures >120ºC. It is speculated that the thermal equilibrium temperature for the doped layers p and/or n is low which, in turn, limits the annealing temperature to 120ºC. The gain of FF due to initial annealing may be attributed to the reduction of stress and unstable defects in the film that were quenched-in during the removal of the samples from the reactor. In contrast to the BP Solarex results, we have not seen an improvement in the stable efficiency of single-junction a-Si alloy and a-SiGe alloy and double-junction solar cells. The gain from the initial annealing is lost after light soak.

5.3. Comparison of the Stability of RF and MVHF a-Si Alloy Solar Cells

Top, middle and bottom component cells were fabricated in three small-area deposition systems. The experiments were conducted to compare the stability of cells deposited with RF and MVHF plasmas. The three systems were the Line (L9654 ~1Å/s RF), BMW (B3467 ~3Å/s RF), and VHF (VHF6960 ~6Å/s MVHF). The initial and stabilized J-V characteristics of the RF solar cells deposited at 1Å/s and 3Å/s and the MVHF cells deposited at ~6Å/s were compared. The middle and bottom cells were deposited without bandgap profiling to compare similar cells. State-of-the-art middle and bottom RF cells deposited with bandgap profiling at ~1Å/s were also compared.

The initial and stabilized active-area characteristics of a-Si alloy top cells deposited on stainless steel substrate are listed in Table 28. As reported earlier, the initial characteristics of the a-Si alloy top cell are the best for RF at 1Å/s. The initial characteristics of the 3Å/s RF cell are superior to the 6Å/s MVHF cell, but the stabilized characteristics of the 6Å/s VHF cell is better than the 3Å/s RF cell.

Table 28. Initial and Stabilized Characteristics of Top Component Cells on Stainless Steel.

Sample	Status	J_{sc} (mA/cm^2)	V_{oc} (V)	FF	Efficiency (%)		Deg. Rate (%)	Comment
					Active	Total		
L9654	Initial	8.65	1.016	0.771	6.78	6.31		RF ~1Å/s
	Stable	8.20	0.965	0.711	5.63	5.24	17	
B3467	Initial	8.74	0.962	0.750	6.31	5.87		RF ~3Å/s
	Stable	8.41	0.905	0.656	4.99	4.64	21	
VHF6960	Initial	8.66	0.997	0.691	5.97	5.55		MVHF ~6Å/s
	Stable	8.22	0.955	0.664	5.21	4.85	13	

We light-soaked another set of optimized MVHF top cells. The results are summarized in Table 29. The stabilized efficiencies of the four cells exceed the milestone (active-area efficiency of 5.1%) of Phase III for the high-rate top cell. The highest stabilized active-area efficiency is 5.80%, which is equivalent to total-area efficiency of 5.39%. Figure 33 shows the J-V characteristics and quantum efficiency of this top cell in the initial and stabilized states.

Table 29. Stability of a-Si Alloy Top Cells made with MVHF at ~8Å/sec.

Run #	State	P_{max} (total) (mW/cm^2)	P_{max} (active) (mW/cm^2)	J_{sc} (mA/cm^2)	V_{oc} (V)	FF	Deg. (%)
9078	Initial	5.95	6.40	8.67	0.994	0.743	
	1000 h	5.17	5.56	8.39	0.959	0.691	13.1
9087	Initial	5.99	6.44	8.49	1.004	0.756	
	1000 h	5.19	5.58	8.32	0.963	0.697	13.4
9196	Initial	5.85	6.29	8.57	0.979	0.750	
	1000 h	5.15	5.54	8.53	0.944	0.688	11.9
9254	Initial	**6.15**	**6.61**	**8.84**	**1.002**	**0.746**	
	1000 h	**5.39**	**5.80**	**8.74**	**0.960**	**0.691**	**12.3**

The J-V characteristics of the a-SiGe alloy middle cells deposited on stainless steel and illuminated with a $\lambda > 530$nm cut-on filter are listed in Table 30. The RF cells deposited at ~1Å/s exhibit the highest initial and stabilized P_{max}. The use of bandgap profiling results in a 16% increase in the initial $P_{max.}$ However, both low deposition rate cells with and without bandgap profiling degraded by 20% yielding a 16% higher stabilized P_{max} for the profiled cell. The initial characteristics of the 3Å/s RF and 6Å/s MVHF cells are similar, and both cells exhibited similar degradation yielding similar stabilized P_{max}.

Table 30. Initial and Stabilized Characteristics of Middle Component Cells on Stainless Steel.

Sample	Condition	J_{sc} (mA/cm^2)	V_{oc} (V)	FF	P_{max} (mW/cm^2)		Deg. Rate (%)	Comment
					Active	Total		
L10524	Initial	9.53	0.759	0.702	5.08	4.72		Profiled
	Stable	9.06	0.725	0.616	4.05	3.77	20	RF ~1Å/s
L10547	Initial	8.66	0.751	0.656	4.27	3.97		No profile
	Stable	8.33	0.723	0.566	3.41	3.17	20	RF ~1Å/s
B4576	Initial	7.47	0.764	0.672	3.84	3.57		No profile
	Stable	7.05	0.723	0.552	2.81	2.61	27	RF ~3Å/s
VHF7797	Initial	7.90	0.766	0.650	3.93	3.65		No profile
	Stable	7.48	0.718	0.548	2.94	2.73	25	MVHF ~6Å/s

The initial and stabilized characteristics of a-SiGe alloy bottom cells deposited on AgZnO back reflectors are listed in Table 31. Again, the 1Å/s RF cells exhibit the highest initial and stabilized P_{max}. The degradation in the bottom cells with or without bandgap profiling is similar. The effect of bandgap profiling is to increase the initial and stabilized P_{max} by 16%. The RF cells deposited at 1 and 3Å/s exhibit similar degradation. However, the 6Å/s MVHF bottom cell exhibited the most degradation.

5.4. Annealing Kinetics of a-Si Alloy Solar Cells made at Various Deposition Rates

The optically induced degradation of a-Si alloy solar cell is normally believed to be due to the generation of silicon dangling bonds. The stabilized efficiency is reached as a result of the balance of thermal annealing and light-induced defect generation. A question that remains is whether the different stability observed for cells prepared by the two deposition techniques is due to different generation rate or different annealing kinetics.

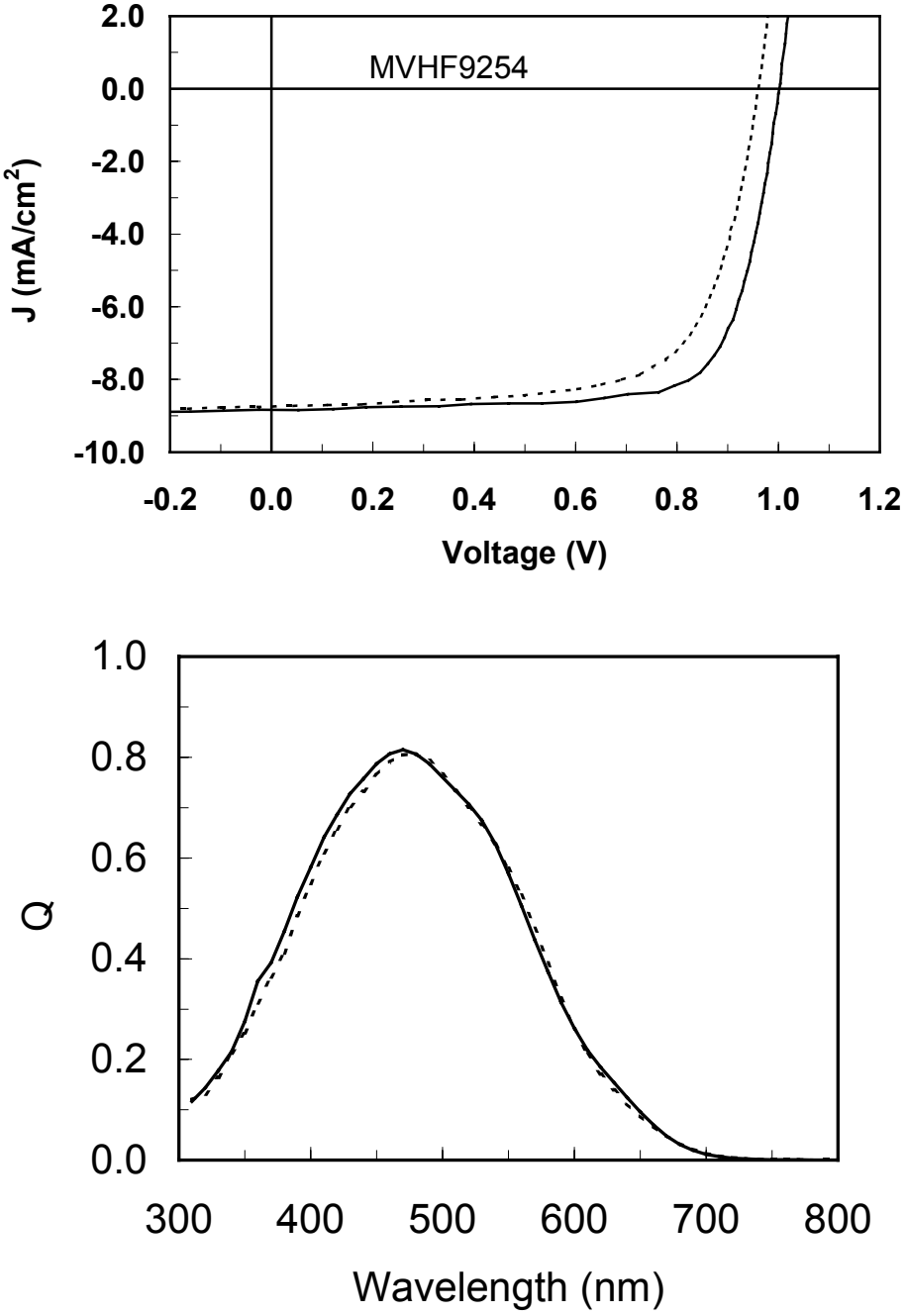

Figure 33. J-V characteristics and quantum efficiency of the best top cell made with MVHF at 8Å/s. The solid and dashed curves indicate the initial and stabilized states, respectively.

Table 31. Initial and Stabilized Characteristics of Bottom Component Cells on Back Reflector.

Sample	Condition	J_{sc} (mA/cm^2)	V_{oc} (V)	FF	P_{max} (mW/cm^2)		Deg. Rate (%)	Comment
					Active	Total		
L10650	Initial	11.72	0.586	0.641	4.40	4.09		Profiled
	Stable	11.43	0.564	0.587	3.78	3.52	14	RF ~1Å/s
L10655	Initial	9.78	0.620	0.631	3.83	3.56		No profile
	Stable	9.38	0.594	0.578	3.22	2.99	16	RF ~1Å/s
B4556	Initial	10.27	0.610	0.583	3.65	3.39		No profile
	Stable	9.84	0.583	0.552	3.17	2.95	13	RF ~3Å/s
VHF7902	Initial	9.20	0.624	0.600	3.44	3.20		No profile
	Stable	8.77	0.597	0.535	2.80	2.60	19	MVHF ~6Å/s

We have carried out stability studies on a-Si alloy solar cells deposited at different deposition rates. Four pin solar cells were fabricated using RF glow discharge at 1Å/s with high hydrogen dilution, 3Å/s with medium hydrogen dilution, and 10Å/s with no hydrogen dilution. Another sample was made with MVHF at 8Å/s with high hydrogen dilution. The thickness of the intrinsic layer was ~2300Å. The samples were light-soaked under white light with an intensity of 30 suns at room temperature, which enhances the defect generation and suppresses the thermal annealing during light soaking. Table 32 summarizes the J-V characteristics of these solar cells in their annealed and light-soaked states. Most cells stabilize after less than one hour of 30 suns light soaking. The 10Å/s no-dilution cell saturated after 2 hours of light soaking. The degradation is similar for the high hydrogen dilution 8Å/s MVHF cell and 1Å/sec RF cell. This result is consistent with our previous report on thin top cell stability studies. The degradation of the undiluted 10Å/s cell is over 50%, which is the largest among the four cells.

After light soaking, the samples were annealed at elevated temperatures for different time intervals. The solar cell performance was measured as a function of annealing time. The correlation of the J-V characteristics with the defect density in the intrinsic layer was modeled using AMPS simulation. Figure 34 shows the annealing kinetics of light-induced defect density at 100ºC, where the dots are experimental values and the lines are the fittings obtained from the AMPS model. The Gaussian distribution of the annealing activation energy is plotted in Fig. 35. Table 33 gives the summary of the Gaussian distribution parameters of the four samples, where E_0 and W are the peak position and the width of the distribution, respectively.

The above study shows that the RF cell deposited at 1Å/s with high hydrogen dilution has the highest annealing rate corresponding to the lowest annealing activation energy with the narrowest distribution. The RF cell deposited at 10Å/s without hydrogen dilution has the lowest annealing rate, corresponding to the highest annealing activation energy with the broadest distribution. The MVHF 8Å/s cell has higher

Table 32. Initial and Light-Soaked J-V Characteristics of a-Si Alloy Solar Cells made at Different Rates.

Sample	State	Eff (%)	J_{sc} (mA/cm^2)	V_{oc} (V)	FF	Deg. (%)	LS time (Hour)
High H_2 - 1 Å/s	Initial	8.0	10.7	1.012	0.738		
(RF)	Degraded	4.9	9.9	0.937	0.528	38.8	1
Medium H_2 - 3 Å/s	Initial	7.1	10.9	0.972	0.667		
(RF)	Degraded	3.9	9.0	0.872	0.499	45.1	1
High H_2 - 8 Å/s	Initial	8.0	11.	0.972	0.727		
(MVHF)	Degraded	5.0	10.4	0.908	0.530	37.5	1
No H_2 - 10 Å/s	Initial	7.0	11.9	0.921	0.640		
(RF)	Degraded	3.5	9.1	0.841	0.460	49.7	1
	Degraded	3.1	8.4	0.830	0.444	55.6	4

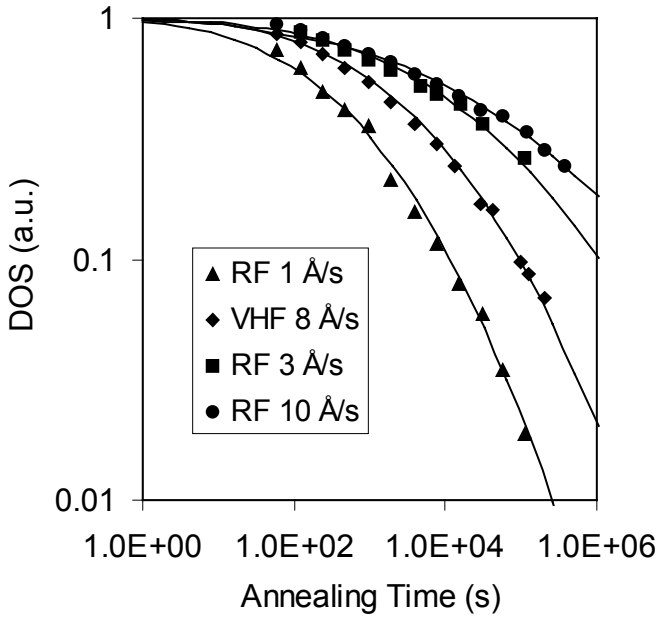

Figure 34. Annealing kinetics at 100°C of normalized light-induced defect density.

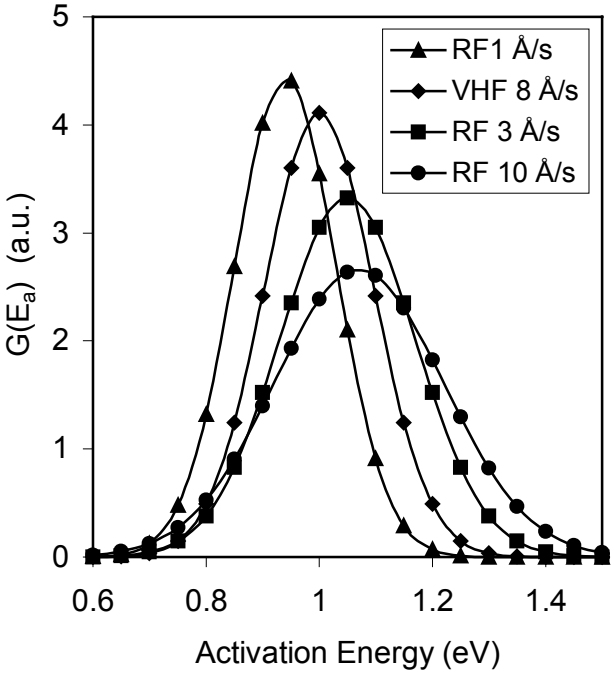

Figure 35. The annealing activation energy distribution of a-Si alloy solar cells deposited at different deposition rates.

Table 33. Density of Defect States and Annealing Activation Energy Distribution Parameters for a-Si Alloy Solar Cells Deposited at Different Rates.

Sample	State	DOS (10^{16} cm^{-3})	LS time (Hour)	E_0 (eV)	W (eV)
High H_2 - 1 Å/s (RF)	Initial	0.316			
	Degraded	11.7	1	0.94	0.090
Medium H_2 - 3 Å/s (RF)	Initial	2.34			
	Degraded	14.2	1	1.05	0.120
High H_2 - 8 Å/s (MVHF)	Initial	0.468			
	Degraded	11.5	1	1.00	0.097
No H_2 - 10 Å/s (RF)	Initial	3.97			
	Degraded	18.4	1	1.07	0.150
	Degraded	20.2	4	1.09	0.150

annealing rate than the RF 3Å/s cell. The different annealing activation energy distributions may be related to the different hydrogen diffusion in the materials. Measurement of the diffusion coefficient of hydrogen in a-Si alloy films made under different deposition conditions may elucidate the mechanism of light induced degradation of a-Si alloy based solar cells.

5.5. Stability Study

Stability studies have been carried out on the component and multijunction cells prepared by the MVHF high-rate technique. The light soaking was done at 50°C under 100mW/cm^2 white light for the top cell and multijunction cell. For middle cells on stainless steel and bottom cells on back reflectors, we use one-sun white light with appropriate filters to simulate their respective operation in a triple-junction structure. The stable efficiency is attained after a few hundred hours of light soak. The stable data reported here are those after >1000 hours of illumination. The performance of the best stable and initial value solar cells is summarized in Table 34. The stable data shown in the table do not correspond to the cells with the highest initial efficiency. It is expected that stable results of the best initial-performance devices will be superior to the stable data shown in the table.

Table 34. Initial and Stable J-V Characteristics of Component and Multijunction Solar Cells of Various Structures. The Solar Cells were Made with MVHF at High Deposition Rates.

Structure	State	Run #	P_{max} (mW/cm^2)	J_{sc} (mA/cm^2)	V_{oc} (V)	FF
Top[a,c]	Initial	10546	6.96	9.05	1.016	0.757
	Stable	9254	5.80	8.74	0.960	0.697
Middle[a,d]	Initial	9775	4.47	9.09	0.742	0.662
	Stable	7733	3.15	7.58	0.720	0.577
Bottom[b,e]	Initial	7298	3.84	10.00	0.623	0.616
	Stable	7902	2.80	8.77	0.597	0.535
a-Si/Si Tandem[b,c]	Initial	10661	10.40	7.55	1.907	0.721
a-Si/a-SiGe Tandem[b,c]	Initial	9998	11.38	10.11	1.677	0.671
	Stable	8704	9.14	9.47	1.606	0.601
Triple[b,c]	Initial	9008	10.97	7.20	2.299	0.663

a: Deposited on a bare stainless steel substrate
b: Deposited on a textured Ag/ZnO back reflector
c: Measured under AM1.5 illumination
d: Measured under AM1.5 with a λ>530nm filter
e: Measured under AM1.5 with a λ>630nm filter

Section 6

Status of Amorphous Silicon Alloy Component and Multijunction Cells and Modules Deposited in a Large-Area Reactor

6.1. Introduction

A prerequisite to fabricating high efficiency modules of aperture area 460-920cm^2 is to optimize the performance and the uniformity of smaller area cells. This approach enables the diagnosis and analysis of the devices at both the cell and module levels. Evaluation of the small-area (total area = 0.268cm^2, active area = 0.25cm^2) cells using I-V and Q measurements provide information about the basic device efficiency without the complications of electrical and optical losses associated with modules. It also enables the evaluation and optimization of the device at the component cell level.

6.2. Device Fabrication and Measurement

A large-area stainless steel substrate is first sputter-coated with a textured Ag/ZnO back reflector layer. The deposition is over an area of ~1 sq. ft. This is followed by the deposition over the same area of a triple-junction triple-bandgap a-Si/a-SiGe/a-SiGe alloy cell in the 2B machine using conventional glow discharge technique. The top transparent conducting oxide (TCO) is deposited in two different configurations as follows:

6.2.1. Small-Area (0.268cm^2) Devices

This process allows the complete and in-depth evaluation of the component cells and light soaking characteristics of both the component and triple-junction cells. In this method, the completed large-area device is cut into 2"x2" substrates. The TCO is deposited through an evaporation mask to yield devices of total area 0.268cm^2. These devices are used for I-V and Q measurements. Stable cell results are obtained by exposing several of the representative 2"x2" samples obtained from the original 900cm^2 substrate.

6.2.2. Module Fabrication

This process is for the fabrication of modules. The TCO film is deposited over the entire area. The TCO film is then etched to fabricate a module of aperture area 460cm^2. Front surface grids are applied using a wire bonding process and bus bars are connected. The unencapsulated modules are measured in a Spire pulsed solar simulator Model 240A equipped with a peak detector circuit board. The modules are then encapsulated using a stack of Tefzel and EVA. Another set of I-V measurements is made on the encapsulated modules under the Spire solar simulator.

6.3. Stability Studies

Two kinds of samples were used for the stability studies. The first were the small-area (0.268cm^2) component and triple-junction cells and the second were the modules. For the small-area cells, several 2"x2" substrates encompassing several unencapsulated 0.268cm^2 total area devices were first measured. The average efficiency was obtained on each substrate. The average efficiency of all the substrates gives an estimate of the expected initial module efficiency. Only encapsulated modules were used for the light soaking. The small-area light soak was done at United Solar whereas the modules were light soaked at NREL. The light soaking for all the small-area samples was done under one-sun, 50^{0}C, and open-circuit conditions for >1000 hours.

6.4. Results of Component Cells

6.4.1. Top Cell on Stainless Steel Substrate

Six 2"x2" substrates, representing the large-area stainless steel substrate with no back reflector, were selected. The average of the J-V characteristics of the small-area cells is assumed to be representative of the large-area device. The initial and stable performance after 1000 hours of light soak of the six sets of devices and their average values are listed in Table 35. Each value in the table represents the average of several 0.268cm^2 devices on that substrate. The light soaking was done under AM1.5 global illumination at 50^{0}C and open-circuit conditions. The table shows that the average values of the stable total-area efficiency for the six substrates are in the range of 5.2-5.8mW/cm^2. The average for all the substrates shown at the bottom of Table 35 is 5.5mW/cm^2 and is representative of the entire large-area 12"x12" substrate. The stabilized total-area P_{max} of 5.5mW/cm^2 meets the Phase III milestone of 5.4mW/cm^2.

Table 35. Average Results of Small-Area a-Si Alloy Top Cells on 2"x2" Stainless Steel Substrate.

Sample 2B7082	Active-area (cm^2)	Total-area (cm^2)	Light Soak (Hours)	J_{sc} (mA/cm^2)	V_{oc} (V)	FF	P_{max} (mW/cm^2)	
							Active area	Total area
LH4	0.25	0.268	0	9.37	0.992	0.711	6.6	6.1
			1000	9.16	0.985	0.677	6.1	5.7
LD4	0.25	0.268	0	9.01	1.023	0.717	6.6	6.1
			1000	8.86	0.993	0.680	6.0	5.6
LB2	0.25	0.268	0	8.82	1.015	0.703	6.3	5.9
			1000	8.61	0.993	0.675	5.8	5.4
LB6	0.25	0.268	0	9.21	1.009	0.728	6.8	6.3
			1000	9.06	0.990	0.686	6.2	5.8
LC1	0.25	0.268	0	8.31	1.020	0.781	6.6	6.1
			1000	8.22	0.992	0.686	5.6	5.2
LE	0.25	0.268	0	8.66	1.015	0.737	6.5	6.0
			1000	8.59	0.990	0.675	5.7	5.3
Average	**0.25**	**0.268**	**0**	**8.90**	**1.012**	**0.730**	6.6	**6.1**
			1000	**8.75**	**0.991**	**0.680**	5.9	**5.5**
Phase III milestone		***1.0***	***1000***					***5.4***

6.4.2. Middle Cell on Stainless Steel Substrate

Similar work has been done on the middle cell on stainless steel substrate with no back reflector. Six representative 2"x2" pieces with 0.268cm^2 total-area devices were prepared. The initial performance of the devices was measured under AM1.5 illumination using a λ>530nm cut-on filter. The devices were then light-soaked under open circuit, one sun with filter, and 50^{0}C conditions. The filter was selected such that the intensity corresponded to a J_{sc} ~8-9mA/cm^2. The initial and 1655 hours light-soaked results of the six substrates are summarized in Table 36. Each value in the table represents the average of several 0.268cm^2 devices on that substrate. The average stable values of P_{max} at λ>530nm for the six substrates are in the range of 3.46-3.82mW/cm^2. The average for all the substrates shown at the bottom of Table 36 is 3.7mW/cm^2 and is representative of the entire large-area 12"x12" substrate. The stabilized value of 3.7mW/cm^2 meets the Phase III milestone of 3.3mW/cm^2 for the third year of the program.

6.4.3. Bottom Cell on Ag/ZnO Back Reflector

For the bottom cell, a Ag/ZnO back reflector substrate has been used. Six representative 2"x2" pieces with 0.268cm^2 total-area devices were prepared. The initial performance of the devices was measured under

Table 36. Average Results of Small-area a-SiGe Alloy Middle Cells on a 2"x2" Stainless Steel Substrate.

Sample 2B6812	Active-area (cm^2)	Total-area (cm^2)	Light Soak (Hours)	J_{sc} (mA/cm^2)	V_{oc} (V)	FF	P_{max}>530nm (mW/cm^2)	
							Active area	Total area
LA2	0.25	0.268	0	11.1	0.777	0.651	5.64	5.3
			1655	10.25	0.724	0.528	3.93	3.67
LD3	0.25	0.268	0	11.1	0.780	0.642	5.56	5.2
			1655	10.28	0.727	0.516	3.86	3.60
LF2	0.25	0.268	0	10.9	0.776	0.648	5.48	5.1
			1655	10.34	0.728	0.541	4.09	3.82
LC0	0.25	0.268	0	11.1	0.778	0.657	5.66	5.3
			1655	10.27	0.724	0.531	3.95	3.69
LE	0.25	0.268	0	10.2	0.786	0.649	5.21	4.8
			1655	9.36	0.731	0.542	3.71	3.46
LB1	0.25	0.268	0	11.2	0.777	0.648	5.61	5.2
			1655	10.32	0.727	0.536	4.02	3.75
Average	**0.25**	**0.268**	**0**	**10.9**	**0.779**	**0.649**	**5.53**	**5.2**
			1655	**10.14**	**0.727**	**0.532**	**3.93**	**3.7**
Phase III milestone		***1.0***	***1000***					***3.3***

AM1.5 illumination using a λ>630nm cut-on filter. The devices were then light-soaked under open circuit, one sun with filter, and 50^0C conditions. The filter was selected such that the intensity corresponded to a J_{sc} of 8.5-9.5mA/cm^2. The initial and 1076 hour light soak results of the six substrates are summarized in Table 37. Each value in the table represents the average of several 0.268cm^2 devices on that substrate. The average stable values of total-area P_{max} at λ>630nm for the six substrates are in the range of 3.2-3.5mW/cm^2. The average for all the substrates shown at the bottom of Table 37 is 3.4mW/cm^2 and is representative of the large-area 12"x12" substrate. The stabilized value of 3.4mW/cm^2 is close to the Phase III milestone of 3.5mW/cm^2 for the third year of the program.

Table 37. Average Results of Small-area a-SiGe Alloy Bottom Cells on 2"x2" Ag/ZnO Substrate.

Sample 2B6439	Active-area (cm^2)	Total-area (cm^2)	Light Soak (Hours)	J_{sc} (mA/cm^2)	V_{oc} (V)	FF	P_{max}>630nm (mW/cm^2)	
							Active area	Total area
LE	0.25	0.268	0	12.08	0.606	0.613	4.5	4.2
			1076	11.81	0.567	0.549	3.7	3.5
LB1	0.25	0.268	0	12.08	0.590	0.613	4.4	4.1
			1076	11.81	0.567	0.547	3.7	3.4
LD1	0.25	0.268	0	12.08	0.583	0.610	4.3	4.0
			1076	11.81	0.560	0.541	3.6	3.3
LC2	0.25	0.268	0	12.08	0.600	0.611	4.4	4.1
			1076	11.81	0.575	0.527	3.6	3.3
LG3	0.25	0.268	0	12.08	0.589	0.608	4.3	4.0
			1076	11.81	0.566	0.520	3.5	3.2
LA6	0.25	0.268	0	12.08	0.606	0.605	4.4	4.1
			1076	11.81	0.581	0.524	3.6	3.4
Average	**0.25**	**0.268**	**0**	**12.08**	**0.596**	**0.610**	**4.4**	**4.1**
			1076	**11.81**	**0.572**	**0.533**	**3.6**	**3.4**
Phase III milestone		***1.0***	***1000***					***3.5***

6.5. Results of Triple-Junction Cells

Triple-junction triple-bandgap a-Si/a-SiGe/a-SiGe alloy cells were deposited on Ag/ZnO back reflector. Small-area cell performance was measured on four 2"x2" substrates, representing the large-area substrate. The initial and the stabilized results after 1067 hours of light soak are shown in Table 38. Each value in the table represents the average of several 0.268cm^2 devices on that substrate. The overall average values of initial efficiency of all the substrates are active-area efficiency = 14.3% and total-area efficiency = 13.3%. The corresponding values for the 1067 hours light stabilized case are 12.5% and 11.6%, respectively, and is representative of the large-area 12"x12" substrate. The Phase III milestone, shown in the same table, for the stabilized total-area efficiency is 12.2%. The stabilized total-area efficiency of 11.6% is slightly shy of the Phase III milestone. One reason for not meeting this milestone was the change in focus of the large-area reactor research aspect of the program towards fabrication of cells and modules using production technology (discussed in Section 7). The new work took precedence and the earlier objective was scaled back.

Table 38. Average Results of Small-area Triple-junction Cells on 2"x2" Ag/ZnO Back Reflector.

Sample 2B5735	Active area (cm^2)	Total area (cm^2)	Light Soak (Hours)	J_{sc} (mA/cm^2)	V_{oc} (V)	FF	Efficiency (%)	
							Active area	Total area
LE	0.25	0.268	0	8.84	2.281	0.708	14.3	13.3
			1067	8.64	2.209	0.660	12.6	11.7
LF4	0.25	0.268	0	8.77	2.279	0.717	14.3	13.4
			1067	8.49	2.208	0.664	12.5	11.6
LD4	0.25	0.268	0	8.81	2.280	0.713	14.3	13.4
			1067	8.43	2.207	0.666	12.4	11.6
LC1	0.25	0.268	0	8.77	2.250	0.718	14.2	13.2
			1067	8.49	2.178	0.674	12.5	11.6
Average	**0.25**	**0.268**	**0**	**8.80**	**2.273**	**0.714**	**14.3**	**13.3**
			1067	**8.51**	**2.201**	**0.666**	**12.5**	**11.6**
Phase III milestone		***1.0***	***1000***					***12.2***

6.6. Module Results

The module fabrication process has been briefly described above. Two kinds of modules have been fabricated corresponding to the two aperture areas: (1) ~460 cm^2 and (2) ~920 cm^2. All I-V measurements have been made using a Spire pulsed solar simulator equipped with a peak detector circuit board. The initial results of the modules are described.

6.6.1. Modules of Aperture Area ~460cm^2

Table 39 summarizes the initial measurements of twenty-eight unencapsulated modules of aperture area ~460cm^2. The conversion efficiency is in the range of 11.9-12.7%. The average efficiency of all the modules is 12.25%. Two modules, 6915 and 6972, exhibit the highest efficiency of 12.7% which is the highest value obtained to date on such a module. The I-V characteristics of the module 6915 are shown in Figure 34. The initial values of the module are efficiency = 12.68%, P_{max} = 5.88W, V_{oc} = 2.403V, I_{sc} = 3.617A, and FF = 0.676.

6.6.2. Modules of Aperture Area ~920cm^2

Some of the modules shown in Table 39 have been encapsulated to fabricate modules of aperture area ~920cm^2. The initial Spire I-V characteristics of ten encapsulated modules are summarized in Table 40. The efficiency is in the range of 11.7-12.5%. The I-V characteristics of module 691548L are shown in Fig. 35.

Table 39. Initial Spire I-V Characteristics of Unencapsulated Modules.

Serial # 2B	Aper. Area (cm^2)	Temp (^0C)	V_{oc} (V)	I_{sc} (A)	FF	P_{max} (W)	V_{mp} (V)	R_s (ohm)	R_{sh} (ohm)	Efficiency (%)
6782	466.3	22.0	2.362	3.630	0.661	5.66	1.910	0.09	3.9	12.15
6835	462.3	23.4	2.336	3.817	0.633	5.64	1.776	0.10	3.6	12.20
6839	462.3	23.4	2.336	3.762	0.629	5.53	1.764	0.11	3.7	11.95
6841	462.3	23.7	2.337	3.542	0.669	5.54	1.794	0.10	5.5	11.98
6843	462.3	21.2	2.350	3.580	0.656	5.52	1.831	0.10	4.8	11.95
6854	462.3	21.5	2.351	3.450	0.682	5.53	1.886	0.09	5.2	11.96
6861	462.3	21.0	2.357	3.733	0.646	5.69	1.801	0.10	4.8	12.31
6867	462.3	21.0	2.356	3.613	0.663	5.64	1.831	0.10	4.4	12.21
6870	462.3	22.7	2.351	3.564	0.659	5.52	1.874	0.10	4.6	11.95
6883	462.2	22.7	2.357	3.500	0.679	5.60	1.880	0.11	4.8	12.12
6887	464.3	20.3	2.378	3.691	0.663	5.82	1.868	0.11	4.0	12.54
6896	463.3	22.2	2.338	3.386	0.694	5.49	1.874	0.08	5.2	11.86
6909	463.3	22.2	2.381	3.643	0.661	5.74	1.917	0.10	4.6	12.38
6914	462.3	22.0	2.361	3.396	0.695	5.57	1.910	0.09	6.0	12.05
6915	463.3	22.2	2.403	3.617	0.676	5.88	1.862	0.10	4.7	12.68
6927	462.3	22.5	2.370	3.471	0.673	5.54	1.868	0.09	4.0	11.98
6930	464.4	22.5	2.378	3.649	0.659	5.72	1.935	0.10	4.2	12.32
6931	463.3	22.5	2.366	3.510	0.671	5.57	1.862	0.09	4.4	12.03
6935	464.4	22.0	2.373	3.716	0.654	5.77	1.868	0.09	4.5	12.42
6943	464.4	22.7	2.373	3.706	0.660	5.81	1.892	0.09	4.9	12.50
6948	463.3	22.2	2.386	3.646	0.671	5.84	1.941	0.09	1.9	12.61
6949	463.3	22.5	2.382	3.761	0.651	5.83	1.935	0.10	4.6	12.59
6958	462.2	21.2	2.356	3.724	0.636	5.58	1.813	0.10	3.8	12.08
6959	463.3	20.8	2.381	3.709	0.657	5.81	1.874	0.10	5.1	12.53
6963	462.3	20.8	2.383	3.620	0.666	5.74	1.886	0.10	3.7	12.43
6971	461.2	20.8	2.404	3.601	0.665	5.76	1.910	0.09	4.1	12.48
6972	461.0	20.8	2.403	3.660	0.666	5.86	1.935	0.09	5.0	12.71
6976	462.5	20.8	2.382	3.740	0.625	5.57	1.843	0.10	4.4	12.04

Table 40. Initial Spire I-V Characteristics of Encapsulated Modules.

Serial #	Area (cm^2)	Temp (^0C)	V_{oc} (V)	I_{sc} (A)	FF	P_{max} (W)	V_{mp} (V)	R_s (W)	R_{sh} (W)	Efficiency (%)
685496L	920.2	21.7	4.682	3.573	0.652	10.91	3.680	0.18	8.7	11.86
686167L	922.5	22.5	4.693	3.643	0.640	10.94	3.601	0.21	9.5	11.86
683941L	924.2	22.9	4.671	3.662	0.639	10.93	3.650	0.18	6.3	11.82
687083L	924.4	22.0	4.698	3.619	0.648	11.02	3.711	0.19	8.9	11.93
687475L	924.5	23.4	4.671	3.581	0.647	10.82	3.705	0.18	9.9	11.71
68876914L	924.5	22.2	4.713	3.582	0.660	11.13	3.705	0.19	10.2	12.04
67826835L	924.7	22.9	4.683	3.612	0.653	11.05	3.619	0.18	7.9	11.95
691548L	922.3	21.5	4.778	3.633	0.664	11.53	3.699	0.16	9.6	12.50
693543L	923.4	21.2	4.748	3.652	0.648	11.23	3.766	0.18	9.4	12.16
694959L	923.6	20.3	4.765	3.640	0.644	11.17	3.748	0.18	8.8	12.10

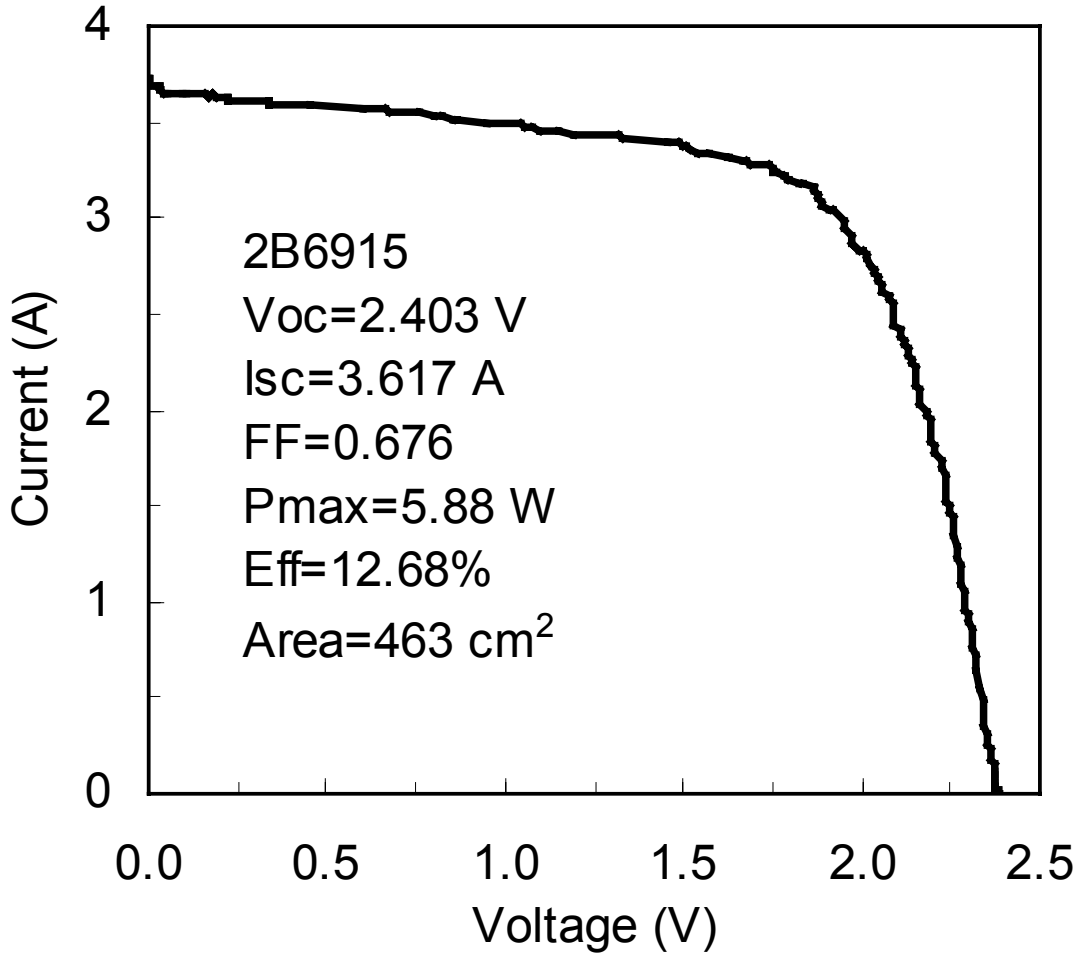

Figure 34. Initial I-V characteristics of unencapsulated module 2B6915 of aperture-area 463cm^2 and efficiency ~12.7%.

The initial values of the module, measured at 21.5^{0}C, are efficiency = 12.5%, P_{max} = 11.53W, V_{oc} = 4.780V, I_{sc} = 3.633A, and FF = 0.664.

6.7. NREL Measurement of Modules

Three of the ~920cm^2 modules shown in Table 40, #s 691548L, 683941L, and 67826835L, were sent to NREL for confirmation of the I-V measurements. NREL made three types of measurements: (1) indoor using Spire solar simulator equipped with a peak detector circuit board, (2) indoor using Large Area Continuous Solar Simulator (LACSS), and (3) outdoor using Standard Outdoor Measurement System (SOMS). A summary of the NREL measurements and the corresponding United Solar Spire measurements is provided in Table 41.

The table shows that the initial efficiency measured by NREL is lower all across the board. The United Solar efficiency values are 11.8-12.5%; the corresponding NREL numbers are 10.60-11.90%. As per the NREL values, module 691548L exhibits the highest efficiency 11.9% (LACSS) and 11.34% (Spire). These are the highest NREL measurements on any thin film a-Si alloy encapsulated module of this size. It is higher than the earlier world-record United Solar module measured by NREL. However, the discrepancy between the United Solar and NREL measurements is disturbing. Table 41 also gives the ratio of P_{max} measured at NREL (for each measurement technique) and United Solar and the average ratio for all the modules for each measurement technique. A corresponding I_{sc} ratio is also displayed. The average values of the P_{max} ratio for the NREL Spire, NREL LACSS, and NREL outdoor measurements are 90.8%, 96.0%, and 90.5%, respectively. The NREL LACSS measurements are within 4% of the United Solar Spire values. The other two NREL measurement techniques result in a much larger discrepancy. The average values of the I_{sc} ratio for the NREL, NREL LACSS, and NREL outdoor measurements are 91.8%, 97.2%, and 92.0%, respectively. The values of the I_{sc} ratios are similar to the P_{max} ratios. Thus, the discrepancy in the efficiency measurements at the two laboratories can be attributed primarily to the discrepancy in the I_{sc} measurements.

The discrepancy between the United Solar and the NREL measurements needs to be understood. With respect to the United Solar Spire solar simulator, we have made progress in the module efficiency. The progress with respect to the NREL measurements is somewhat ambiguous. Without better agreement, it is very difficult to make further progress since the optimization process becomes totally blind.

6.8. Stable Results

NREL has light soaked several modules from United Solar. The light soak was done under one-sun, 50^{0}C conditions. The stable results on five modules after 1000 hours are summarized in Table 42. Modules 566566L, 567577L, and 566179L were measured under Spire, SOMS, and LACSS illumination. Modules 67826835L and 691548L were measured under Spire and SOMS illumination. The value of the efficiency ranges from 9.4-10.5% depending on the module and the solar simulator. Module 566566L exhibits the highest efficiency of 10.53%, 10.50%, and 10.40% measured under the Spire, SOMS, and LACSS solar simulators, respectively.

NREL's measurement is somewhat disappointing since the initial United Solar measurements were significantly higher than the corresponding NREL numbers. The expectation was for a significantly higher stable efficiency. Not only are the absolute values of the measurements different in the two laboratories but a relative improvement in the United Solar modules based on United Solar measurements has translated into worse values based on corresponding NREL values. Some of these issues have been discussed in the previous section in the explanation of Table 41. The matter can be elucidated only after critical comparison of the solar simulators at both laboratories. Any optimization of the efficiency at United Solar is futile since the NREL measurements may not agree. This dilemma provides a cogent argument for failing to achieve the Phase III milestone of 11.5% stable efficiency.

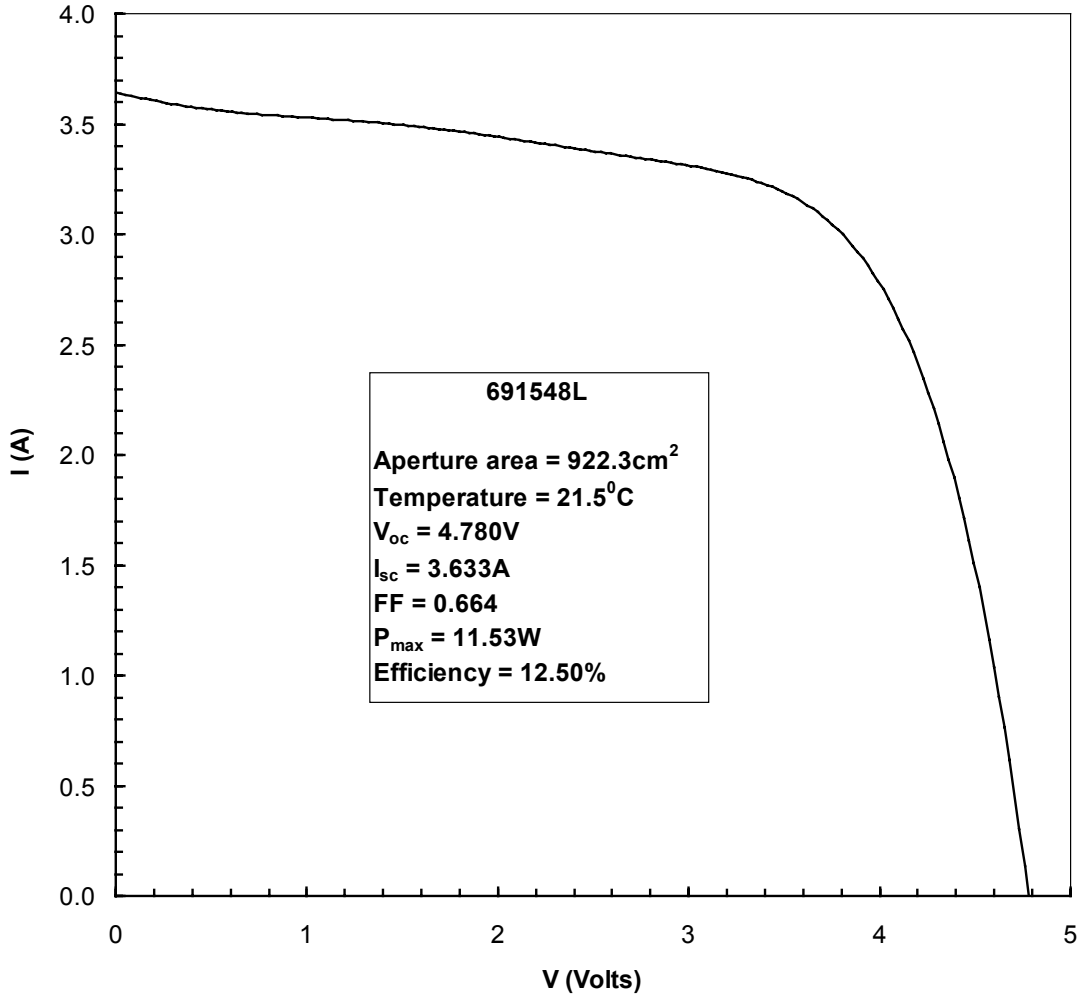

Figure 35. Initial I-V characteristics of encapsulated module 691548L of aperture-area 922cm^2.

Table 41. Comparison of NREL and United Solar Initial Measurements of Encapsulated Modules of Aperture Area ~920 cm^2.

Module	State	Area (cm^2)	Laboratory	Temp. (^0C)	V_{oc} (V)	I_{sc} (A)	I_{sc} NREL/US	FF	V_{max} (V)	I_{max} (A)	P_{max} (W)	P_{max} NREL/US	Efficiency (%)
691548L	Initial	922.3	US Spire	21.5	4.780	3.633		0.664	3.700	3.117	11.53		12.50
		918.0	NREL Spire	25.0	4.699	3.306	91.0%	0.670	3.711	2.806	10.41	90.3%	11.34
			NREL LACSS	26.2	4.680	3.538	97.4%	0.661	3.742	2.925	10.95	95.0%	11.90
			NREL Outdoor	27.4	4.620	3.295	90.7%	0.666	3.675	2.758	10.13	87.9%	11.00
683941L	Initial	924.2	US Spire	22.9	4.671	3.662		0.639			10.93		11.80
		930.9	NREL Spire	25.0	4.636	3.382	92.4%	0.635	3.619	2.750	9.95	91.1%	10.69
			NREL LACSS	26.3	4.604	3.553	97.0%	0.647	3.560	2.974	10.59	96.9%	11.40
			NREL Outdoor	25.4	4.589	3.389	92.5%	0.646	3.609	2.783	10.05	91.9%	10.60
67826835L	Initial	924.7	US Spire	22.9	4.683	3.612		0.653			11.05		11.90
		930.9	NREL Spire	25.0	4.640	3.326	92.1%	0.651	3.528	2.849	10.05	91.0%	10.80
			NREL LACSS	26.0	4.618	3.506	97.1%	0.656	3.626	2.928	10.62	96.1%	11.40
			NREL Outdoor	26.1	4.582	3.353	92.8%	0.659	3.609	2.805	10.12	91.6%	10.80
Average discrepancy (United Solar/NREL)			**NREL Spire**				**91.8%**					**90.8%**	
			NREL LACSS				**97.2%**					**96.0%**	
			NREL Outdoor				**92.0%**					**90.5%**	

Table 42. NREL Measurement of Stable Encapsulated Module Performance.

Module 2B	Simulator	Irradiance (W/m^2)	Temp. (^0C)	V_{oc} (V)	I_{sc} (A)	FF (%)	P_{max} (W)	Eff. (%)
566566L	Spire	1000.0	25.1	4.418	3.2996	65.37	9.530	10.53
	SOMS	1036.0	28.4	4.327	3.4778	65.20	9.811	10.50
	LACSS	1000.0	26.5	4.353	3.2854	65.98	9.436	10.40
567577L	Spire	1000.0	25.4	4.408	3.2551	64.62	9.273	10.10
	SOMS	1050.0	28.6	4.322	3.5253	64.13	9.770	10.10
	LACSS	1000.0	27.9	4.302	3.3228	65.13	9.310	10.10
566179L	Spire	1000.0	25.4	4.381	3.2502	64.91	9.241	10.09
	SOMS	1054.0	27.7	4.323	3.5132	64.38	9.777	10.10
	LACSS	1000.0	26.2	4.331	3.3779	63.78	9.330	10.20
67826835L	Spire	1000.0	24.9	4.515	3.2726	59.43	8.782	9.43
	SOMS	1036.5	30.8	4.374	3.5433	58.80	9.114	9.45
691548L	Spire	1000.0	25.4	4.568	3.2628	61.73	9.201	10.02
	SOMS	1037.0	34.6	4.369	3.4507	62.11	9.364	9.84

6.9. Summary of Large Area Results

A summary of all the large-area stable results for the component cells, triple-junction devices, and triple-junction modules is given in Table 43. The corresponding milestones for Phase III of the program are also tabulated. Note that for the triple-junction module, the NREL Spire data is given. The data shows that most of the milestones have been achieved. The reasons for missing the goals for the triple-junction cells and modules are discussed in the text.

Table 43. Summary of all Stable Results and Corresponding Phase III Milestones.

Cell/ Module	Sub.	Spectrum	Total area/ aper. area (cm^2)	Active area results			Total area/aper. area results		
				J_{sc} (mA/cm^2)	V_{oc} (V)	FF	I_{sc} (A)	P_{max} (mW/cm^2)	Efficiency (%)
Top	ss	AM1.5	0.268	8.8	0.991	0.680		5.5	
Phase III milestone			1					5.4	
Middle	Ss	>530nm	0.268	10.14	0.727	0.532		3.7	
Phase III milestone			1					3.3	
Bottom	Ag/ZnO	>630nm	0.268	11.81	0.572	0.533		3.4	
Phase III milestone			1					3.5	
Triple	Ag/ZnO	AM1.5	0.268	8.51	2.201	0.666			11.6
Phase III milestone			1						12.2
Module *	Ag/ZnO	AM1.5	905.1	3.2996	4.418	0.6537	3.538		10.53
Phase III milestone									11.5

* NREL Spire results

6.10. Large-Area Prototype Modules

We have investigated methods and processes for fabricating large-area flexible modules of two different sizes. One size has a nominal outside dimension of 216”x29.6”, and the other size is 216”x15.5”. The material and processes used for these prototype modules are compatible with United Solar’s current production line. The larger size of the prototype module, however, is two times the largest standard rigid product. The motivation for investigating the methods of fabrication of these 18’ long flexible modules is to

evaluate and qualify each step of the manufacturing process. We have successfully completed qualifying each step in the process and one prototype module from each size was delivered to NREL. The 216"x 15.5" module was measured by NREL on October 20, 1998 to produce 155.5W under outdoor conditions at 1025 W/m^2 irradiance. The module temperature was 39^0C-45^0C. The 216"x.29.6" module was measured by NREL on December 3, 1998 to produce 317.8W under outdoor conditions at $1044W/m^2$ irradiance The module temperature was 34^0C-39^0C. Assuming a typical degradation of 15%, the modules should stabilize to ~130W and 260W, respectively, higher than the 125W and 250W goals.

6.11. IEEE Std 1262-1995 Qualification of Modules

United Solar has carried out a detailed and systematic qualification of its commercial products. We have sent out many of these products to the Department of Electronics and Computer Technology at the Arizona State University for lEEE 1262 and IEC 1646 qualification testing. All our products pass the qualification tests. Relevant pages from the test-report document (Test Report Number 8100101) were included in the Phase I Annual Report. The R&D modules fabricated for the NREL program have been fabricated using the same materials and processes used in the production line. By the principle of similarity, the R&D modules therefore pass the same tests.

Section 7

Cells and Modules made Using Production Parameters in a Large-Area Reactor

7.1. Introduction

Towards the end of the program, a new effort was initiated to develop high efficiency component and triple-junction devices using parameters and conditions used in our production machine. The goal was to explore the possibility of enhancing the efficiency of our finished products using conditions used in the production environment. Some of the production parameters that have been incorporated for the development of the devices were deposition rate ~3Å/s, deposition pressure, substrate temperature, gas dilution, gas utilization efficiency, and rf power density. The imposition of the restrictions on the available regime of the deposition parameters is expected to have a deleterious effect on the cell performance. The challenge was to explore means to improve the device efficiency while working within the constraints.

Another important restriction imposed for the optimization process was the use of Al/ZnO back reflector used in production. Initially, it was decided that some cells be fabricated on the superior Ag/ZnO back reflector to evaluate the state-of-art for the a-Si alloy technology. However, due to limitation of time and in order to do full justice to the more important Al/ZnO program, this effort was abandoned. The revised strategy of focusing all our efforts on Al/ZnO back reflector has paid off. Important results critical to the upcoming 25MW machine have been accomplished.

The a-Si alloy work has been carried out in the large-area "2B" deposition reactor whose geometry is similar to the roll-to-roll deposition machine. It is the same machine that has been used for the work described in section 6. Cells are deposited over a ~1sq. ft. area. The substrate is cut up into 2"x2" pieces and TCO is deposited through an evaporation mask to delineate devices of total-area 0.268cm^2. The methodology used for the fabrication of component cells, triple-junction cells, and modules is identical to the approach used in section 6.

7.2. Component Cells

The initial total-area performance of the top, middle, and bottom component cells of area 0.268cm^2 are summarized in Table 44. The top and middle cells have been made on stainless steel substrate with no back reflector and the bottom cell is on Al/ZnO back reflector. The I-V measurements correspond to AM1.5 illumination for the top cell, AM1.5+530nm cut-on filter for the middle cell and AM1.5+630nm cut-on filter for the bottom cell. The J_{sc} has been obtained using Q measurements. The efficiency of the two top cells 2B8323 and 2B8325 is ~5.9%. The P_{max}>530nm for the middle cell 2B8316 is ~3.7mW/cm^2. The

Table 44. Initial Total-Area Results of Component Cells of Area 0.268cm^2 made at ~3Å/s using Production Parameters.

Cell	Sub.	Spectrum	Sample 2B	V_{oc} (V)	J_{sc} (Q) (mA/cm^2)	FF	Eff. (%) or P_{max} (mW/cm^2)
Top	ss	AM1.5	8323	0.992	8.28	0.716	5.9%
			8325	0.976	8.19	0.735	5.9%
Middle	ss	>530nm	8316	0.704	7.85	0.666	3.7
Bottom	Al/ZnO	>630nm	8358	0.588	8.45	0.626	3.1
			8364	0.596	8.09	0.644	3.1

P_{max}>630nm for the two bottom cells 2B8358 and 2B8364 is ~3.1mW/cm^2. The initial performance of all the component cells is similar to that of corresponding cells made in a small-area machine without any of the restrictions imposed due to production related issues. These results are encouraging in terms of anticipated performance of the upcoming 25MW machine.

7.3. Triple-Junction Cells

Triple-junction devices have been fabricated on Al/ZnO back reflector using the component cells tabulated in Table 44 above. The initial results of two devices are summarized in Table 45. The initial total-area efficiency of devices 2B7748#LC1 and 2B8429#LC1 are 11.9% and 11.6%, respectively. The values of V_{oc}, FF, and total-area Q of the component cells are also summarized in Table 45. The Q of the current-limiting component cell has been used as the J_{sc} of the device.

Table 45. Initial Total-Area Results of Triple-Junction Devices of Area 0.268cm^2 made at ~3Å/s on Al/ZnO Back Reflector.

Run #	V_{oc}	FF	J_{sc}	Efficiency	$Q_{top}/Q_{mid}/Q_{bot}/Q_{tot}$
2B	(V)		(mA/cm^2)	(%)	(mA/cm^2)
7748#LC1	2.287	0.717	6.77	11.1	7.03/6.95/6.77/20.76
8429#LC1	2.275	0.704	6.78	10.9	6.79/6.78/6.83/20.41

7.4. Stability Studies

For stability studies, several 2"x2" substrates were cut from an area of ~460cm^2 of the original large-area substrate. The average results compiled on all the 2"x2" substrates is representative of the 460cm^2 area.

7.4.1. Top Cell on Stainless Steel Substrate

Six 2"x2" substrates, representing the large-area substrate stainless steel substrate with no back reflector, were selected. The average of the J-V characteristics of the small-area cells is assumed to be representative of the large-area device. The initial and stable performance after 1004 hours of light soak of the six sets of devices and their average values are listed in Table 46. Each value in the table represents the average of several 0.268cm^2 devices on that substrate. The light soaking was done under AM1.5 global illumination at 50^{0}C and open-circuit conditions. The table shows that the average values of the stable total-area efficiency for the six substrates are in the range of ~4.9-5.4mW/cm^2. The average for all the substrates shown at the bottom of Table 46 is ~5.1mW/cm^2 and is representative of the entire large-area 460cm^2 substrate. The stabilized total-area efficiency of 5.1mW/cm^2 meets the phase III milestone of 4.3mW/cm^2.

7.4.2. Middle Cell on Stainless Steel Substrate

Similar work has been carried out on middle cell on stainless steel substrate with no back reflector. Six representative 2"x2" pieces with 0.268cm^2 total-area devices were prepared. The initial performance of the devices was measured under AM1.5 illumination using a λ>530nm cut-on filter. The devices were then light-soaked under open circuit, one sun with filter, and 50^{0}C conditions. The filter was selected such that the intensity corresponded to a J_{sc} of ~7.0-8.0mA/cm^2. The initial and light-soaked results after 1055 hours of the six substrates are summarized in Table 47. Each value in the table represents the average of several 0.268cm^2 devices on that substrate. The average stable values of P_{max} at λ>530nm for the six substrates are in the range of 2.3-2.9mW/cm^2. The average for all the substrates shown at the bottom of Table 47 is 2.7mW/cm^2 and is representative of the entire large-area 460cm^2 substrate. The stabilized value of 2.7mW/cm^2 is close to the Phase III milestone of 2.8mW/cm^2 for the third year of the program.

Table 47. Average Total-Area Results of 0.268cm^2 a-Si Alloy Top Cell on 2"x2" Stainless Steel Substrate with No Back Reflector.

Sample #	Area	Source	Light Soak	V_{oc}	FF	J_{sc} (Q)	Efficiency (Q)
2B8325	(cm^2)		(hours)	(V)		(mA/cm^2)	(mW/cm^2)
LC1	0.268	AM1.5	0	0.977	0.731	8.19	5.9
			1004	0.939	0.673	7.94	5.0
A0	0.268	AM1.5	0	0.971	0.739	8.67	6.2
			1004	0.939	0.683	8.45	5.4
B2	0.268	AM1.5	0	0.967	0.735	8.23	5.8
			1004	0.931	0.680	8.03	5.1
D0	0.268	AM1.5	0	0.974	0.737	8.47	6.1
			1004	0.940	0.665	8.24	5.1
E1	0.268	AM1.5	0	0.962	0.745	7.99	5.7
			1004	0.936	0.664	7.81	4.9
I	0.268	AM1.5	0	0.974	0.736	8.55	6.1
			1004	0.946	0.682	8.35	5.4
Average initial		**AM1.5**	**0**	**0.971**	**0.737**	**8.35**	**6.0**
Average stable		**AM1.5**	**1004**	**0.938**	**0.674**	**8.14**	**5.1**
Phase III milestone		**AM1.5**	**1000**				**4.3**

Table 46. Average Total-Area Results (λ>530nm) of Small-Area a-SiGe Alloy Middle Cell on a 2"x2" Stainless Steel Substrate with No Back Reflector.

Sample #	Area	Source	Light Soak	V_{oc}	FF	J_{sc} (Q)	P_{max} (Q)
2B8316	(cm^2)		(hours)	(V)		(mA/cm^2)	(mW/cm^2)
LC1	0.268	>530nm	0	0.704	0.670	7.85	3.7
			1055	0.654	0.555	7.29	2.6
A1	0.268	>530nm	0	0.703	0.672	8.06	3.8
			1055	0.649	0.551	7.36	2.6
B0	0.268	>530nm	0	0.718	0.697	7.70	3.9
			1055	0.664	0.598	7.22	2.9
D2	0.268	>530nm	0	0.704	0.651	7.79	3.6
			1055	0.651	0.516	6.93	2.3
E0	0.268	>530nm	0	0.720	0.697	7.61	3.8
			1055	0.665	0.592	7.17	2.8
I	0.268	>530nm	0	0.738	0.720	6.91	3.7
			1055	0.686	0.641	6.49	2.9
Average initial		**>530nm**	**0**	**0.714**	**0.684**	**7.65**	**3.7**
Average stable		**>530nm**	**1055**	**0.661**	**0.575**	**7.30**	**2.7**
Phase III Milestone		**>530nm**	**1000**				**2.8**

7.4.3. Bottom Cell on Al/ZnO Back Reflector

For the bottom cell, an Al/ZnO back reflector substrate has been used. Two 2"x2" pieces with 0.268cm^2 total-area devices from two different run numbers were prepared. For lack of time, it was not possible to light soak six substrates. The initial performance of the devices was measured under AM1.5 illumination using a λ>630nm cut-on filter. The devices were then light-soaked under open circuit, one sun with filter,

and 50^{0}C conditions. The filter was selected such that the intensity corresponded to a J_{sc} of 7.0-8.0mA/cm^2. The initial and 1012 hour light soak results of the two substrates are summarized in Table 48. Each value in the table represents the average of several 0.268cm^2 devices on the substrate. The average stable values of P_{max} at λ>630nm for the two samples 2B8358#LC1 and 2B8364#LC1 are 2.5 and 2.6mW/cm^2, respectively. Both these samples satisfy the Phase III milestone of 2.5mW/cm^2 for the third year of the program.

Table 48. Total-Area Results (λ>630nm) of Small-Area a-SiGe Alloy Bottom Cell on 2"x2" Al/ZnO Substrate.

Sample #	Area	Source	Lite Soak	V_{oc}	FF	J_{sc} (Q)	P_{max} (Q)
2B	(cm^2)		(hours)	(V)		(mA/cm^2)	(mW/cm^2)
8358#LC1	0.268	>630nm	0	0.586	0.624	8.45	3.1
			1012	0.556	0.562	7.93	2.5
8364#LC1	0.268	>630nm	0	0.595	0.644	8.09	3.1
			1012	0.565	0.581	7.80	2.6
Phase III Milestone		**>630nm**	**1000**				**2.5**

7.4.4. Triple-Junction Cell on Al/ZnO Back Reflector

Triple-junction triple-bandgap a-Si/a-SiGe/a-SiGe alloy cells were deposited on Al/ZnO back reflector. Due to lack of time, small-area cell performance was measured on only one 2"x2" sample 2B8429. The initial and the stabilized results after 1012 hours of light soak are shown in Table 49. The table represents the average of several 0.268cm^2 devices on the substrate. The average initial total-area efficiency is ~10.9% and the stable value is 9.1%. The Phase III milestone, shown in the same table, for the stabilized total-area efficiency is 9.0%. The stabilized total-area efficiency of 9.1%, thus, meets the Phase III milestone.

Table 49. Total-Area Results of Small-Area Triple-Junction Cell on 2"x2" Al/ZnO Substrate.

Sample #	Area	Lite Soak	V_{oc}	FF	J_{sc} (Q)	Efficiency (Q)	$Q_{top}/Q_{mid}/Q_{bot}/Q_{tot}$
2B	(cm^2)	(hours)	(V)		(mA/cm^2)	(%)	(mA/cm^2)
8429#LC1	0.268	0	2.275	0.704	6.78	10.9	7.28/7.27/7.32/21.87
		1012	2.171	0.636	6.60	9.1	7.16/7.08/7.27/21.52
Phase III Milestone		**1000**				**9.0**	

7.5. Module Results

Triple junction modules have been fabricated on Al/ZnO back reflector using deposition rates and deposition conditions to be used in the 25MW production machine. The modules were processed, encapsulated, and measured in a way similar to that described in Section 6.2.2. The aperture area of the modules is typically ~460cm^2. The I-V characteristics of the modules were measured before and after encapsulation. Tables 50 and 51 summarize the initial results of several modules before and after encapsulation, respectively. The initial efficiency of the unencapsulated modules is in the range of ~10.4-11.0%. Unencapsulated module 2B8493 exhibits the highest initial efficiency ~11.0%. The I-V characteristics of the module are shown in Fig. 36. The V_{oc} = 2.338V, I_{sc} = 3.09A, FF = 0.704, and the aperture area is 461.4cm^2. Encapsulated module 2B8493L exhibits the highest initial efficiency ~10.6%. The I-V characteristics of the module are shown in Fig. 37. The V_{oc} = 2.320V, I_{sc} = 2.95A, FF = 0.709, and the aperture area is 458.0cm^2. These values are substantially higher than those being currently obtained from the present 5MW production machine.

Table 50. Initial Results of Unencapsulated Modules on Al/ZnO Back Reflector.

Module #	Area	Temp.	V_{oc}	I_{sc}	FF	P_{max}	V_{mp}	R_s	R_{sh}	Efficiency
2B	(cm^2)	(^{0}C)	(V)	(A)		(W)	(V)	(ohm)	(ohm)	(%)
8493	461.4	23.2	2.338	3.09	0.704	5.09	1.910	0.09	5.1	11.02
8465	462.3	24.7	2.312	3.03	0.712	4.99	1.953	0.08	5.3	10.79
8492	458.0	23.2	2.307	3.05	0.694	4.89	1.910	0.09	4.7	10.67
8488	442.8	22.9	2.315	2.92	0.696	4.70	1.923	0.10	4.1	10.61
8486	462.3	23.7	2.301	3.07	0.694	4.90	1.892	0.09	4.5	10.59
8490	462.3	23.4	2.302	3.05	0.697	4.90	1.855	0.09	5.5	10.59
8489	462.3	22.9	2.314	3.06	0.690	4.88	1.923	0.09	4.1	10.55
8487	462.3	23.4	2.296	3.02	0.701	4.87	1.880	0.08	5.0	10.53
8467	462.3	23.4	2.318	2.98	0.702	4.86	1.886	0.09	4.9	10.51
8485	462.3	23.7	2.293	2.99	0.702	4.81	1.947	0.09	4.7	10.41
8464	462.3	23.2	2.318	2.98	0.693	4.79	1.923	0.08	4.0	10.37

Table 51. Initial Results of Encapsulated Modules on Al/ZnO Back Reflector.

Module #	Area	Temp.	V_{oc}	I_{sc}	FF	P_{max}	V_{mp}	R_s	R_{sh}	Efficiency
2B	(cm^2)	(^{0}C)	(V)	(A)		(W)	(V)	(ohm)	(ohm)	(%)
8493L	458.0	23.9	2.320	2.95	0.709	4.85	1.923	0.086	5.2	10.58
8465L	459.0	25.1	2.309	2.91	0.710	4.77	1.941	0.095	6.0	10.40
8492L	457.4	24.2	2.296	2.95	0.699	4.73	1.892	0.097	5.8	10.35
8486L	456.4	24.7	2.287	2.95	0.696	4.70	1.874	0.083	4.4	10.29
8490L	456.9	24.4	2.289	2.95	0.696	4.70	1.880	0.098	4.7	10.28
8489L	458.0	24.4	2.299	2.91	0.701	4.69	1.904	0.099	4.8	10.24
8464L	458.0	22.7	2.315	2.85	0.708	4.67	1.935	0.085	5.3	10.19
8487L	458.0	24.2	2.287	2.93	0.695	4.66	1.892	0.093	4.5	10.17
8467L	455.8	23.4	2.311	2.84	0.705	4.63	1.910	0.089	6.1	10.16
8485L	456.9	24.2	2.281	2.93	0.694	4.63	1.862	0.088	4.2	10.14

Four modules listed in Table 51, 2B8464L, 2B8465L, 2B8467L, and 2B8486L have been light soaked at United Solar under one-sun, open-circuit, and 50^{0}C conditions. The results after 520 hours of light soak are summarized in Table 52. The light-soaked efficiency is in the range of ~8.7-9.1%. Since most of the degradation occurs during the first 200 hours, these values are close to the stable values. Light soaking will be continued for 1000 hours and the stable values measured. Module 2B8486L exhibits the highest stable efficiency ~9.1% after the first 520 hours of light soak. It should pass the Phase III milestone of 8.4%.

7.6. Summary

Small-area cells and modules have been fabricated on Al/ZnO back reflector using the projected 25MW/year production machine parameters. The highest initial total-area efficiency is ~11.1% on a 0.268cm^2 device. For another sample, the initial total-area efficiency is ~10.9%, and the stable total-area efficiency ~9.1%. The highest aperture-area efficiency obtained on an encapsulated module of aperture area 458cm^2 is ~10.6%. The efficiency after 520 hours of light soak ~9.1%. These values are significantly higher than those being fabricated using the present 5MW/year production machine.

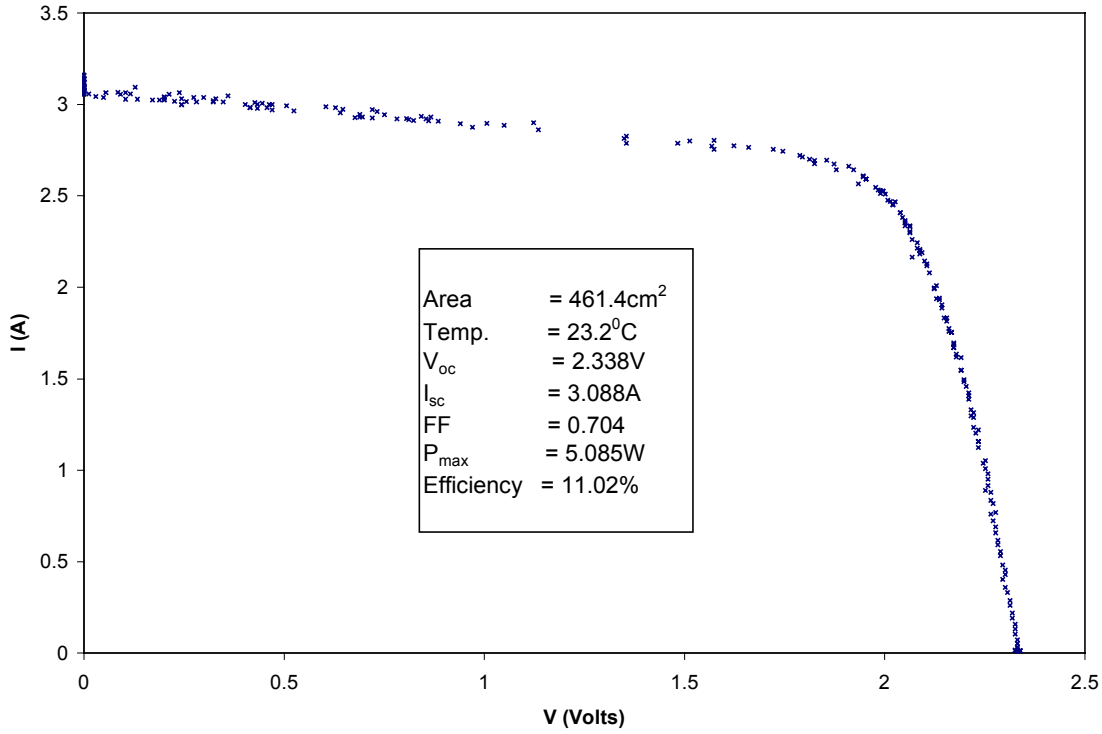

Figure 36. Initial I-V characteristics of unencapsulated module 2B8493 on Al/ZnO back reflector.

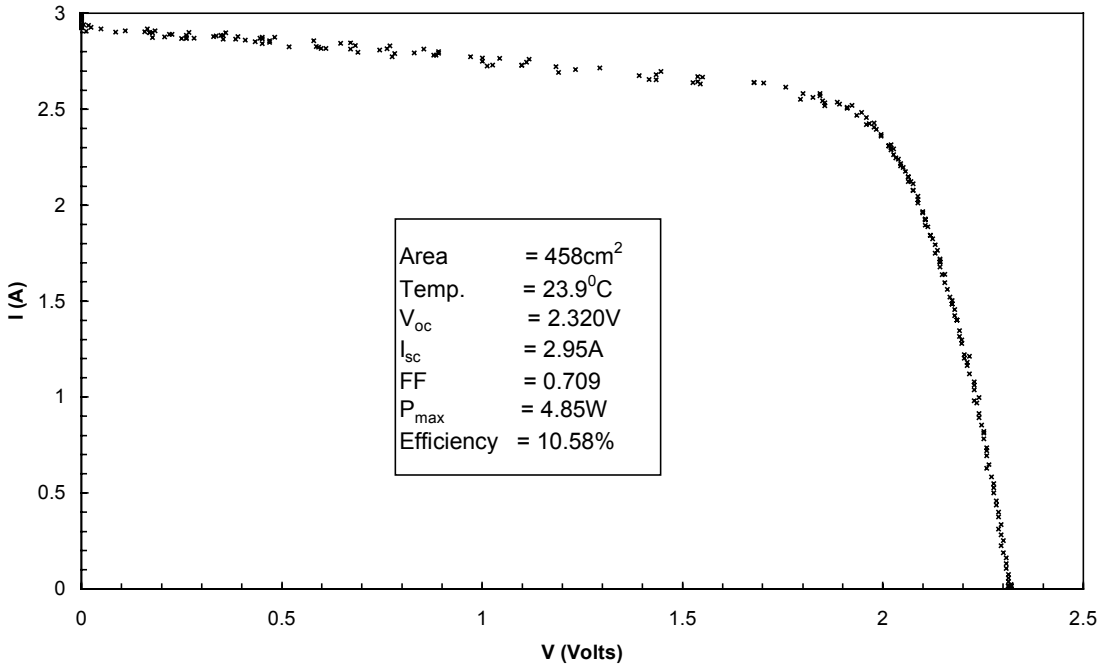

Figure 37. Initial I-V characteristics of encapsulated module 2B8493L on Al/ZnO back reflector.

Table 52. Stable Results of Encapsulated Modules on Al/ZnO Back Reflector after 520 Hours of Light Soak.

Module #	Area	Temp.	V_{oc}	I_{sc}	FF	P_{max}	V_{mp}	R_s	R_{sh}	Efficiency
2B	(cm^2)	(^0C)	(V)	(A)		(W)	(V)	(ohm)	(ohm)	(%)
8464L	458.0	23.9	2.207	2.83	0.654	4.09	1.740	0.112	4.1	8.93
8465L	459.0	24.2	2.207	2.90	0.647	4.14	1.752	0.100	5.1	9.02
8467L	455.8	23.9	2.200	2.80	0.642	3.96	1.685	0.117	4.9	8.68
8486L	456.4	23.7	2.202	2.90	0.649	4.14	1.740	0.103	4.7	9.08
Phase III milestone										8.4%

Section 8

References

Banerjee, A.; Xu, X.; Yang, J.; Guha, S. (1995). "Analysis of fill factor losses in a-Si and a-SiGe alloy solar cells using a new technique." *Mater. Res. Soc. Symp. Proc*. **377**, 675.

Biebericher, A.C.W.; Bezemer, J.; van der Weg, W.F.; Goedheer, W. (2000). "Fast growth of amorphous silicon layers by amplitude modulation PECVD." *Mater. Res. Soc.Symp. Proc*. **609**, A4.1.1

Chatham, H.; Bhat, P.K. (1989). "High deposition rate P-I-N solar cells prepared from disilane using VHF discharge." *Mater. Res. Soc. Symp. Proc.* **149**, 447.

Gallagher, A. (1999). Private communication.

Guha, S.; Narasimhan, K.L.; Pietruszko, S.M. (1981). "On light-induced effects in amorphous hydrogenated silicon." *J. Appl. Phys*. **52**, 859.

Guha, S.; Yang, J.; Pawlikiewicz, A.; Glatfelter, T.; Ross, R.; Ovshinsky, S.R. (1989). "Band-gap profiling for improving the efficiency of amorphous silicon alloy solar cells." *Appl. Phys. Lett.* **54**, 2330.

Guha, S.; Yang, J.; Jones, S. J.; Chen, Y; Williamson, D. L. (1992). " Effect of microvoids on initial and light-degraded efficiencies of hydrogenated amorphous silicon alloy solar cells." *Appl. Phys. Lett* **61**, 1444.

Guha, S.; Xu, X.; Yang, J.; Banerjee, A. (1995). " High deposition rate amorphous silicon-based multijunction solar cell." *Appl. Phys. Lett.* **66**, 595.

Guha, S.; Yang, J.; Williamson, D.L.; Lubianiker, Y.; Cohen, J.D.; Mahan, A.H. (1999). "Structural, defect, and device behavior of hydrogenated amorphous Si near and above the onset of microcrystallinity." *Appl. Phys. Lett.* **74**, 1860.

Harmers, E.A.G.; Bezermer, J.; Meiling, H.; van Spark, W.G.J.H.M.; van der Weg, W.F. (1997). "Ion bombardment in silane VHF deposition plasmas." *Mater. Res. Soc. Symp. Proc.* **467**, 603.

Isomura, M.; Yamamoto, H.; Kondo, M.; Matsuda, A. (1998). "The light-induced increase in open circuit voltage of amorphous silicon solar cells." *2nd World Conference and Exhibition on Photovoltaic Solar Energy Conversion* (IEEE, NewYork, 1998), 925.

Koh, J.; Lee, Y.; Fujiwara, H.; Wronski, C.R.; and Collins, R.W. (1998). "Optimization of hydrogenated amorphous silicon *p-i-n* solar cells with two-step *i* layers guided by real-time spectroscopic ellipsometry." *Appl. Phys. Lett.* **73**, 1526.

Longeaud, C.; Kleider, J.P.; Gauthier, M.; Brüggemann, R.; Poisant, Y.; Roca i Cabarrocas, P. (1999). "Polymorphous silicon: transport properties and solar cell applications." *Mater. Res. Soc. Symp. Proc.* **557**, 501.

Mahan, A.H.; Yang, J.; Guha, S.; Williamson, D.L. (2000). "Structural changes in a-Si:H film crystallinity with high H dilution." *Phys. Rev. B* **61**, 1677.

Matsuda, A. (1996). "Control of plasma and surface conditions for low defect density a-Si:H at high growth rates." *Conf. Record 25th IEEE Photovoltaics Specialists Conference* (IEEE, New York, 1996), 1029.

Platz, R.; Wagner, S.; Hof, C.; Shah, A.; Wieder, S.; Rech, B. (1998). "Influence of excitation frequency, temperature, and hydrogen dilution on the stability of plasma enhanced chemical vapor deposited a-Si:H." *J. Appl. Phys.* **84**, 3949.

Roca i Cabarrocas, P.; St'ahel, P.; Hamma, S.; Poissant, Y. (1998). "Stable single junction p- i-n solar cells with efficiencies approaching 10%." *2nd World Conference and Exhibition on Photovoltaic Solar Energy Conversion* (IEEE, New York, 1998), 355.

Shah, A.; Meier, J.; Torres, P.; Kroll, U.; Fischer, D.; Beck, N.; Wyrsch, N.; Keppner, H. (1997). "Recent progress of microcrystalline solar cells." *Conference Record of the Twenty Sixth IEEE Photovoltaic Specialists Conference* (IEEE, New York, 1998), 569.

Sheng, S.; Liao, X.; Ma, Z.; Yue, G.; Wang, Y.; and Kong, G.; (2001). "Hydrogenated Amorphous Silicon Films with Significantly Improved Stability." *Solar Energy Materials and Solar Cells* **68**, 123.

Siamchai P.; Konagai, M. (1995). "Degradation behavior of amorphous silicon solar cells fabricated by mercury-sensitized photochemical vapor deposition with hydrogen dilution." *Appl. Phys. Lett.* **67**, 3468.

Staebler, D.L.; Wronski, C.R. (1977). "Reversible conductivity changes in discharge-produced amorphous Si." *Appl. Phys. Lett*. **31**, 292.

Tsu, D.V.; Chao, B.S.; Ovshinsky, S.R.; Guha, S.; Yang, J. (1997). "Effect of hydrogen dilution on the structure of amorphous silicon alloys." *Appl. Phys. Lett.* **71**, 1317.

Tsu, D.V.; Chao, B.S.; Ovshinsky, S.R.; Jones, S.J.; Yang, J.; Guha, S.; Tsu, R. (2001). "Heterogeneity in hydrogenated silicon: Evidence for intermediately ordered chainlike objects." *Phys. Rev. B* **63**, 125338.

van Sark, W.G.J.H.M.; Bezermer, J.; van der Heijden, R.; van der Weg, W. F. (1996). "a-Si:H solar cells deposited using VHF-PECVD." *Mater. Res.Soc. Symp. Proc.* **420**, 21.

Yan, B.; Yang, J.; Guha, S.; Gallagher, A. (1999). "Analysis of plasma properties and deposition of amorphous silicon alloy solar cells using very high frequency glow discharge." *Mater. Res. Soc. Symp. Proc*., **557**, 115.

Yang, J.; Banerjee, A.; Guha, S. (1997). "Triple-junction amorphous silicon alloy solar cell with 14.6% initial and 13.0% stable conversion efficiencies." *Appl. Phys. Lett.* **70**, 2975.

Yang, J.; Sugiyama, S.; Guha, S. (1998). "Effect of excitation frequency on the properties of amorphous silicon solar cells." *Mater. Res. Soc. Symp. Proc.* **507**, 157.

Yang, J.; Guha, S. (1999). " Amorphous silicon alloy materials and solar cells near the threshold of microcrystallinity." *Mater. Res. Soc. Symp. Proc.* **557**, 239.

Yang, J.; Lord, K.; Guha, S.; Ovshinsky, S.R. (2000). "Amorphous silicon alloy solar cells near the threshold of amorphous-to-microcrystalline transition." *Mater. Res. Soc. Symp. Proc*. **609**, A15.4.

Yang L.; Chen, L. (1994). "The effect of H_2 dilution on the stability of a-Si:H based solar cells." *Mater. Res. Soc. Symp. Proc.* **336**, 669.

REPORT DOCUMENTATION PAGE

Form Approved
OMB NO. 0704-0188

1. AGENCY USE ONLY (Leave blank)	2. REPORT DATE	3. REPORT TYPE AND DATES COVERED
	November 2001	Final Technical Report 6 March 1998 – 15 October 2001

4. TITLE AND SUBTITLE
High-Efficiency Triple-Junction Amorphous Silicon Alloy Photovoltaic Technology
Final Technical Report, 6 March 1998 – 15 October 2001

5. FUNDING NUMBERS
CF: ZAK-8-17619-09
PVP25001

6. AUTHOR(S)
S. Guha

PERFORMING ORGANIZATION NAME(S) AND ADDRESS(ES)
United Solar Systems Corp.
1100 West Maple Road
Troy, Michigan 48084

8. PERFORMING ORGANIZATION REPORT NUMBER

9. SPONSORING/MONITORING AGENCY NAME(S) AND ADDRESS(ES)
National Renewable Energy Laboratory
1617 Cole Blvd.
Golden, CO 80401-3393

10.SPONSORING/MONITORING AGENCY REPORT NUMBER
NREL/SR-520-31290

11.SUPPLEMENTARY NOTES
NREL Technical Monitor: Ken Zweibel

12a. DISTRIBUTION/AVAILABILITY STATEMENT
National Technical Information Service
U.S. Department of Commerce
5285 Port Royal Road
Springfield, VA 22161

12b. DISTRIBUTION CODE

13.ABSTRACT *(Maximum 200 words)* This report describes the research program intended to expand, enhance, and accelerate knowledge and capabilities for developing high-performance, two-terminal multijunction amorphous silicon (a-Si) alloy cells, and modules with low manufacturing cost and high reliability. United Solar uses a spectrum-splitting, triple-junction cell structure. The top cell uses an amorphous silicon alloy of ~1.8-eV bandgap to absorb blue photons. The middle cell uses an amorphous silicon germanium alloy (~20% germanium) of ~1.6-eV bandgap to capture green photons. The bottom cell has ~40% germanium to reduce the bandgap to ~1.4-eV to capture red photons. The cells are deposited on a stainless-steel substrate with a predeposited silver/zinc oxide back reflector to facilitate light-trapping. A thin layer of antireflection coating is applied to the top of the cell to reduce reflection loss. The major research activities conducted under this program were: 1) Fundamental studies to improve our understanding of materials and devices; the work included developing and analyzing a-Si alloy and a-SiGe alloy materials prepared near the threshold of amorphous-to-microcrystalline transition and studying solar cells fabricated using these materials. 2) Deposition of small-area cells using a radio-frequency technique to obtain higher deposition rates. 3) Deposition of small-area cells using a modified very high frequency technique to obtain higher deposition rates. 4) Large-area cell research to obtain the highest module efficiency. 5) Optimization of solar cells and modules fabricated using production parameters in a large-area reactor.

14.SUBJECT TERMS: PV ; triple-junction cell structure ; two-terminal multijunction ; amorphous silicon (a-Si) alloy cells; spectrum-splitting ; modified very-high-frequency technique ; manufacturing; radio frequency technique

15.NUMBER OF PAGES

16.PRICE CODE

17.SECURITY CLASSIFICATION OF REPORT	18.SECURITY CLASSIFICATION OF THIS PAGE	19.SECURITY CLASSIFICATION OF ABSTRACT	20.LIMITATION OF ABSTRACT
Unclassified	Unclassified	Unclassified	UL